LA-13687-T
Thesis

Deformation of a Beryllium-Aluminum Composite

Los Alamos
NATIONAL LABORATORY

Los Alamos National Laboratory is operated by the University of California for the United States Department of Energy under contract W-7405-ENG-36.

This dissertation was accepted by the Materials Department, University of California, Santa Barbara, California, in partial satisfaction of the requirements for the degree of Doctor of Philosophy in Materials. The text and illustrations are the independent work of the author and only the front matter has been edited by the CIC-1 Writing and Editing Staff to conform with Department of Energy and Los Alamos National Laboratory publication policies.

An Affirmative Action/Equal Opportunity Employer

LA-13687-T
Thesis

Issued: March 2000

Deformation of a Beryllium-Aluminum Composite

David H. Carter

Los Alamos
NATIONAL LABORATORY
Los Alamos, New Mexico 87545

Dedication

This work is dedicated with love to my parents and my wife, Janice.

Acknowledgments

I am indebted to many people for their enthusiastic support and guidance. I would especially like to thank Professor Anthony Evans who advised me, even after he left UCSB, and was always dedicated to this research. Professor David Embury was my advisor while I was working at the Los Alamos National Laboratory (LANL). I could not have completed this work without the constant encouragement and interest from Professor Embury. I cannot say enough about the advice and support I received from Dr. Loren Jacobson, my mentor and friend, the champion of beryllium at LANL.

My research was performed at LANL, which is supported in part by the United States Department of Energy (DOE) contract W7405-ENG-36. I am in the Metallurgy group of the Materials Science and Technology Division (MST-6) and returned for my degree under the Advanced Studies Program.

Many people at LANL provided technical assistance and advice. Special thanks to Dr. Carlos Tomé, who helped me enormously through our periodic discussions.

A major portion of my experimental work was performed at the LANL Manuel Lujan Jr. Neutron Scattering Center (LANSCE). This is a national user facility funded by the DOE, Office of Basic Energy Science and Defense Programs. Special thanks to Dr. Mark Bourke at LANSCE who helped me set up and run the experiments. He was very interested in my research and especially helpful in interpreting the results.

I am especially grateful to the people in the metallography and characterization section of our group. I had many useful discussions with Dr. Robert Field,

who also assisted me with transmission electron microscopy. Dr. Ke Han, LANL Center for Materials Science, was also very helpful with my microscopy studies. I am very thankful for Ann Kelly and Pallas Papin who helped me with sample preparation as well as microscopy.

Paul Stanek was instrumental in developing the centrifugal gas atomization capability at LANL and provided the Be-Al materials for my research. Steve Abeln has also been very supportive of my work. I am grateful for the collaborations with many people at Starmet (formerly Nuclear Materials) and Brush Wellman.

I want to thank my current and former supervisors at LANL for their dedication to the Advanced Studies Program and their continuous support. I am particularly grateful to Richard Mah, Raymond Dixon, and Dr. Tony Rollett.

[redacted]

[redacted]

1987	Bachelor of Science Materials Science and Engineering Massachusetts Institute of Technology Cambridge, Massachusetts
1988	Master of Science Materials Science and Engineering Massachusetts Institute of Technology Cambridge, Massachusetts
1988–Present	Technical Staff Member Materials Science and Technology Division Los Alamos National Laboratory Los Alamos, New Mexico

Selected Publications

"SiC Whisker-Reinforced $MoSi_2$." D. H. Carter. Masters thesis, Massachusetts Institute of Technology. *Los Alamos Report LA-11411-T,* 1988.

"Mechanical behavior of beryllium-aluminum composites." D. H. Carter, L. A. Jacobson, and P. W. Stanek. *Proceedings of the Tenth International Conference on Composite Materials, Whistler, British Columbia, Canada, 14–18 August 1995.* Vol. 2, *Metal Matrix Composites,* (401–408). Edited by A. Poursartip and K. Street. Cambridge, England: Woodhead Publishing Limited, 1995.

Contents

List of Figures

List of Tables

Deformation of a Beryllium-Aluminum Composite

By

David H. Carter

ABSTRACT

The physical and mechanical properties of beryllium, especially the combination of low density and high elastic modulus, make it an attractive candidate for a structural material. Intrinsic problems exist with Be as a monolithic material, as its structural behavior is complex due to its hexagonal close-packed crystal structure. Therefore, great value may be found in investigating composites of Be, such as beryllium-aluminum. However, one needs to understand the behavior of the individual phases in a Be composite and their interaction during the sequence of elasticity, plasticity, and fracture. The approach taken in this dissertation was to use neutron diffraction to monitor the elastic loading of each phase, in combination with detailed studies of the composite's mechanical behavior for strains up to 5%. In addition, the experiments were performed on a unique type of composite microstructure. This consisted of interpenetrating phases formed from liquid immiscibility, rather than conventional powder processing, which is limited by reactions at interfaces. The results were interpreted in terms of plasticity models and finite element calculations that describe the interaction between the phases and the local stress states established by compatibility requirements between the phases.

Neutron diffraction studies of a compression test on a Be-Al composite showed that the Be deformed plastically at −200 to −250 MPa, and the Al developed large hydrostatic stress components. Finite element analyses using a relatively simple model simulated this behavior quite well.

The tensile elongation of this rapidly solidified Be-Al composite was on the order of 10%, with yield strengths of 300–400 MPa, whereas the elongation of Be produced by the same rapid solidification process was only 1% at its ultimate strength of 400 MPa. The mechanical behavior of this composite was largely influenced by constraints developed during deformation. These constraints were very complex and had a number of origins. *(i)* Beryllium has some unique elastic properties including a high elastic modulus and a low Poisson's ratio. *(ii)* The microstructure and morphology of the composite consisted of an interpenetrating network of two continuous phases with a very fine grain size. *(iii)* The Al was constrained during plastic flow, yet accommodated compatible deformation in the Be.

Chapter 1

Introduction

Beryllium is of interest in aerospace and military applications as well as specialized commercial applications because of its unique set of properties (see Table 1.1). These include very low density, high strength and stiffness, and high thermal conductivity. At room temperature, polycrystalline Be fails by cleavage at elongations of only about 3%. Accordingly, when used for structural applications, it must be designed using a brittle material methodology. Much effort has been spent improving the ductility of Be, with limited success. Alternatively, Be can be combined with another material in a composite in order to enhance its toughness and ductility while substantially maintaining its attractive properties. Beryllium-aluminum (Be-Al) is one such composite. This material has been studied since the 1960's, commencing with the advent of Lockalloy—a powder metallurgy product with composition Be-38Al[1]. Although this product was used in some military applications, its low strength and fracture properties limited its insertion into a wider range of applications.

[1]All chemical compositions are given in weight percent unless otherwise indicated.

Table 1.1: Some properties of beryllium

Density (g/cm^3)	1.848
Young's modulus (GPa)	300
Poisson's ratio	0.03
Yield strength (MPa)	345
Ultimate strength (MPa)	450
Elongation (%)	3
Melting temperature (°C)	1278
Thermal expansion coefficient at 25 °C (10^{-6} K^{-1})	11.6
Thermal conductivity at 25 °C (W m^{-1} K^{-1})	208

Recent advances in processing techniques (such as rapid solidification) have improved the properties of Be-Al materials. The focus of the present research is on one such composite, having composition Be-47.5Al-2.5Ag, produced by the hot isostatic pressing of a powder fabricated by rapid solidification using a centrifugal atomization process. The minor additions of silver were used to study the effects of age-hardening of the Al on the overall properties. The tensile elongation of this rapidly solidified Be-Al composite was on the order of 10%, with yield strengths of 300–400 MPa, whereas the elongation of Be produced by the same rapid solidification process was only 1% at its ultimate strength of 400 MPa.

The Be-47.5Al-2.5Ag composite has an uncommon morphology because of liquid phase separation. The microstructure comprises a fine, three-dimensional interpenetrating network.

The purpose of the present study was to understand the behavior of the individual phases in a Be composite and their interaction during the sequence

of elasticity, plasticity, and fracture. The approach taken was to follow the deformation behavior of the individual phases by utilizing neutron diffraction techniques.

To quantify the deformation behavior, *in situ* neutron diffraction measurements were taken of the elastic strains during loading. This is an ideal technique for studying the deformation because it distinguishes between phases and measures strain in all possible crystallographic orientations. Moreover, unlike x-rays which are typically limited to near surface regions, neutrons provide a volumetric or bulk average strain. These strains were compared with predictions from finite element analyses to clarify the stress state in each phase during deformation.

Two possible explanations may account for the order of magnitude higher strains in Be-Al composites compared to pure Be. *(i)* Extensive microcracking may occur in the Be phase, such that plastic strain occurs mainly in the Al, and the Be accommodates that strain without undergoing catastrophic failure. *(ii)* Compatible plastic deformation occurs in both phases. To distinguish between these two possibilities, one experiment comprised a cyclic tensile test, along with microscopy, to demonstrate that minimal microcracking accompanies plastic straining up to 8%. That is, all of the strain is caused by compatible plastic deformation of both the Al and Be phases.

Detailed microstructural characterization was also performed using scanning electron microscopy. The morphology of the composite was studied by etching away one phase and closely examining the remaining phase.

This dissertation is organized as follows. Chapter 2 contains background information and a review of the relevant literature, including properties of Be

and past work on the Be-Al system. Neutron diffraction studies of deformation in composites will be described. Relevant deformation mechanisms will also be reviewed. Chapter 3 describes the experiments and results. The major portion of this work consisted of *in situ* neutron diffraction loading experiments. This chapter also includes details on tensile, compression and bend properties; the cyclic tensile test; the etching experiment; and microscopy studies. Chapter 4 presents various physical and numerical models used to describe the results from the experiments. This is followed by a discussion of the results, with an emphasis on relating the deformation behavior to the mechanical properties of Be-Al composites. Chapter 5 presents a summary of the important conclusions and recommendations for future work.

Chapter 2

Background and Literature Review

2.1 Introduction

Four separate topics will be reviewed. The Be and Be-Al systems will be described, with an emphasis on their mechanical properties and deformation behavior. The development of Be-Al composites will be described. The use of neutron diffraction to study deformation of composites will be discussed. Finally, relevant theories of deformation in two-phase materials will be reviewed. This review will provide a starting point for the development of a physically-based deformation model, to be discussed in Chapter 4.

2.2 Properties of beryllium

An extensive treatise on Be science and technology has been compiled [1, 2]. Volume 1 (of the two volume series) contains reviews of the flow and fracture properties of single-crystal and polycrystalline Be, grain size and impurity effects, recrystallization and grain growth, the constitution of Be and its alloys, and the elevated temperature behavior of Be.

A number of factors cause Be to be brittle at room temperature. The primary cause in single-crystal Be is the nature of its interatomic bonding, which results in a propensity for basal plane cleavage. Namely, the small ratio of bulk to shear modulus (K/μ) (small Poisson's ratio) implies a preference for brittle fracture rather than plasticity [3, 4]. Other contributing factors include the limited number of slip systems and the predominance of basal plane slip. In polycrystalline Be, ductility is also controlled by factors such as grain size, texture, impurities, and the orientation of grains that provide compatible deformation.

2.2.1 Single-crystal Be

Crystal structure

Beryllium has a hexagonal close-packed (hcp) structure, an ABAB stacking of closely packed planes, shown in Figure 2.1 where the axes c and a are identified. The structure is depicted in this illustration as a hexagonal prism with three unit cells. Two atoms are associated with each lattice point and are located at coordinates (0,0,0) and ($\frac{2}{3}$,$\frac{1}{3}$,$\frac{1}{2}$). The lattice parameters of Be are $a = 2.2854$ Å and $c = 3.5829$ Å.

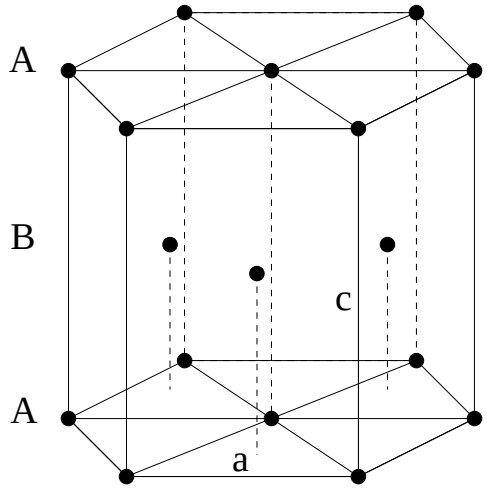

Figure 2.1: Hexagonal close-packed structure of Be

Elastic properties

The elastic constants of Be have been measured acoustically by a pulse-echo-overlap technique and are tabulated in Table 2.1 [5]. The values for bulk modulus (K), shear modulus (μ), Young's modulus (E), and Poisson's ratio (ν) were calculated from weighted averages of the measured single-crystal elastic constants using Voigt's isostrain assumption (Table 2.2 [5]). The calculated Poisson's ratio (ν) is 0.02, whereas most metals have a ν of about 0.3. Beryllium is also unique by virtue of its large stiffnesses (such as C_{11}) but small coupling between modes, indicated by the small C_{12} and C_{13}. The small C_{13} implies that stresses applied normal to the basal plane are not transferred into directions within the plane.

The theoretical dependence of Young's modulus on orientation can be calculated from the elastic compliances (S_{ij}) as [6]

$$\frac{1}{E} = S_{11}(1-\gamma^2)^2 + S_{33}\gamma^4 + (2S_{13} + S_{44})\gamma^2(1-\gamma^2) \tag{2.1}$$

Table 2.1: Measured elastic constants of Be (from [5])

Elastic stiffness (GPa)					
C_{11}	C_{33}	C_{44}	C_{66}	C_{12}	C_{13}
295.4	356.1	170.6	134.8	25.9	-10 ± 20
Elastic compliance (10^{-3} GPa^{-1})					
S_{11}	S_{33}	S_{44}	S_{12}	S_{13}	
3.411	2.808	5.862	-0.299	0.01	

Table 2.2: Calculated elastic properties of Be (from [5])

K (GPa)	μ (GPa)	E (GPa)	ν
110	156	318	0.02

for hexagonal crystals where γ is the cosine of the angle formed with the c-axis. Only one angle appears in this formula because the elastic properties have rotational symmetry with respect to this axis. Substituting the values from Table 2.1 into Equation 2.1, Young's modulus is plotted for single-crystal Be as a function of orientation in Figure 2.2. Young's modulus is relatively isotropic, with a maximum in the c-axis direction and a minimum in a direction perpendicular to the c-axis. From this equation, $E_{min} = 293$ GPa and $E_{max} = 356$ GPa.

The thermal expansion coefficient is anisotropic, with a 15% difference in the expansion coefficients of the major crystallographic directions. Measurements on high-purity single crystals showed that in a direction parallel to the c-axis, $\alpha_{\parallel} = 10.076 \pm 0.026 \times 10^{-6}$ K^{-1}, and perpendicular to the c-axis, $\alpha_{\perp} = 11.580 \pm 0.050 \times 10^{-6}$ K^{-1} [7].

Bonding within the basal plane has been described as metallic, but across the basal plane, along the c-axis, it has covalent characteristics. This implies that bonds across the basal plane can undergo little stretching before fracture [8]. This

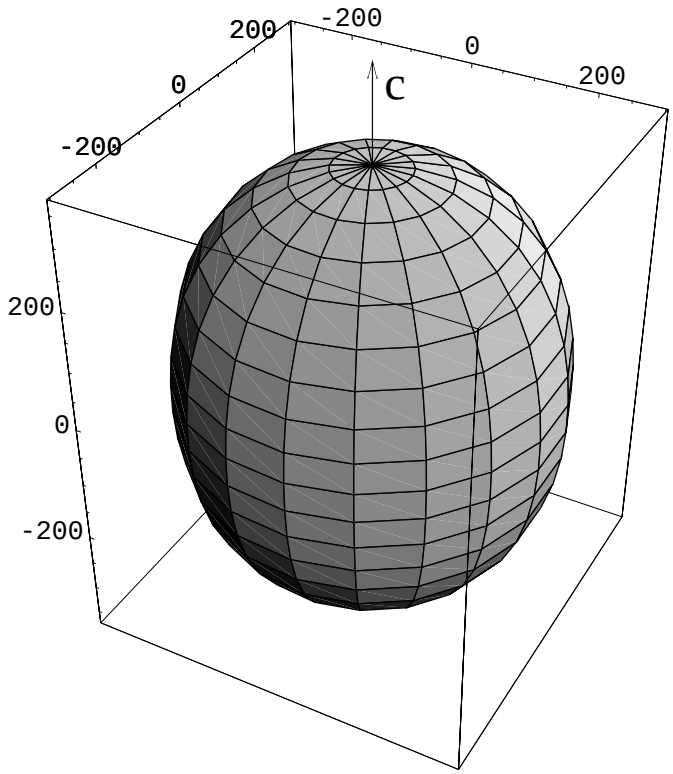

Figure 2.2: Young's modulus (GPa) of Be as a function of orientation

Table 2.3: Ductility correlation for hcp metals (from [3, 4, 9])

Element	c/a	Primary slip mode	K/μ	Ductility
Cd	1.886	Basal	2.03	Fair
Zn	1.856	Basal	1.59	Brittle
Co	1.623	Basal	2.43	Fair
Mg	1.623	Basal	1.92	Fair
Re	1.615	Both basal and prismatic	1.76	Fair
Zr	1.593	Prismatic	2.58	Ductile
Ti	1.587	Prismatic	3.25	Ductile
Hf	1.581	Prismatic	3.58	Ductile
Os	1.579	—	1.67	Brittle
Be	1.568	Basal	0.87	Brittle

also leads to a "flattened" crystal structure, with a very low c/a ratio (1.568).

In addition, the ratio of bulk modulus to shear modulus for Be ($K/\mu = 0.87$) is the lowest of any hcp metal. The bulk modulus is the binding energy of an atomic structure and, therefore, can be correlated with the energy required to create new surfaces during cleavage fracture [9]. The shear modulus can be correlated with the energy required to move dislocations. Therefore, metals with low values of K/μ should be more brittle [10], as demonstrated in Table 2.3 [3, 4, 9].

Deformation modes

The anisotropy of slip systems in Be also helps explain its brittle nature [11–13]. Hexagonal close-packed metals have primary slip systems that are either $(0001)\langle 11\bar{2}0\rangle$ (basal) or $\{10\bar{1}0\}\langle 11\bar{2}0\rangle$ (prismatic). In an ideal hcp structure, the c/a ratio is $\sqrt{8/3} = 1.633$. Hexagonal metals with lower c/a ratios provide primary slip on the prism plane (see Table 2.3). This occurs because low c/a ratios indicate larger distances between prismatic slip planes, and the Peirels-

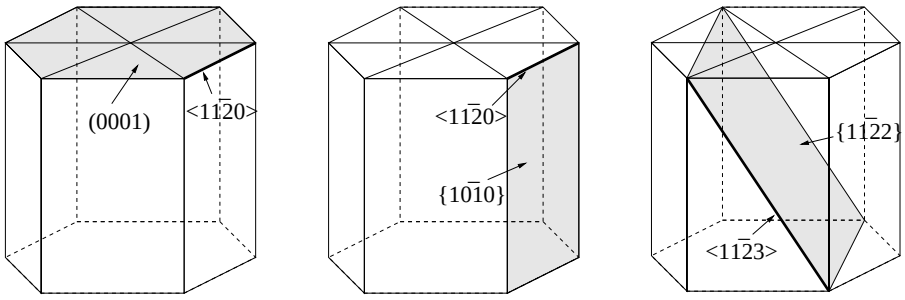

(a) Primary slip on basal planes $(0001)\langle 11\bar{2}0\rangle$, two independent slip systems

(b) Secondary slip on prism planes $\{10\bar{1}0\}\langle 11\bar{2}0\rangle$, two independent slip systems

(c) Secondary $(c+a)$ slip on second-order pyramidal planes $\{11\bar{2}2\}\langle 11\bar{2}3\rangle$, five independent slip systems

Figure 2.3: Primary and secondary slip systems in Be

Nabarro stress is lowest for planes with the greatest interplanar spacing [8]. Beryllium has the smallest c/a ratio (1.568) of any element, yet the primary slip mode is basal. The reason for this is not well understood [4, 14].

The primary and secondary slip systems in Be (basal, prism and second-order pyramidal) are shown in Figure 2.3. Slip on first-order pyramidal planes $\{10\bar{1}1\}$ is not as important in Be, because this system consists only of combinations of basal and prism slip. Accordingly, Be has only four independent slip systems. The Taylor-von Mises criterion for arbitrary deformation requires five independent slip systems; otherwise, deformation has to be accommodated cooperatively by neighboring grains with different orientations. However, $(c+a)$ type dislocations with a Burgers vector inclined to the basal plane could occur on the second-order pyramidal plane in Be. This is the only mode which provides five independent slip systems [15].

Measurable plasticity associated with a non-basal slip direction can occur in high-purity single crystals even at room temperature; however, the stress level at which this occurs is very high [16]. This is illustrated in Figure 2.4 [8], which shows that at room temperature, the flow stress, or critical resolved shear stress (CRSS), for basal slip (1.3 MPa) is more than an order of magnitude less than prismatic slip (51 MPa) and much lower than $c + a$ slip (2176 MPa). Yet, Be exhibits a brittle to ductile transition at 200 °C even though the CRSS for $c + a$ slip is still relatively high at this temperature. Consequently, below 200 °C, in polycrystalline Be, measured strains comprise basal slip in isolated grains combined with lattice bending.

The micro elastic limit (MEL) shown in Figure 2.4 is the stress at which the stress-strain curve first deviates from linear elastic behavior. The CRSS, or the macro elastic limit, is the intercept of the elastic loading line with the final slope of the stress-strain curve.

Reducing impurities lowers the CRSS for slip, but affects basal slip the most, causing an even greater plastic anisotropy. Although lowering the CRSS causes an increase in elongation, the fracture stress remains constant [9]. Therefore, increased purity decreases the work-hardening rate for single-crystal Be. This effect would not be observed in polycrystalline Be, in which large numbers of randomly oriented grains favor basal cleavage.

For perfectly oriented crystals, the CRSS for prismatic slip is anomalous (shown in Figure 2.4): namely, a maximum occurs just above room temperature. Mechanisms for this anomaly have been hypothesized [17]. The flow stress for pyramidal slip (Figure 2.4) also demonstrates anomalous behavior above room

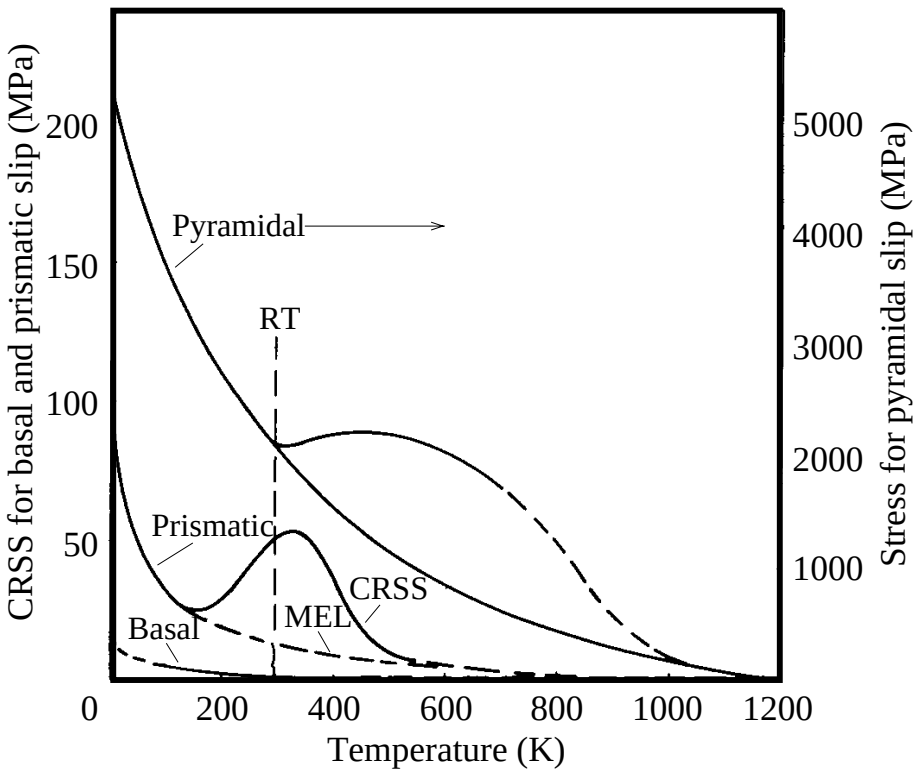

Figure 2.4: Flow stress vs. temperature for basal, prismatic, and pyramidal $c+a$ slip in high-purity Be. MEL is the micro elastic limit and CRSS is the critical resolved shear stress (from [8]).

temperature. The reason is not understood.

Cleavage fracture

The primary fracture mode in single-crystal Be at room temperature is basal plane cleavage. In Be, the basal plane has the lowest surface energy ($\gamma_{(0001)} = 2322$ erg/cm^2, $\gamma_{(10\bar{1}0)} = 6342$ erg/cm^2, and $\gamma_{\{11\bar{2}2\}} = 11,851$ erg/cm^2) [18].

The brittle nature of hexagonal metals is enhanced if both slip and cleavage occur on the same lattice plane, whereas those metals that slip primarily on prismatic planes do not undergo basal plane cleavage as readily [8,19]. Furthermore, if $(c+a)$ slip is difficult to activate, as in Be, no slip mechanism for crack blunting exists and basal cleavage may propagate easily.

Fracture in Be is initiated by a process known as bend plane splitting, shown in Figure 2.5 [18]. Tensile elongation by basal slip causes the basal planes to rotate and introduces bending of the slip planes. Bend planes have sharp discontinuities and, under further deformation, may easily initiate basal cleavage. If the Stroh criterion is satisfied, cleavage will cause failure [19]. This criterion is given as

$$\sigma_n \geq \frac{4\gamma\mu\cos\theta}{\pi D\tau_s} \tag{2.2}$$

where σ_n is the applied normal stress, γ is the basal plane surface energy, μ is the shear modulus, θ is the angle between the basal plane and the tensile axis, D is the grain size, and τ_s is the effective resolved shear stress.

The energy to both initiate and propagate cleavage cracks on the basal plane was measured as approximately 2100 erg/cm^2 [20], in close agreement with the theoretical cleavage surface energy of the (0001) plane.

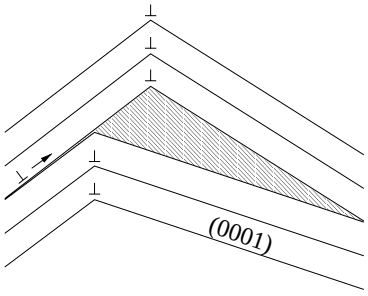

(a) Nucleation of basal cleavage by bend plane splitting

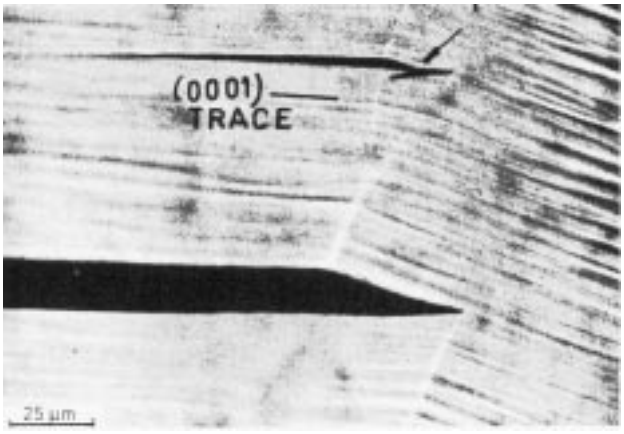

(b) Optical photograph of basal plane cracks formed by bend plane splitting (from [18])

Figure 2.5: Stroh fracture mechanism in Be

Twinning

Twinning occurs on the $\{10\bar{1}2\}$ planes and results in some plastic deformation along the c-axis. Because of the low c/a ratio, twinning causes an extension of the c-axis and compression of the a-axis. Twinning, therefore, can be observed when conditions are favorable for c-axis expansion: under c-axis tension or a-axis compression.

Twinning provides little enhancement to deformation in polycrystalline Be, where the random orientation of c-axes results in only $\sim 1\%$ additional overall deformation. In addition, basal plane cleavage often occurs before twinning when a crystal is loaded in c-axis tension. Therefore, unlike in other hcp metals, twinning can actually promote cracking in polycrystalline Be, rather than provide substantial plasticity.

2.2.2 Bicrystals

A series of experiments has been performed on high-purity Be bicrystals, carefully oriented so that the Taylor-von Mises criterion could be satisfied by only two slip systems, a simple tilt boundary [21].

It was found that even in circumstances where strain compatibility conditions were easily satisfied, the presence of a grain boundary reduced the tensile elongation by nearly an order of magnitude. This indicates that even for high-purity Be, simply meeting macroscopic strain compatibility requirements may not produce ductile behavior.

2.2.3 Polycrystalline Be

In polycrystalline Be, the room temperature ductility is dependent on impurity content, texture, and grain size. Therefore, there is a substantial variation in the tensile stress-strain curves reported in the literature. Table 2.4 shows typical properties of different commercially available forms of Be [22]. Some of the common impurities in Be are oxygen in the form of BeO inclusions, C, Fe, Al, Si, and Mg. The effects of each of these impurities on mechanical behavior are well characterized [23, 24].

Significant gains in ductility can be achieved through texture. Normally, however, such increases are directional, so an increase in ductility in one direction comes at the expense of decreased ductility in one of the other orthogonal directions within the material. Rolling, for example, produces a very fine grain size and basal texture within the plane of the rolling direction. This texture gives in-plane ductility, but the ductility in the through-thickness direction is

Table 2.4: Typical tensile properties of commercially available forms of Be (from [22])

Material	Test direction	Ultimate tensile strength (MPa)	0.2% Yield strength (MPa)	Elongation (%)[a]
Block				
normal-purity (hot-pressed)[b]				
structural grade	L[c]	370	266	2.3
	T	390	273	3.6
thermal or brake grade	L	294	196	2.7
	T	322	196	4.6
high-purity (isopressed)	L	455	287	3.9
	T	455	287	4.4
high-oxide instrument grade				
(hot-pressed)	L	476	406	1.5
	T	511	413	2.7
fine grain size (isopressed)	L	580	407	3.7
	T	587	407	4.2
Sheet (1–6.35 mm thick)				
normal-purity powder		531	372	16
normal-purity ingot		352	172	7
Extrusions				
normal-purity powder		655–690	345–518	8–13
high-purity powder		655–828	345–518	8–13
Forgings				
normal-purity		483–600	435–600	0–4.5
Wire (50–635 μm diameter)				
high-purity ingot		966	793	3

[a]Elongation in 50 mm, except 250 mm for wire.

[b]Structural grade contains about 1.8% BeO and thermal or brake grade about 0.9%.

[c]L and T refer to longitudinal and transverse test directions.

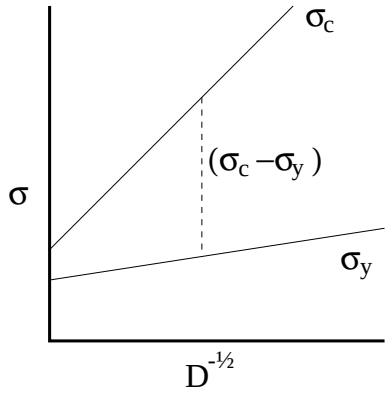

Figure 2.6: The Hall-Petch stress-grain size dependence in Be. σ_c is fracture stress, σ_y is yield stress, and D is average grain size.

considerably less.

The grain size in Be governs both the flow and fracture strengths through a Hall-Petch relationship. That is, strength is proportional to $D^{-1/2}$, where D is the average grain diameter, when other variables such as impurity content and texture are constant [25].

Grain size also has an effect on ductility. The Hall-Petch slope for fracture stress (σ_c) is considerably higher than the Hall-Petch slope for yield stress (σ_y). This is shown in Figure 2.6 where $(\sigma_c - \sigma_y)$ is plotted vs. $D^{-1/2}$. It has also been shown that elongation (ε_f) increases with an increase in $(\sigma_c - \sigma_y)$, as shown in Figure 2.7 [25]. Because $(\sigma_c - \sigma_y) \propto D^{-1/2}$ and $(\sigma_c - \sigma_y) \propto \varepsilon_f$, it follows that grain refinement should result in improved ductility.

2.2.4 Summary

Be has some unusual properties because of the anisotropic nature of its atomic bonding. These include an unusually high stiffness in the primary crystallo-

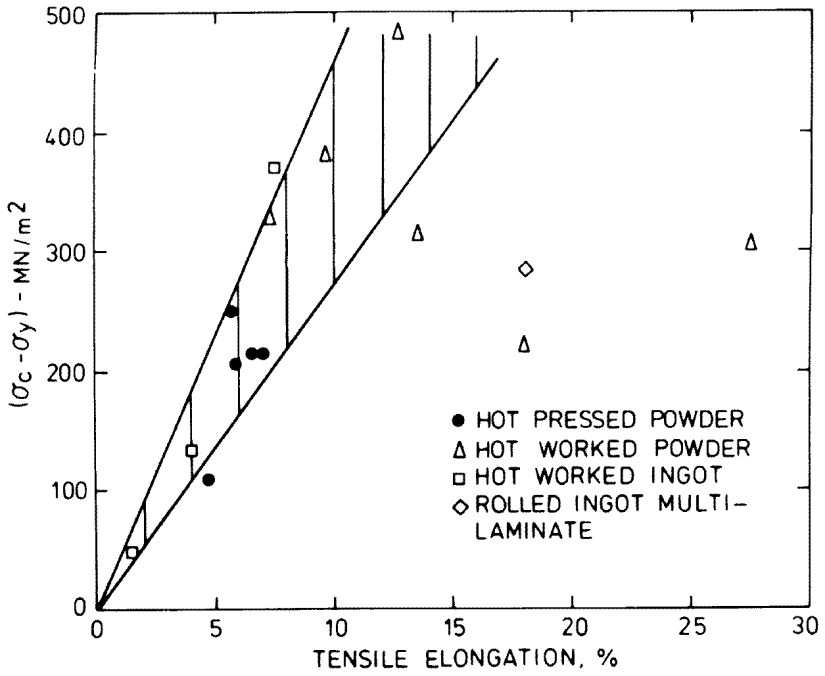

Figure 2.7: Relation between $(\sigma_c - \sigma_y)$ and tensile elongation for Be (from [25])

graphic directions, but a very low coupling between these directions. This results in a very low K/μ and ν. In addition, the limited number of available slip systems and the anisotropy of the stresses required for slip on nonbasal slip systems lead to the preference of basal slip.

The preferred slip plane is also the preferred cleavage plane. Because basal slip does not allow arbitrary three-dimensional deformation, polycrystalline Be will undergo basal plane cleavage when neighboring grains are not oriented correctly for basal slip. Therefore, Be normally fractures via basal plane cleavage.

By combining Be with Al, as in the composite studied in this work, the ductility of Be is enhanced for two reasons. *(i)* The grain size of the Be in this rapidly solidified composite is much smaller than in typical monolithic Be and raises the fracture stress for Be because of the Stroh criterion (Equation 2.2). *(ii)*

In polycrystalline Be, mismatches in orientation of the Be grains do not allow compatible deformation to occur, and fracture initiates at grain boundaries that are not oriented preferentially for plastic deformation. In this composite, each Be grain is embedded in Al, which flows readily and allows the Be to deform in arbitrary directions. This greatly reduces the problems caused by mismatches in the orientation of Be grains by allowing compatible plastic deformation.

2.3 Beryllium-aluminum composites

2.3.1 Motivation

The specific stiffness of Be is much higher than that of many commonly used metals and metal alloys (Figure 2.8 [26]). Materials are normally chosen for a combination of properties that maximize their performance, rather than a single property. For example, the stiffest material is the one with the highest value of E, but the best materials for a light, stiff beam or column are those with the greatest value of the "performance index" $E^{1/2}/\rho$ [26]. A performance index is derived by considering the component's functional requirements, geometric parameters, and material properties. Two other indices relating to light, stiff components are E/ρ and $E^{1/3}/\rho$ which, when maximized, give the best slender ties and plates, respectively.

By plotting E and ρ on log scales, a family of parallel lines can be drawn for each of the indices. Each line represents a constant value of the index. Therefore, materials above a particular index are preferred. Consider the index for light stiff beams, $E^{1/2}/\rho$. If a family of parallel lines are drawn for this index, Be is one of

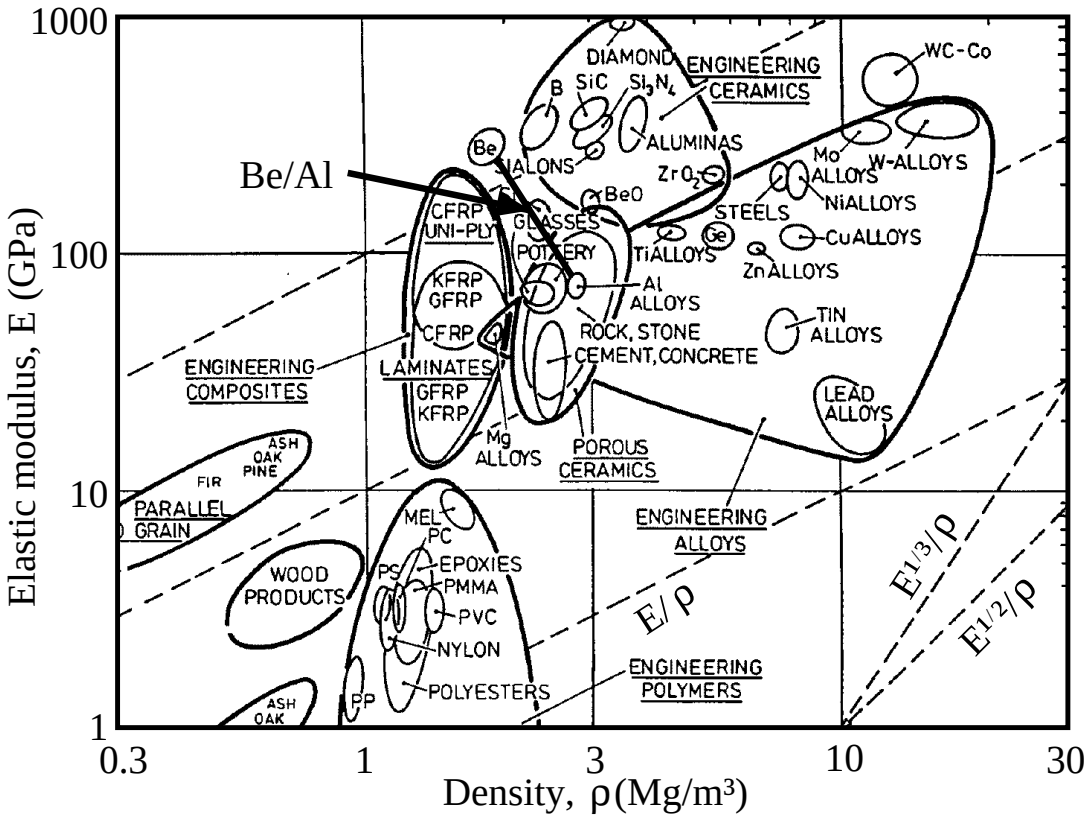

Figure 2.8: Specific stiffness of engineering materials (from [26])

the best materials.

By combining Be with Al, a composite with a high specific stiffness and good ductility can be designed. This is the fundamental motivation for designing a composite with Be and Al. The specific stiffness of the resulting composite depends on the morphology of the phases and the volume fraction of each phase.

If a volume fraction f of a reinforcement r with a density ρ_r is mixed with a volume fraction $(1-f)$ of a matrix m with a density ρ_m to form a composite with no porosity, its density is given exactly by the rule of mixtures,

$$\rho = f\rho_r + (1-f)\rho_m \tag{2.3}$$

It does not depend on the morphology of the phases.

The Young's modulus of a composite can be explored using the well-known Voigt (upper) and Reuss (lower) bounds (although more closely spaced bounds do exist). The upper bound (E_u) is an isostrain model and the composite stress is the volume average of the local stresses. The elastic modulus is given by

$$E_u = fE_r + (1-f)E_m \tag{2.4}$$

where E_r and E_m are the Young's moduli of the reinforcement and matrix, respectively.

The lower bound (E_l) is an isostress model and the composite strain is the volume average of the local strains. The elastic modulus is given by

$$E_l = \frac{E_m E_r}{fE_m + (1-f)E_r} \tag{2.5}$$

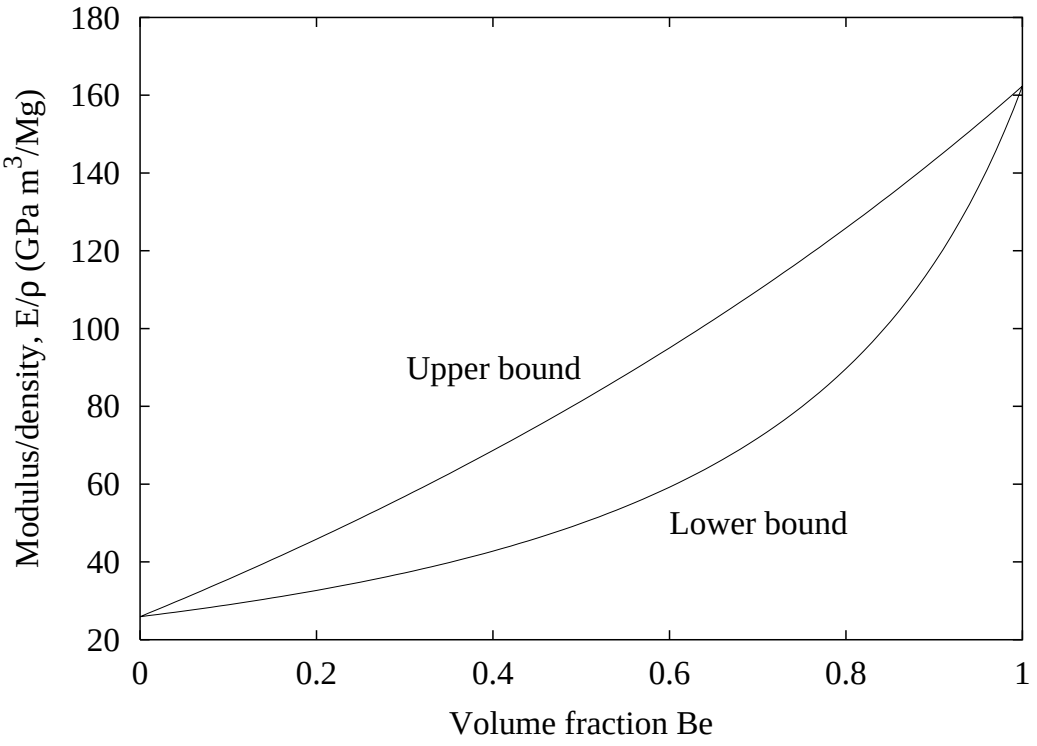

Figure 2.9: Upper bound (Equations 2.3 and 2.4) and lower bound (Equations 2.3 and 2.5) of specific stiffness vs. volume fraction of Be in a Be-Al composite

Using Equations 2.3, 2.4, and 2.5, envelopes can be constructed for the specific stiffness (Figure 2.9).

Figure 2.10 [27] is a small portion of Figure 2.8 that shows envelopes describing the modulus-density relationship in the Be-Al and Al-Al_2O_3 systems. The two sides of the envelopes represent the upper and lower bounds.

By superimposing the performance index $E^{1/2}/\rho$ on this figure, the effect of combining materials to form composites can be illustrated. It is evident that the performance index of Al is much more effectively improved with the addition of Be than with the addition of Al_2O_3. The notations, fibers and particles, indicate that using fibers provides a longitudinal composite modulus closer to the

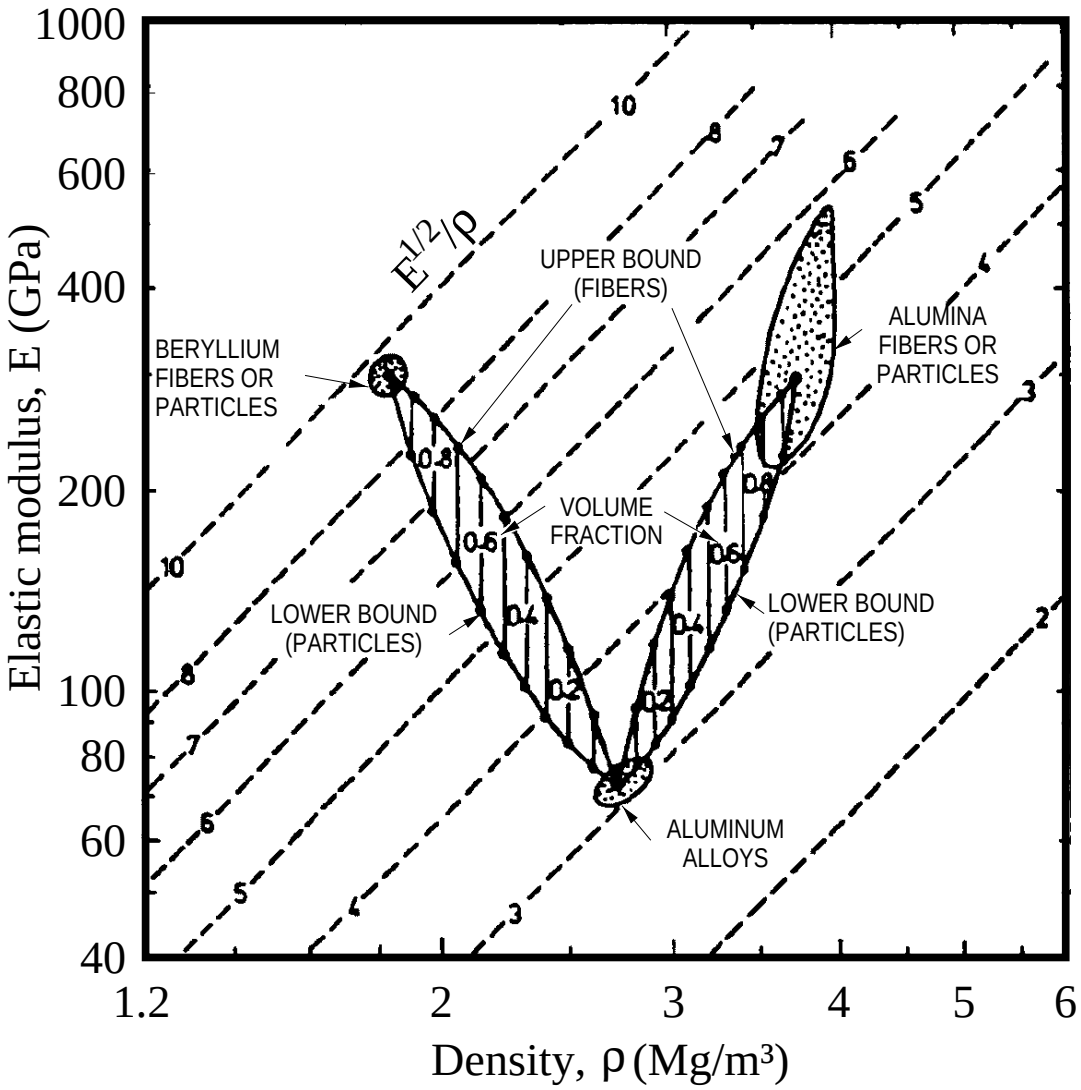

Figure 2.10: A small part of the modulus-density space, showing aluminum alloys, beryllium, alumina, and composite envelopes described by Equations 2.3–2.5 (from [27])

upper bound, and using particles (or fibers when loaded transversely) provides a composite modulus closer to the lower bound [27].

The upper bound for the strength of a composite (σ_u) is a rule of mixtures of the strength of the reinforcement (σ_r) and matrix (σ_m) as

$$\sigma_u = f\sigma_r + (1-f)\sigma_m \tag{2.6}$$

The lower bound (σ_l) is the yield strength of the matrix, enhanced by the plastic constraint imposed by the reinforcement [27], or

$$\sigma_l = \sigma_m \left[1 + \frac{1}{16}\left(\frac{f^{1/2}}{1-f^{1/2}}\right)\right] \tag{2.7}$$

It has been shown that bounds for composite properties can be modified by incorporating simple scaling laws [28]. If the effect of scale on the strength of either the matrix or reinforcement is known, this effect can be incorporated into the upper and lower bounds for the strength of the composite (Equations 2.6 and 2.7). This was done for particulates of Be in an Al matrix [28]. The analysis is reproduced here.

The Be was assumed to follow a Hall-Petch relationship for yield strength, given (in MPa) as [29]

$$\sigma_r = 114 + \frac{0.37}{d^{1/2}} \tag{2.8}$$

It was assumed in this analysis that the grain size d is replaced by particle size r, and that the maximum d is 10 μm.

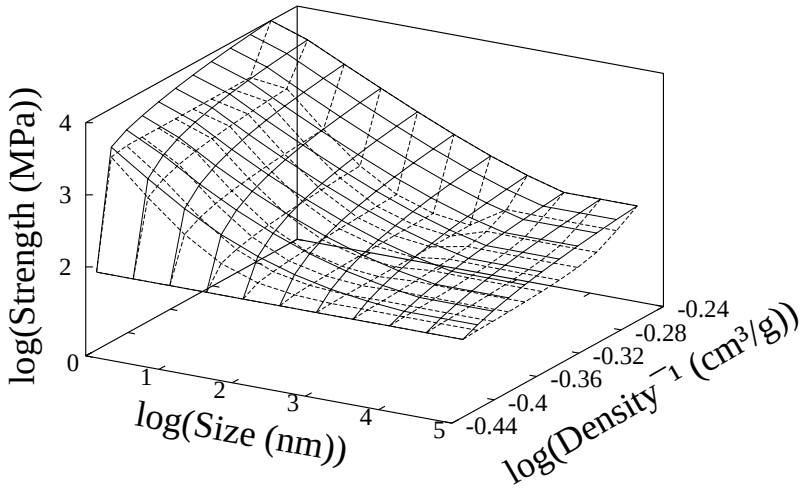

Figure 2.11: Scale dependent design chart for Be-Al (after [28])

The strength of the Al was described by the equation for Orowan bowing [30]

$$\sigma_m = \sigma_\circ + \frac{Eb}{3l} \tag{2.9}$$

In this equation, b is the Burgers vector for the matrix and l is the spacing between particles. l is a function of volume fraction f and particle size r, given by

$$l = \frac{(2\pi)^{1/2} r}{(3f)^{1/2}} \tag{2.10}$$

The expressions for σ_r and σ_m were substituted into Equations 2.6 and 2.7 for particle sizes ranging from 100 to 0.001 μm, and plotted as a three-dimensional surface in Figure 2.11 as strength vs. particulate size and composite density. For submicron particle sizes, the matrix strength was used instead of Equation 2.7. For clarity, the reciprocal of composite density was plotted.

2.3.2 Historical development

The possibilities of combining Be with Al to take advantage of the high specific stiffness and strength of Be and the ductility of Al have been recognized for many years. In fact, a patent related to the Be-Al system was awarded in 1918 [31].

Be-Al composites were first used during the 1960's and 1970's in military applications, when Lockalloy was developed by Lockheed Missiles and Space Company for the Minuteman III Missile [32] and the YF-12 Ventral Fin (SR-71 Blackbird) [33]. Lockalloy had the composition Be-38Al, which was chosen because this material had an elastic modulus of 180 GPa, similar to steel, which made it easier to insert into existing designs. Its specific stiffness, however, was almost four times greater than that of steel.

No further major developments occurred until the early 1990's, when advances in processing techniques enabled the commercial viability of two different types of Be-Al. Brush Wellman Inc. currently produces a powder metallurgy family of alloys with a tradename AlBeMet, which is fabricated by rapid solidification of pre-alloyed Be-Al, followed by hot isostatic pressing [34–38]. Starmet Corporation currently produces an investment cast Be-Al with a tradename Beralcast, which can be cast into near net shapes [39–45].

Current research efforts by both producers include using small ternary additions to improve processibility as well as the properties of the resultant composite. For example, Beralcast 363 has minor additions that are given as ranges in weight percent, such as Be-(27.5–34.5)Al-(2.65–3.35)Ag-(0.65–1.35)Co-(0.55–0.95)Ge [44]. Mechanical properties of AlBeMet AM162 (as HIP'd) and Beralcast 363 (as cast) are listed in Table 2.5.

Table 2.5: Properties of commercially available Be-Al (from product literature)

Property	AlBeMet AM162 (as HIP'd)	Beralcast 363 (as cast)
Composition	Be-38Al	Be-30Al-0.75Ge-3Ag-1Co
Density (g/cm^3)	2.071	2.159
Young's modulus (GPa)	179	226
Yield strength (MPa)	193	200
Ultimate strength (MPa)	262	255
Elongation (%)	2	3.5
Thermal expansion coefficient at 25 °C (10^{-6} K^{-1})	13.91	12.7
Thermal conductivity at 25 °C (W m^{-1} K^{-1})	210	108

2.3.3 Liquid phase separation

The microstructures of these two products differ because of their solidification rates (among other factors). The Be-Al phase diagram has a eutectic reaction with no compounds, very little solid solubility of Be in Al (0.3% at the eutectic temperature), and essentially no solubility of Al in Be. The microstructural length scales and phase morphologies depend on solidification rates and processing history.

It has been suggested that a metastable region of immiscibility may occur in undercooled liquids when the equilibrium system consists of a eutectic reaction involving limited solubility and a liquidus exhibiting a point of inflection [46].

This was demonstrated in the Cu-Fe and Cu-Co alloy systems [47]. Both of these systems have an equilibrium phase diagram with limited solid-solubility, a large difference in melting points of the two phases, and a liquidus exhibiting a point of inflection. In this work, liquid immiscibility was studied by measur-

ing the magnetic susceptibility as the alloys were supercooled. The supercooled state could be easily retained for about thirty minutes, so that magnetic measurements could be performed. It was found that the magnetic properties of the supercooled liquids were similar to those of normal liquids. However, once the liquids separated into two phases, the magnetic susceptibility became anomalous. Based on the magnetic properties, a liquid immiscibility limit was determined.

Liquid phase separation in these systems was confirmed by microscopic examination of quenched samples. If samples were quenched from above the immiscibility limit, small dendritic segregates were uniformly distributed throughout the sample, irrespective of whether the sample was quenched from above or below the liquidus temperature. However, if the sample was quenched after being held below the immiscibility limit, the specimen separated into two heterogeneous layers. The layers were regarded as evidence of liquid immiscibility. If the sample was immediately quenched after being rapidly cooled, the specimen did not separate into two layers, but rather formed spherical-like drops of heterogeneous phases, indicative of liquid phase separation. No estimates of cooling rate were given.

A sub-liquidus metastable liquid miscibility gap in the Be-Al system has been identified and characterized [48–55]. Figure 2.12 shows the suggested Be-Al phase diagram [55]. Using a thermodynamic approach, the critical point of this miscibility gap was calculated as 1100 °C at 68 at% Be [55]. A subregular solution model was used for this calculation with parameters from [48].

Sufficiently rapid rates of solidification can result in melt undercooling below the liquid miscibility gap, leading to the possibility of liquid phase separation.

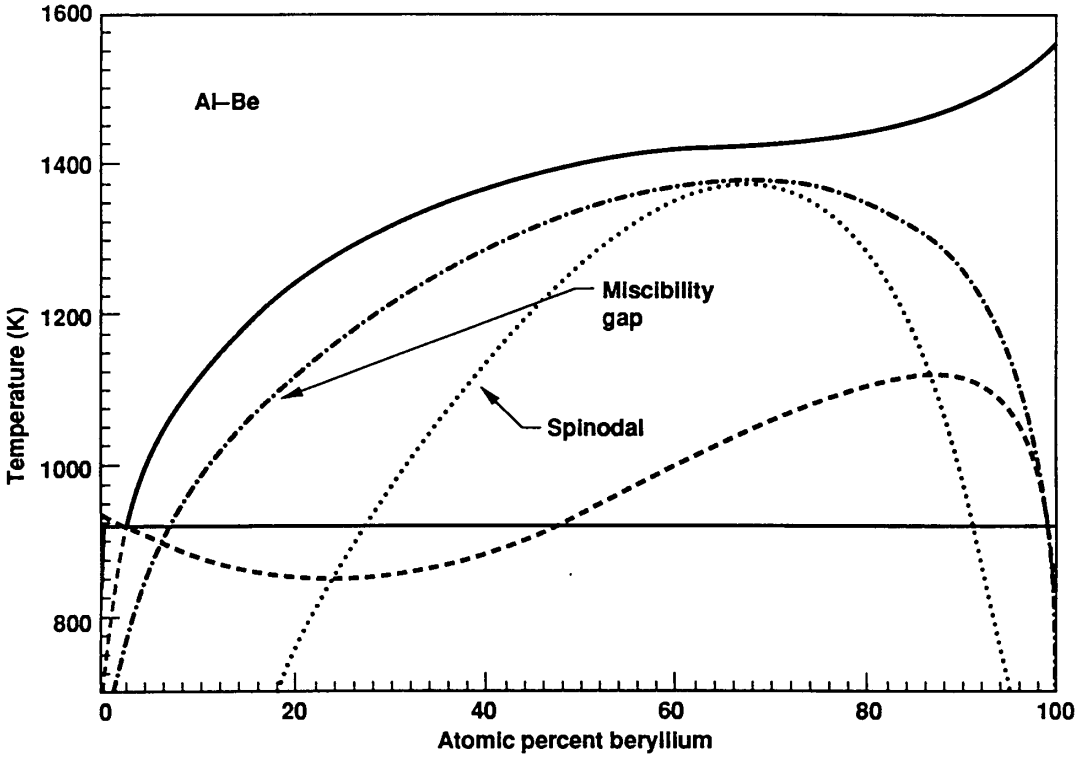

Figure 2.12: Suggested Be-Al phase diagram showing the eutectic at 2.4 at% Be and the metastable liquid miscibility gap. The solid lines represent equilibrium between the phases, the dashed lines represent the metastable-phase extensions, the dashed-dot line is the liquid phase miscibility gap, and the dotted line is the liquid-phase spinodal (from [55]).

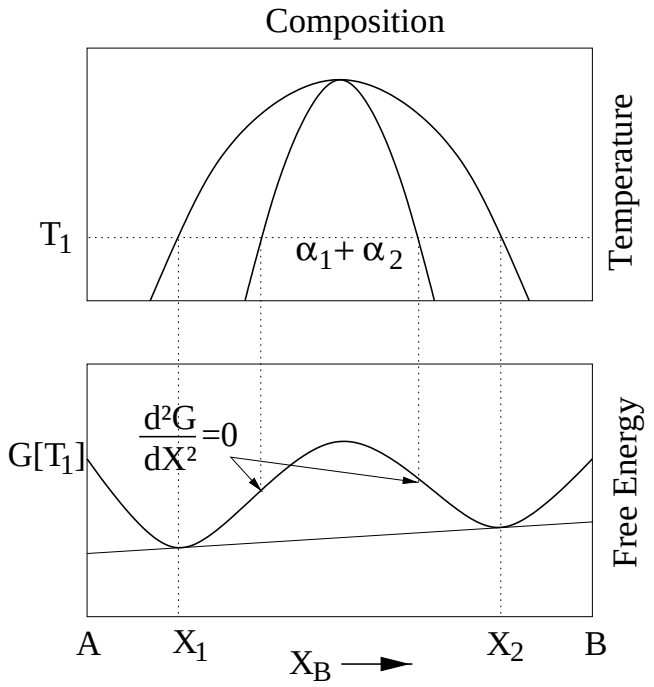

Figure 2.13: Illustration of spinodal decomposition

Within the range of spinodal decomposition, illustrated in Figure 2.13 as the inflection points on the free energy against composition plot, there is no nucleation barrier to the separation, and both of the resulting phases can be continuous.

Upon complete solidification, two intimately interpenetrating phases exist. The resulting microstructure can be described as a three-dimensional interpenetrating composite. The "tendrils" of each phase have widths on the order of 1–3 μm and typically consist of about one grain of either Be or Al across each tendril.

Through recent advances in rapidly solidified powder processing techniques, fine-grained Be-Al composites have been produced at the Los Alamos National Laboratory (LANL) with a morphology indicative of liquid phase separation and with excellent strength and ductility. Initial studies concentrated on Be-28Al [56],

but a number of other compositions were examined during the development of these composites [57]. The composite studied in this research had a composition of Be-47.5Al-2.5Ag.

2.4 Neutron diffraction

Neutron diffraction was used in this study to quantitatively examine the deformation behavior of Be-Al composites. Neutron diffraction is an ideal technique because elastic strains can be measured for every crystallographic orientation in each phase. It is important to discuss the details of the experiment and describe exactly what information can be obtained and how to interpret it. This section will consist of a brief description of the theory of measuring strain using neutron diffraction. This will be followed by an analysis of how these measurements can be applied to studying deformation in composites. Finally, a brief overview of the application of neutron diffraction for examining deformation in composites will be presented.

2.4.1 Neutron diffraction strain measurements

Neutron diffraction for strain measurement is described in the literature [58–61]. Diffraction of neutrons is governed by Bragg's law,

$$\lambda = 2d_{hkl} \sin \theta_{hkl} \tag{2.11}$$

where λ is the neutron wavelength, d_{hkl} is the spacing of a crystal plane having indices hkl, and θ_{hkl} is the angle of incidence of the neutron beam on the hkl plane.

At the LANL Manuel Lujan Jr. Neutron Scattering Center (LANSCE), polychromatic pulses of neutrons are produced by spallation interactions of 800 MeV protons with a tungsten target. At a pulsed neutron source, an entire diffraction pattern can, in principle, be acquired from a single neutron pulse, although many pulses are usually needed to acquire adequate statistics. Each detector at a fixed angle records the entire diffraction pattern. Based on the "time of flight" of the diffracted neutrons, the d-spacing can be calculated for each crystal plane that is oriented correctly for diffraction. The wavelength of a neutron, from wave mechanics, can be expressed as

$$\lambda = \frac{h}{mv} = \frac{ht}{mL} \tag{2.12}$$

Here, h is Planck's constant, m is the mass of the neutron, v is the velocity of the neutron, and t is the time taken for a diffracted neutron to travel the total flight path L.

By combining Equations 2.11 and 2.12, the d-spacing can be expressed in terms of the time of flight as

$$d_{hkl} = \frac{ht}{2mL \sin \theta_{hkl}} \tag{2.13}$$

Elastic strains for individual lattice planes are calculated using

$$\varepsilon_{hkl} = \frac{\Delta d_{hkl}}{d_{hkl}} \tag{2.14}$$

where Δd_{hkl} is the change in d-spacing from two diffraction patterns taken at two different applied stresses.

A typical diffraction spectrum for a Be-Al composite is shown in Figure 2.14. The individual peaks are sharp, well defined, and well separated. The intensities are normalized by the incident spectrum and have had a background subtracted. Individual Be and Al Bragg peaks are labeled. The tick marks below the diffraction spectrum indicate predicted reflections for Be (lower marks) and Al (upper marks). The stronger scattering of the Be over the Al is apparent from the disparity in the peak intensities.

Figure 2.15 illustrates the shift in the Be $(10\bar{1}1)$ diffraction peak recorded at applied stresses of -5 and -307 MPa. Using Equation 2.14, $\varepsilon_{(10\bar{1}1)} = -8.2\times10^{-4}$.

The complete diffraction pattern is taken by a single detector and is, therefore, associated with this detector and, as a consequence, with a given diffraction angle. Each hkl peak in a diffraction pattern from a given detector represents diffraction from the subset of grains that have this particular hkl peak oriented correctly for diffraction. Therefore, each peak represents diffraction from a different subset of grains.

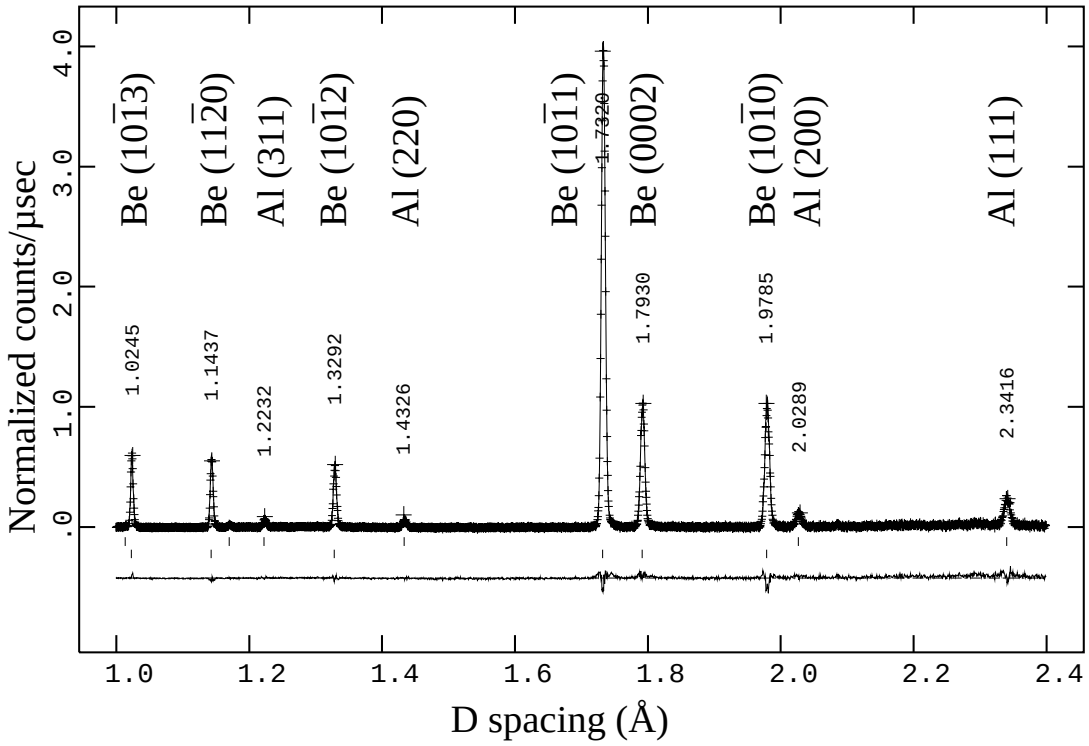

Figure 2.14: Diffraction spectrum for Be-47.5Al-2.5Ag. The fitted background response has been subtracted and the intensity has been normalized with respect to the incident spectrum.

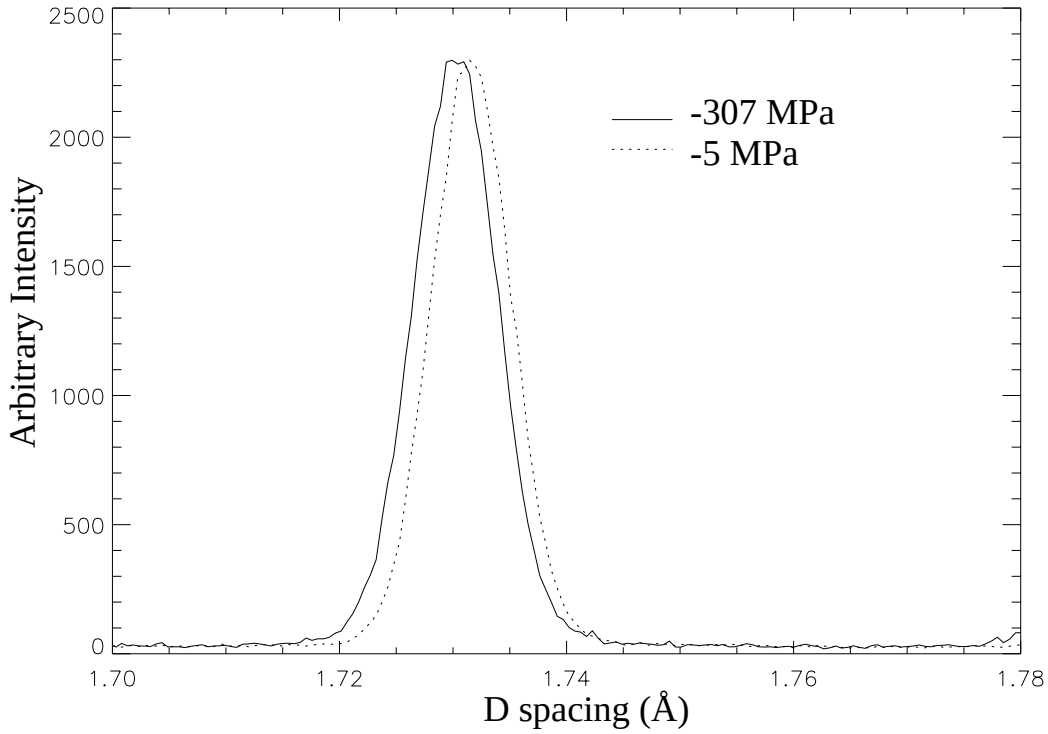

Figure 2.15: Effect of compression on the Be $(10\bar{1}1)$ diffraction peak, calculated elastic strain: -8.2×10^{-4}

2.4.2 Rietveld refinement

Strain data from individual sets of hkl planes can be analyzed to understand the response of every crystallographic plane in each phase during deformation of a two-phase system. Although this data is useful for a detailed understanding of the dependence of crystallographic orientation on deformation behavior in each phase, it is sometimes more useful to describe the stress-strain behavior on a phase average basis. For example, for comparison with finite element analyses, the stress-strain behavior of each phase is required, rather than the stress-strain behavior of each crystallographic plane within each phase.

One method of arriving at a phase average behavior is to calculate an average lattice parameter for each phase based on a Rietveld profile refinement of the complete diffraction spectrum [62]. In this approach, the intensities and positions of all Bragg peaks are predicted from an assumed crystal structure using the Los Alamos Generalized Structure Analysis System (GSAS) software [63]. The predicted spectrum is then optimized to match the measured spectrum. Using a least-squares fit between the observed and predicted spectra, the atomic positions and the lattice parameters can be calculated. The solid line through the data in Figure 2.14 is a Rietveld fit, and the line below the tick marks is the difference curve.

A lattice parameter determined in this manner is an empirical phase average. This can be used to calculate strain in each phase during a loading experiment. Strain is calculated by replacing values of interplanar spacings in Equation 2.14 with the values of the lattice parameters obtained using the Rietveld refinement (a for Al, a and c for Be).

The validity and usefulness of using these lattice parameters for comparison with continuum mechanics calculations has been demonstrated [58]. Rietveld refinements were made on neutron diffraction data taken during a tensile test of austenitic stainless steel up to a plastic strain of 2% [64]. The response of the calculated lattice parameter agreed with the expected average elastic response, even in the plastic region. This study demonstrated that the refinement is a good empirical average of the various *hkl* responses.

A more recent study considered the agreement between single peak fits and the Rietveld refinement-modeled single peak positions for Be under a compressive load [65]. It was found that the agreement was good in the elastic and early plastic regime.

Three methods are available in the Rietveld refinement process for handling crystal structures such as Be that exhibit anisotropic properties. The first method is to assume that the strains in the a and c directions are such that c/a remains constant. The second, or "normal" method, is to allow c/a to vary, and

$$\frac{1}{d_{hkl}^2} = \frac{4}{3}\left(\frac{h^2 + hk + k^2}{a^2}\right) + \frac{l^2}{c^2} \tag{2.15}$$

The third method is to include the elastic anisotropy of the single crystal (see Table 2.1) in the refinement. The three methods of refinement were compared for use with Be [65].

The normal method was used in this dissertation. This approach assumes that the crystal structure remains perfectly hexagonal and that all *hkil* planes have responses between that of the (0002) and $(10\bar{1}0)$ planes. Different strains are obtained in the a and c directions. It was found that if these strains were av-

eraged according to $(2\varepsilon_a + \varepsilon_c)/3$, this gave the same results as the first refinement method, where c/a was held constant [65].

Inclusion of the elastic anisotropy parameters in the refinement slightly improved the fits to individual peaks and, therefore, may be useful when this is the goal of the research, for example, in studies of texture. However, Daymond, Bourke, and Von Dreele [65] give a couple of reasons why normal Rietveld refinements may work for anisotropic materials such as Be. First, the majority of reflections collected by a given detector bank move in the same direction during a loading experiment. Second, elastic strains are small (generally less than 2×10^{-3}), and the deviations due to anisotropy would only be a modest percentage of this strain. It was concluded that the normal refinement method provided a good bulk average of the polycrystalline strains in Be.

2.4.3 Neutron diffraction strain measurements on composites

Deformation

Neutron diffraction is an ideal technique for studying the deformation of composites because it distinguishes between phases and measures strain in all possible crystallographic orientations. Unlike x-rays, which are typically limited to near-surface regions, neutrons provide a volumetric or bulk average strain. This is because the depth at which most of the diffracted beam originates is typically several orders of magnitude greater for neutrons than for x-rays. For most engineering materials, neutrons penetrate on the order of millimeters, compared

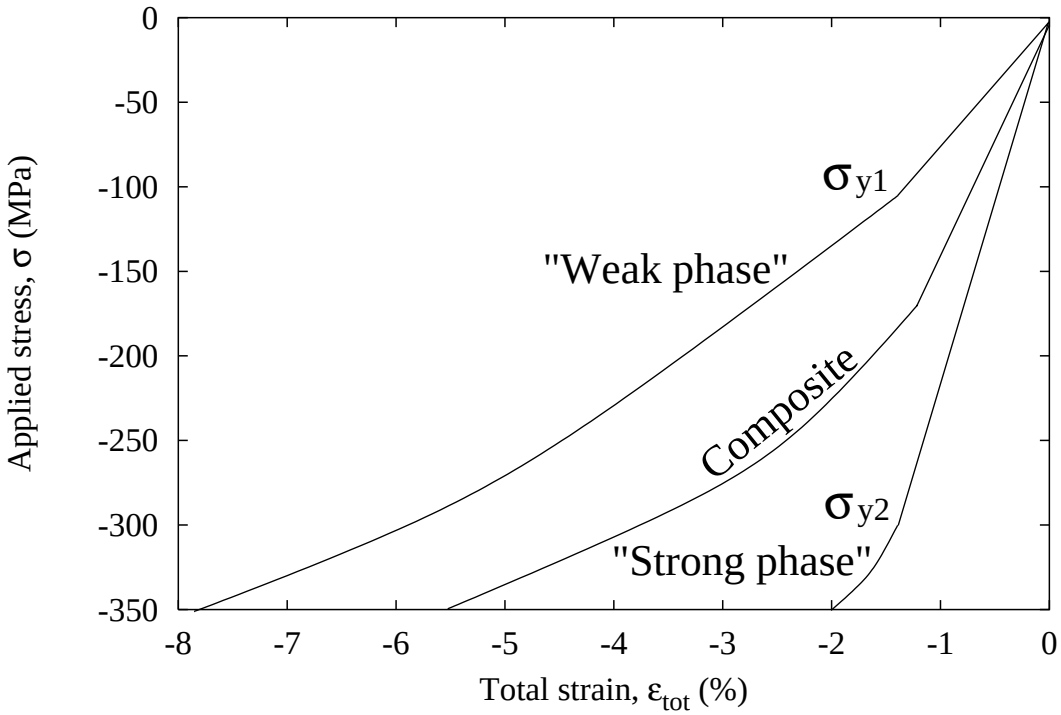

Figure 2.16: Hypothetical compression stress vs. strain data for a "weak phase," a "strong phase," and a composite (which consists of the two phases)

with microns for x-rays [66].

A neutron diffraction experiment on a hypothetical metal matrix composite will be described in order to understand the results from the present research. The metal matrix composite comprises two phases: one with a low yield stress (σ_{y1}) and low modulus, the other with a high yield stress (σ_{y2}) and high modulus. Hypothetical compression $\sigma - \varepsilon$ data for each phase and for the composite are shown in Figure 2.16.

Figure 2.17 shows the applied stress vs. elastic strain data expected from neutron diffraction measurements taken during a uniaxial compression test of this composite. Strain measured parallel to the compressive load is negative,

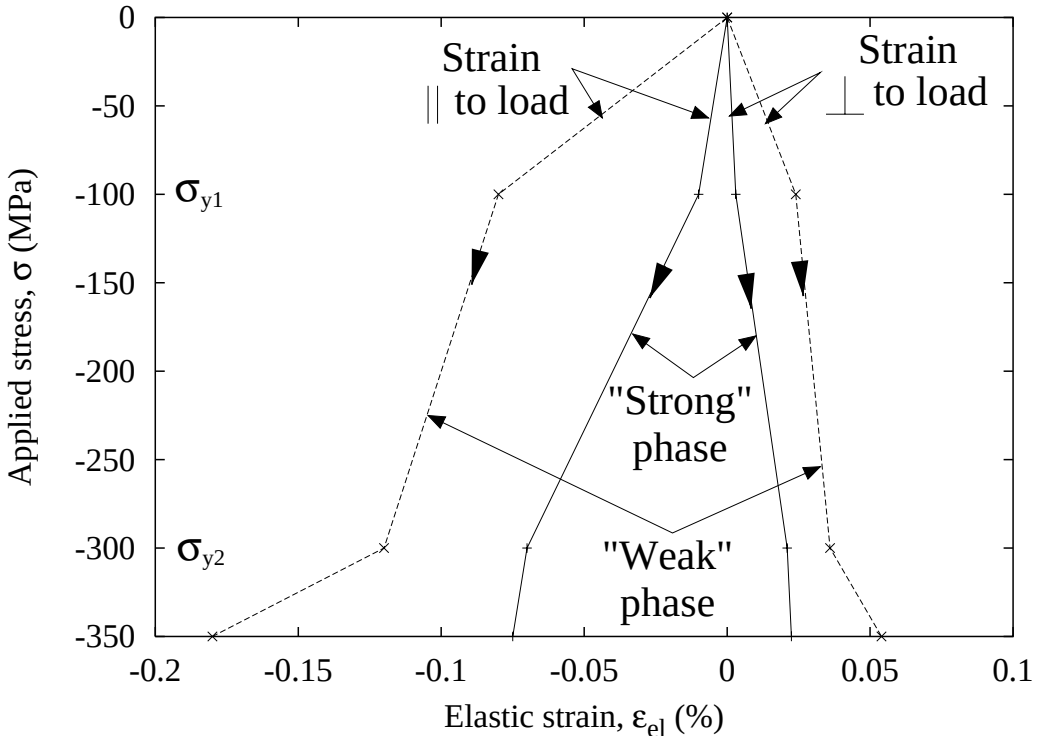

Figure 2.17: Applied stress vs. elastic strain data from a hypothetical neutron diffraction compression experiment on a composite, measured both parallel and perpendicular to the compression axis

and strain measured perpendicular to the load is positive. In this figure, the stress is the applied value (i.e., not the stresses within each phase).

Neutron diffraction measures only the elastic strain, not the total strain. However, from the elastic data, load partitioning between phases is observable, and inferences can be made about the effects of plasticity on the overall deformation. Both phases (Figure 2.17) are elastic up to σ_{y1}, when the weak phase begins to yield. Parallel to the loading direction, this causes the rate of elastic straining in the weak phase, $d\varepsilon_{el}/d\sigma$, to diminish because it accommodates less elastic strain and, thus, carries a smaller proportion of the load. Conversely, the

strong phase must accommodate more load and, therefore, its applied stress vs. elastic strain curve deflects in the opposite direction. Eventually, σ_{y2} is reached and the strong phase yields, resulting in another load repartition. At this point the curves deflect in the opposite directions. In this example, it is assumed that both phases continue to work harden beyond σ_{y2}. If one phase becomes perfectly plastic, its rate of elastic straining would be constant, $d\varepsilon_{el}/d\sigma = 0$.

Perpendicular to the load (Figure 2.17), the strains would be positive for a compression test, and the ratio with the strains parallel to the load is related to the Poisson's ratio (ν) for each phase. As before, the inflection points in the curves indicate repartitioning of the load due to yielding.

Previous studies

Neutron diffraction has previously been used to study thermally and mechanically induced strains in a number of composites [67–70]. Thermally induced residual strains were measured in a SiC whisker-reinforced Al_2O_3 composite [71–73]. It was found that the matrix was in a state of hydrostatic tension. The magnitude of residual strain decreased with increasing temperature and increased with increasing volume fraction of whiskers. Generally good agreement was found with predictions based on Eshelby's equivalent inclusion analysis.

Thermally and mechanically induced strains were measured in Al composites reinforced with either 15 vol% SiC whiskers or 20 vol% SiC particulates [74, 75]. Finite element analyses were performed using an axisymmetric unit cell model. Although the inclusion geometry affected the correlation between numerical and experimental results, it was shown that continuum-based models using finite

elements could be used effectively to calculate average residual strains for comparison with neutron diffraction results. An analysis using Eshelby's equivalent inclusion technique was also successfully used to interpret neutron diffraction measurements on Al reinforced with SiC whiskers or particulates [76].

The repartitioning of load described in the previous section was measured in an Al composite reinforced with 15 vol% TiC particulate using neutron diffraction during tensile loading [77–79]. The proportion of the applied load carried by each phase changed due to the evolution of matrix plasticity. Finite element calculations were performed using an axisymmetric unit cell model and showed good agreement with the neutron diffraction measurements.

2.5 Deformation of composites

Plastic deformation in metal matrix composites can be described by theories that are based on dislocation micromechanics or continuum mechanics. In general, dislocation micromechanics is appropriate for describing the behavior of a composite on a scale comparable to the slip plane spacing. Continuum mechanics approaches are based on classical theories of plasticity, which are not scale dependent; however, these models include terms that may indirectly depend on geometry. Two approaches based on continuum mechanics will be reviewed. The first approach can be described as effective medium approximations, some of which have their origins with Eshelby's models of the mechanics of inclusions. The second approach encompasses numerical techniques, such as finite element method (FEM) calculations, and is well suited for the incorporation of plastic

constraint into generalized plasticity models.

2.5.1 Effective medium approximations

Effective medium approximations are a class of solutions in which composite properties are described in terms of volumetric averages. These include very simple approaches, such as the Reuss and Voigt bounds on elastic moduli discussed earlier, or more elegant solutions, such as Eshelby's equivalent inclusion method. Other models, such as self-consistent theories, which can account for non-dilute concentrations of the second phase and non-linear materials, have their origins in Eshelby's model.

Consider the case of two phases with different elastic constants (E_r and E_m) where the reinforcement phase is in the form of aligned fibers and is well bonded to the matrix phase. If the model is simplified further and treated as a sandwich consisting of two well-bonded parallel plates, upper and lower bounds for the properties of this composite can be derived.

If a load is applied parallel to the fiber axis (or parallel to the plane of the plates in this simplified model), the two components of the composite must have the same strain in this direction. This is the isostrain case and yields the Voigt upper bound for elastic modulus, E_u (Equation 2.4). If a load is applied normal to the face of the plates, the two components of the composite must have the same stress in this direction. This is the isostress case and yields the Reuss lower bound for elastic modulus, E_l (Equation 2.5). Other moduli can be predicted with the sandwich model, such as the shear moduli (G) and the Poisson's ratio (ν_{ij}) in certain directions.

The Reuss bound is rather crude, but others are available, such as the semi-empirical Halpin and Tsai [80] model,

$$E_l = \frac{E_m(1 + \xi\eta f)}{(1 - \eta f)} \tag{2.16}$$

where

$$\eta = \frac{\left(\frac{E_r}{E_m} - 1\right)}{\left(\frac{E_r}{E_m} + \xi\right)}$$

In this equation, ξ is an adjustable parameter and is generally of the order of unity. A comparison is made of this model with the Reuss lower bound and the Eshelby model, which shows that the Halpin-Tsai model gives a very good approximation for a Ti-SiC fiber composite [81].

These models are most useful for long-fiber composites. The most widely used model for short-fiber composites is the shear lag model, which is an analytical description of load transfer from the matrix to the fiber through interfacial shear [82]. Modified models, which take into account normal stress transfer at the fiber ends, are useful for composites with particularly short fibers or smaller fiber-matrix stiffness ratios [83]. The shear lag model has been used to predict the onset of matrix plasticity at fiber ends by specifying a critical shear stress for the matrix [81].

A wide range of problems can be solved using Eshelby's equivalent inclusion method, derived for isolated ellipsoidal inclusions embedded in an infinite medium [84]. These solutions are rigorous only in the case of an infinite matrix, but can be extended to include multiple inclusions. A review of self-consistent models [85, 86], which account for local interactions, can be found in [87].

Bounds for the elastic moduli were derived for a mixture of two phases with arbitrary geometry [88]. These bounds were found to be relatively close at low volume fractions [89], and in some cases, one of the bounds is an exact result for spherical inclusions distributed in a particular way within a matrix.

In the classical theory of plasticity, yielding occurs when the deviatoric stresses exceed some critical value. The Von Mises yield criterion can be expressed for the yield stress in uniaxial deformation σ_Y in terms of the principal stresses σ_i as

$$\sigma_Y = \left\{ \frac{1}{2}[(\sigma_1 - \sigma_2)^2 + (\sigma_2 - \sigma_3)^2 + (\sigma_3 - \sigma_1)^2] \right\}^{\frac{1}{2}} \tag{2.17}$$

When this criterion is satisfied everywhere in the solid, global yielding will occur. The importance of this to the present discussion is that hydrostatic stress does not affect yielding.

When a hard second phase is added to the material, plastic flow is constrained in localized areas near the inclusions. This has the effect of reducing the difference in principal stresses (Equation 2.17) in the constrained areas of the composite. Mutual constraint between the two phases can lead to large hydrostatic stresses. This constraint can significantly contribute to the overall composite strengthening. Consider the problem of plane strain compression of a block of material that obeys Von Mises criterion. When the block begins to yield, frictional forces, due to the platten, constrain the outward flow of the block material. Therefore, the applied stress required to cause flow is higher than the yield stress of the block material because of this constraint.

Hill [90] and Drucker [91, 92] incorporated the concepts of constraint into plasticity models. For example, the limit flow stress of a material can be greatly

enhanced when a large amount of constraint between the two phases is introduced. This can be accomplished through a high volume fraction of particles or closely spaced platelets. A particulate reinforced composite was modeled as a two-dimensional uniform array of non-deformable hexagonal particles in a perfectly plastic matrix, illustrated in Figure 2.18 [91]. The hexagonal grains have a side length a and are surrounded by a contiguous matrix of thickness h. High levels of constraint are developed in the matrix region that lead to composite strengths that are much higher than the yield stress of the matrix. It was shown [91] that for $a/h > 3$, the average strength of the composite $\bar{\sigma}$ is related to the matrix flow stress $\sigma_\circ$ by

$$\bar{\sigma} = \frac{\sigma_\circ}{2}\left(1 + \frac{2a}{3h} + \frac{h}{a}\right) \tag{2.18}$$

For completeness, it was found that for a/h between 1 and 3,

$$\bar{\sigma} = \frac{\sigma_\circ}{3}\left(2 + \frac{a}{h}\right) \tag{2.19}$$

and for $a/h < 1$,

$$\bar{\sigma} = \sigma_\circ \tag{2.20}$$

The ratio of a/h is a function of the area fraction of hexagonal particles and must be adjusted to match the volume fraction in an actual composite.

An extension of this analysis was used to predict the yield strength of pearlitic steels from the yield strengths of spheroidized steels [93]. In this work, the prediction was quite successful, even though a continuum plasticity model may

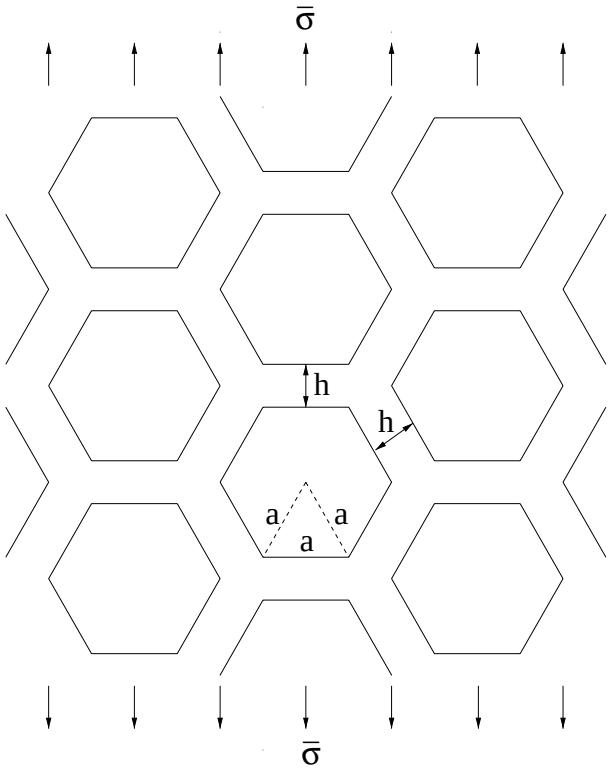

Figure 2.18: Drucker's model of a composite consisting of a two dimensional hexagonal array of hexagonally shaped non-deformable particles with sides of length a in a perfectly plastic matrix with a thickness of h (from [91])

have been inappropriate because of the fine scale of the microstructure.

2.5.2 Finite element methods

Finite element methods are well suited for solving plastic constraint and other problems related to deformation in metal matrix composites. Finite element calculations have become much more common because of the increased availability of the required computing power and improved software. A number of issues have been addressed in the literature. This section will focus on the effects of the reinforcement morphology, volume fraction, and distribution on the evolution of constraint and plastic flow of the composite.

The problems of interest here are metal matrices with either fibers, whiskers, or particles in which the reinforcement is generally considered to be rigid. Finite element models normally divide the composite into representative volume elements that model the behavior of the entire composite microstructure. For example, the simplest case consists of a unit cell incorporating one particle, whisker, or fiber surrounded by matrix material. The analysis consists of applying appropriate loading and boundary conditions to the unit cell and calculating the average behavior of the composite. As an example, a unit cell used for studying the effects of particle volume fraction and shape on the overall properties of the composite is shown in Figure 2.19 [94]. If the particle is axisymmetric, each hexagonal unit cell can be approximated by an axisymmetric cylindrical cell. In this study [94], it was found that spherical particles have little effect on the flow stress of the composite for volume fractions below 0.2, as suggested by Drucker [91]. Aligned needle-shaped particles with an aspect ratio of 10 are

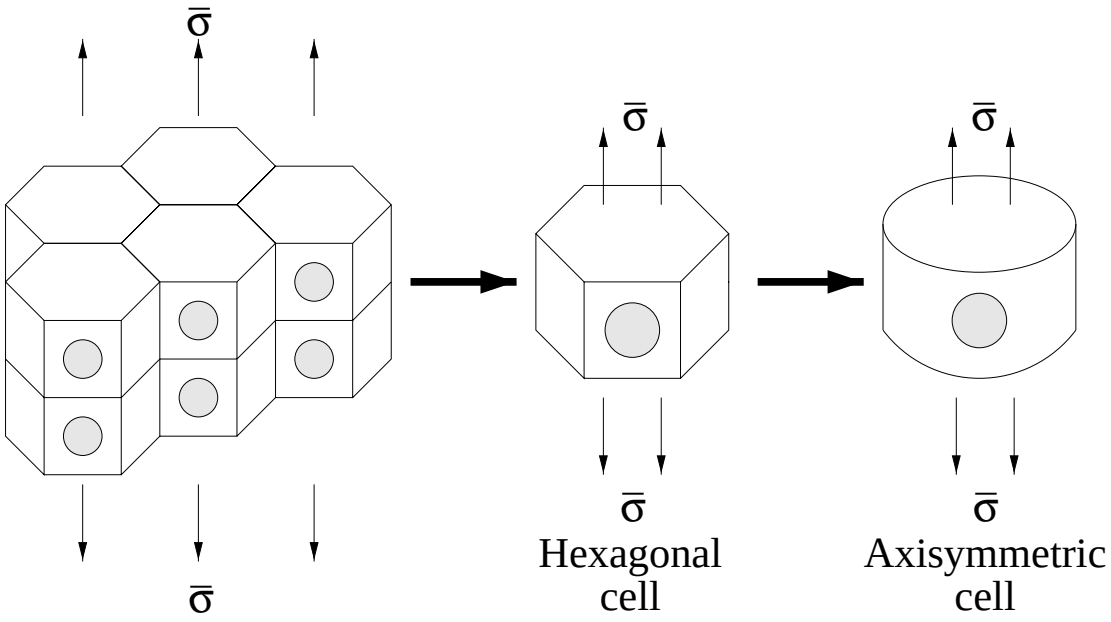

Figure 2.19: Axisymmetric unit cell representing a uniform distribution of particles (from [94])

more than ten times as effective as spheres at a volume fraction of 0.2.

Details of the reinforcement geometry and distribution, not only the aspect ratio, also strongly influence the evolution of constraint and hydrostatic stresses in the matrix and affect the overall constitutive behavior of the composite. A variety of unit cell models were studied to examine the effects of reinforcement geometry and distribution on the properties of Al-SiC particulate and whisker composites [89, 95]. If a whisker reinforcement is modeled as a cylinder with a flat surface, the hydrostatic stress level in the matrix is elevated in the vicinity of the sharp corner. It was found that the hydrostatic stresses were tensile in the matrix surrounding the end surfaces of the whisker, but compressive in the matrix material that was sandwiched between parallel whiskers. The development of these hydrostatic stresses provides an important contribution to strengthening,

which means the shape of the reinforcement used in the model is significant. For example, a cylinder with a flat surface was more effective at increasing the composite flow strength than a spherical reinforcement of the same size. It was also shown that clustering of these whiskers can have a significant effect on the development of triaxial stresses, and, in general, decrease the flow strength of the composite.

Finite element analyses have been used to solve many different problems related to continuous fiber-reinforced composites as well. Although the morphology of the present Be-Al composite is not that of a continuous fiber composite, many of the techniques used in the literature were used successfully in this study, especially those techniques that examined properties transverse to the fiber.

The influence of the cell geometry on the predicted behavior was studied for fiber-reinforced composites [96]. Two different finite element models were studied: one with a regular hexagonal array of fibers and one with a square array of fibers. It was found that the hexagonal array of fibers more closely represented the constitutive properties, especially the transverse properties, of a metal reinforced with a random array of fibers, when the matrix exhibited nonlinear behavior. Using this model, excellent agreement was found with experimental observations for various mechanical and thermal loadings of an aluminum alloy reinforced with alumina fibers [97–99]. This model will be utilized in the present work.

Finite element results were presented on the effects of fiber arrangement and fiber cross-section geometry on the constitutive behavior of metal matrix composites reinforced with continuous fibers [100]. An Al alloy reinforced with boron

fibers was chosen as a model system. It was found that these geometric variables had a strong effect on the behavior of the composite when the composite was loaded transverse to the fiber axis, but the effects were not as strong when the composite was loaded in axial tension. It was concluded that the major factor influencing the difference in transverse properties because of these variables was the manner in which local stresses evolved within the matrix. Different distributions and fiber geometries produced significantly different levels of hydrostatic stresses in localized regions of the matrix and lead to changes in the macroscopic flow stress and strain hardening rate.

2.6 Summary

A number of the issues and models described in this chapter influence the deformation of this Be-Al composite. The behavior of Be-Al will be described in terms of various composite deformation models, both analytical and numerical. Some of the issues that are important to the deformation behavior of the composite are the intrinsic properties of the phases, their scale, and morphology. The following chapter describes the experiments and results that address these issues.

Neutron diffraction is an excellent technique to quantify the intrinsic properties of each phase in a composite. Neutron diffraction measurements will demonstrate the evolution of hydrostatic stresses in the Al. This effectively raises the amount of hardening in the Al and allows it to bear a larger proportion of the applied load. This also raises the applied stress required to reach the critical fracture stress in the Be. The fine grain size of Be raises its critical stress for

fracture as well as its ductility. Simple finite element analyses will be used to reproduce the evolution of hydrostatic stress.

In Chapter 4, the results of the experiments and finite element calculations will be used to develop a model, or description, of deformation in this composite. The model explains the interaction between the phases and the local stress states established by compatibility requirements.

Chapter 3

Experimental Procedures and Results

3.1 Introduction

In this chapter, all of the experimental procedures performed during the study of a Be-Al composite will be presented, along with the results from these experiments. All of the research was performed at LANL. The material studied was a Be-Al composite with a composition Be-47.5Al-2.5Ag, previously fabricated at LANL. The processing method used to fabricate this material will be described. The microstructure will be shown using scanning electron microscopy (SEM). To further explore the morphology of the composite, an etching experiment was performed to examine the morphology of the Be phase after the Al was etched away.

The purpose of the present study was to consider the sequence of elastic and

plastic deformation in this composite and to characterize the deformation behavior of the individual phases. Details of the mechanical tests and *in situ* neutron diffraction loading experiments will be presented, along with their results, which quantify this deformation behavior.

3.2 Material processing

The material used in this study was produced by hot isostatically pressing powder which was made by centrifugal gas atomization[1]. This process involves induction melting a metal charge under argon in a graphite crucible and directing the molten metal through a nozzle onto the surface of a rapidly spinning disk. The liquid metal is mechanically atomized into finely divided droplets at the periphery of the spinning disk. The droplets are solidified in flight by heat transfer to a helium gas that also carries the powder particles into a cyclone separator. The powder is screened to a mesh size of -325, canned, and hot isostatically pressed to 100% density at 590 °C and 207 MPa.

The centrifugal atomization process produced spherical powder particles ranging in size from 5–200 μm in diameter with solidification rates on the order of 10^5–10^7 °C/sec. These solidification rates are rough estimates that were calculated based on many simplifying assumptions. The slowest solidification rate was calculated by assuming that the largest observed particle (200 μm) solidified with a change in temperature of 600 °C in the time it took to travel the entire diameter of the chamber at a constant speed, equal to the tangential velocity of

[1]The centrifugal gas atomization process for Be was developed at LANL under the National Aerospace Program and then under a Cooperative Research Agreement with Pratt & Whitney

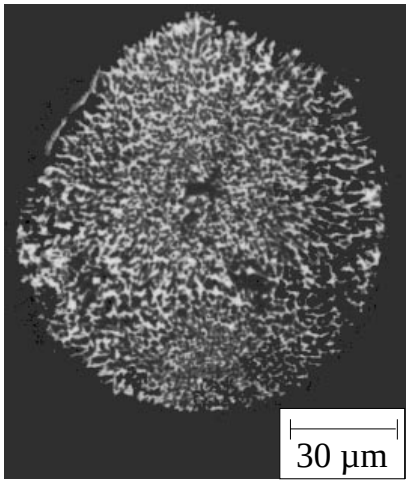

Figure 3.1: Powder particle of Be-Al produced by rapid solidification (backscattered SEM)

the disk. Particles larger than 200 μm did not solidify completely in this amount of time and adhered to the wall of the chamber.

The amount of heat generated during cooling and solidifying was calculated for each particle based on rule-of-mixtures values for heat capacity and heat of fusion. From this value, and the solidification time for the large particle, a heat transfer coefficient was calculated. By setting this coefficient equal to the heat transfer coefficient for the smallest observed particle (5 μm), the solidification time for the smallest particle was found. The fastest solidification rate (10^7 °C/sec) was then calculated, given a change in temperature of 600 °C.

The microstructure of a typical powder particle is shown in Figure 3.1, using backscattered SEM imaging, which enhances the contrast between the Be and Al. The rapid solidification results in two distinct, continuous phases in a three-dimensional interpenetrating morphology, indicative of liquid phase separation.

Minor additions of Ag were used to study the effects of age-hardening the Al

on the hardness and other properties of the composite [101]. An optimum combination of properties was obtained with a composition of Be-47.5Al-2.5Ag [101–105]. All of the material examined had this composition and was examined in the as-HIP'd condition, with the Ag in a super-saturated solid solution with the Al. The formation of the equilibrium phase $AgBe_2$ was suppressed by rapid solidification. The condition of the material was chosen to simplify the development of a model for deformation. All studies were performed on material in the as-HIP'd condition to avoid complexities in the analysis arising from texture due to rolling or extrusion. Also, the Ag was in solid solution in the Al; therefore, the analysis did not need to consider any effects due to precipitates in the material.

3.3 Microstructural characterization

Two commercially available Be-Al composites were examined during the course of this research: Beralcast 363 [2] and AlBeMet AM162 [3]. The neutron diffraction experiment results for the AlBeMet AM162 material will be presented here because this material had a microstructure very similar to the LANL Be-Al. These results showed the same characteristics as those from the LANL Be-Al.

Beralcast 363 has a nominal composition of 65Be-30Al-3Ag with other minor additions of silicon, germanium, or cobalt. The alloy was developed for structural applications and designed for improved castability, as well as good strength and ductility in the as-cast condition. Silver helps strengthen the Al by precipitation strengthening. Germanium improves castability by lowering the interfacial

[2]Sample provided by Starmet Corporation (formerly Nuclear Metals Inc.), Concord, MA 01742

[3]Sample provided by Brush Wellman Inc., Cleveland, OH 44110

energy between Be and Al and increasing the fluidity of the alloy. Due to the resulting decrease in porosity, Ge also improves the strength and ductility of the composite. Cobalt increases the hardness and strength of the Be phase.

The alloy is vacuum-induction melted in a ceramic crucible. The melt is homogenized and then poured into a preheated mold. The casting is solidified under vacuum to room temperature. The resulting microstructure is uniform, with very little texture. A typical microstructure is shown in Figure 3.2. In this backscattered SEM image, the Be is the dark phase and the Al is the light phase. Due to the slower solidification rate of casting versus atomization, no evidence of liquid phase separation is observed. The grain size is on the order of 25–50 μm, and consists of Be dendrites in an Al matrix. However, compared to many types of commercially available monolithic Be, the grain size is relatively small. Because of this, and the fact that the Be grains are surrounded by Al, this material still exhibits excellent strength and ductility.

AlBeMet AM162 is produced by a powder processing technique, similar to that used to produce Lockalloy in the 1970s. The powder is produced by inert-gas atomization, cold isostatically pressed to about 80% of its theoretical density, and then consolidated further by extrusion. AlBeMet is also produced as HIP'd block. A backscattered SEM image of the typical microstructure is shown in Figure 3.3. It is evident that the grain size, 5–10 μm, is much smaller than that of the cast product. The microstructure is similar to that of the LANL Be-Al composite.

The focus of the present research is on the composite fabricated at LANL with a composition Be-47.5Al-2.5Ag. Results from neutron diffraction experiments on

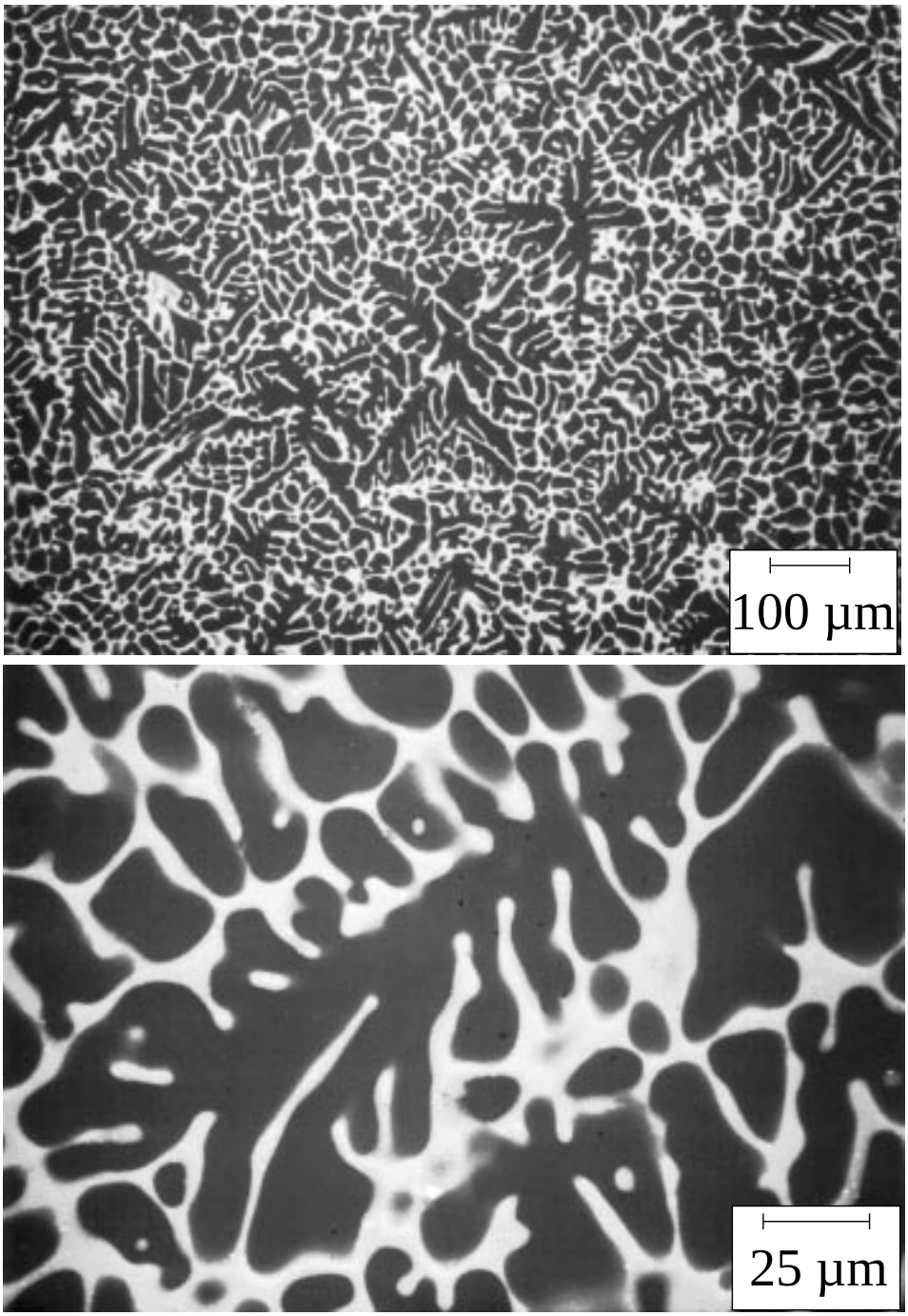

Figure 3.2: Microstructure of Beralcast 363 (backscattered SEM)

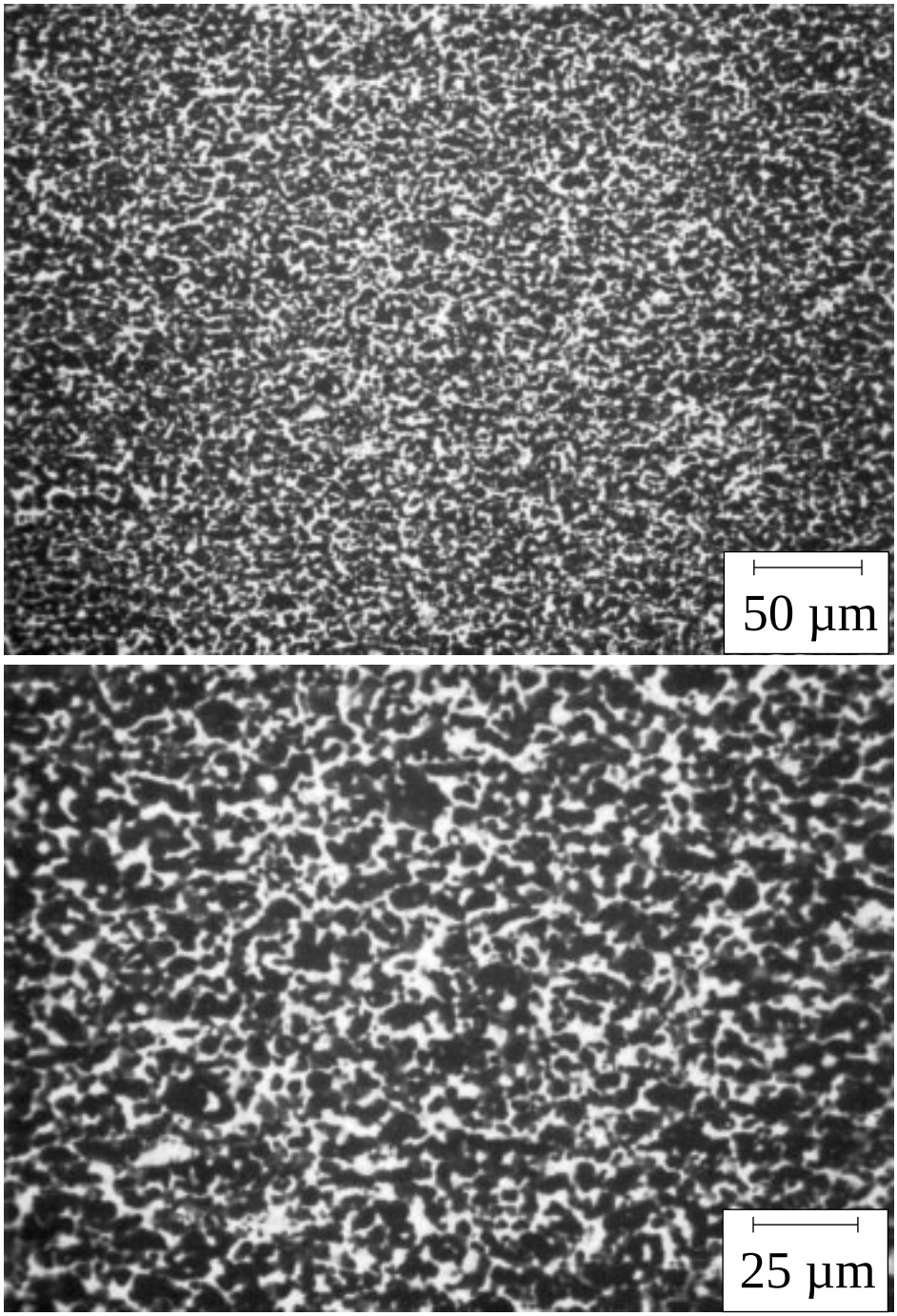

Figure 3.3: Microstructure of AlBeMet AM162 (backscattered SEM)

the commercial alloy will be presented solely for the purpose of supporting certain observations made regarding the LANL composite.

One of the unique features of this composite is its morphology and microstructure, produced by liquid phase separation. It can be described as a three-dimensional interpenetrating composite in which each phase is continuous. A number of studies were performed to characterize this microstructure. A backscattered SEM micrograph is shown in Figure 3.4. As shown in this micrograph, this composite had a very fine microstructure, with a grain size on the order of 1–3 μm and about one grain across each "tendril" of Be or Al.

3.4 Etching experiments

One method used to evaluate the morphology of the composite was to etch away the Al phase with sodium hydroxide and closely examine the remaining material. Two samples of as-HIP'd Be-47.5Al-2.5Ag, labeled as Sample 1 and 2, were immersed in a solution of 10% NaOH at 80 °C. The sample geometry was the same as that used for tensile tests (see Figure 3.8). Immersion density measurements were taken before and after the experiments [106]. The samples were weighed periodically during the experiments. Microscopy was performed on the samples after the experiments were complete.

Table 3.1 shows the density of the samples before and after the experiment. The theoretical density of Be-47.5Al-2.5Ag is 2.23 g/cm^3, and the theoretical density of Be is 1.848 g/cm^3. The density after etching should not be less than that of pure Be; therefore, this error is due to the large amount of porosity in the

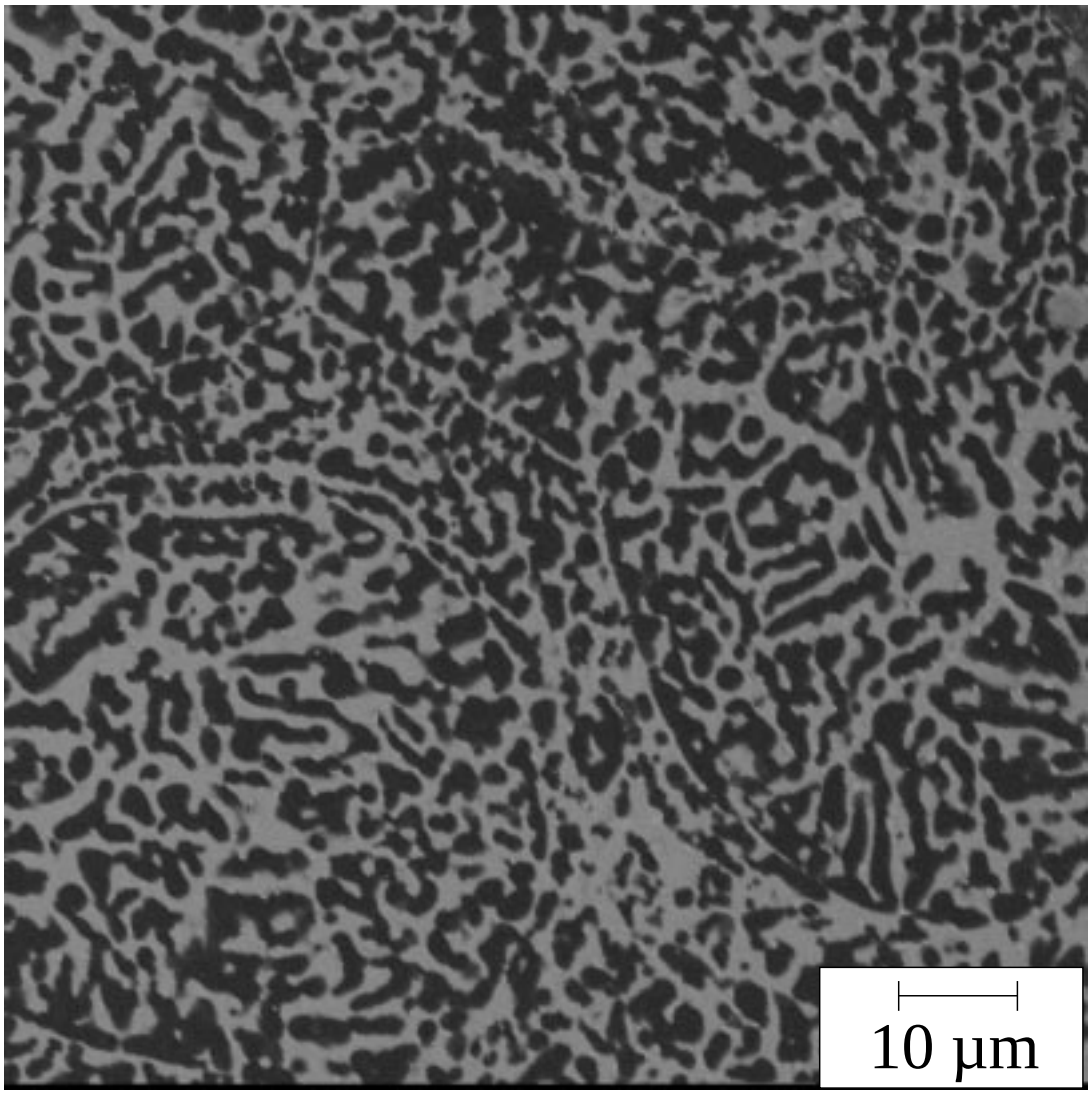

Figure 3.4: Microstructure of Be-47.5Al-2.5Ag (backscattered SEM)

Table 3.1: Density before and after etching experiment

	Starting Density (g/cm^3)	Final Density (g/cm^3)
Sample 1	2.217	1.229
Sample 2	2.217	1.274

sample after etching and the small sample size, which makes an accurate density measurement difficult.

Figure 3.5 shows a plot of weight loss vs. time during the etching experiment. This plot is shown in order to emphasize the significance of optimizing the etching time and to document the amount of time necessary to etch away the Al phase. It is evident that Sample 1 lost more weight than the starting weight percentage of Al. The Be began etching away once the Al was gone, especially at the point on the graph where the rate of weight loss slows down considerably, at about 50% of the weight. Sample 2 was removed from the etchant when it had attained a weight loss of 46%, in order to etch away most of the Al and to prevent etching the Be phase.

The microstructures of the material remaining after the etching experiments from Samples 1 and 2 are shown in Figures 3.6 and 3.7, respectively. The microstructure of Sample 1 is unusual, but probably not indicative of the morphology of the Be in the as-HIP'd composite because a substantial amount of the Be was etched away. The microstructure consists almost entirely of platelets, similar to a graphite microstructure, and indicates that perhaps the Be grains preferentially etched a particular crystallographic plane.

Sample 2 is more indicative of the microstructure of the Be in the as-HIP'd

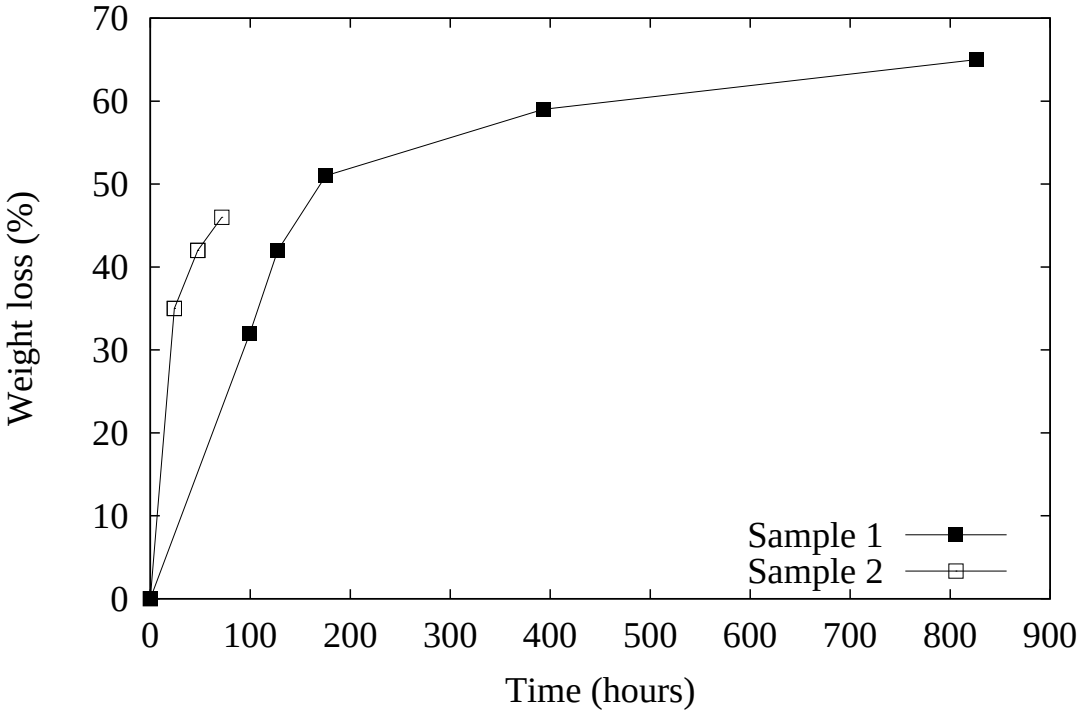

Figure 3.5: Weight loss vs. time during etching experiment

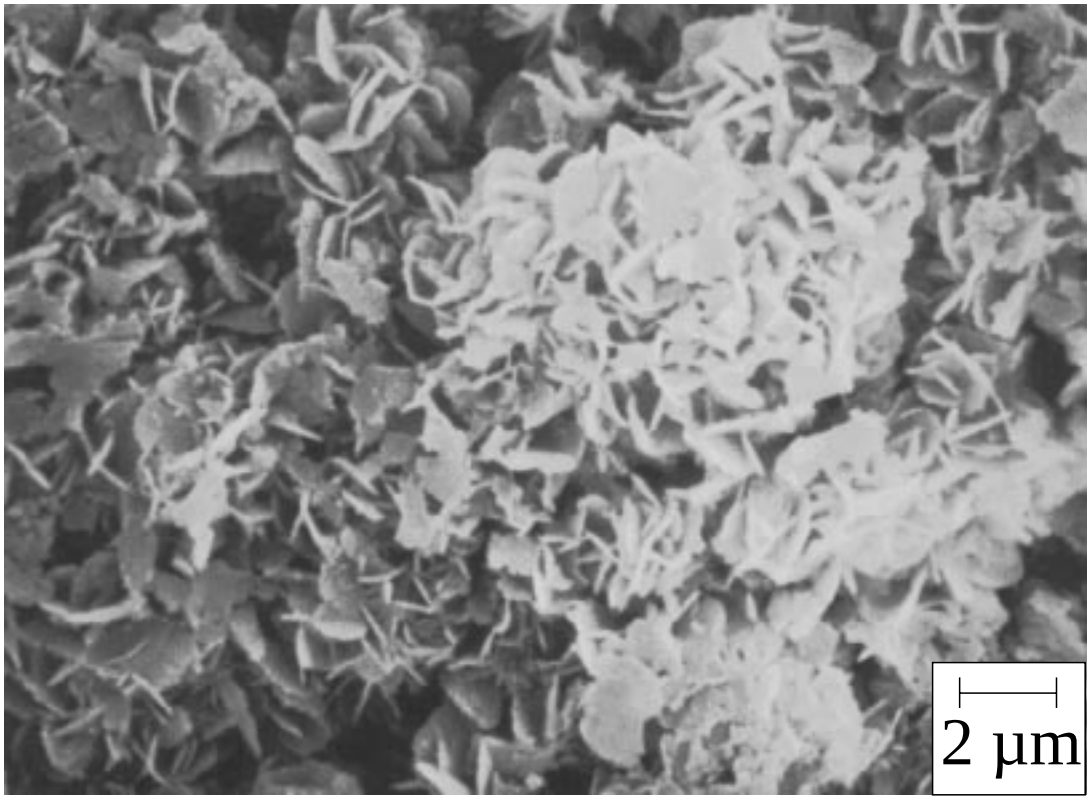

Figure 3.6: Microstructure of Sample 1 after etching for 826 hours

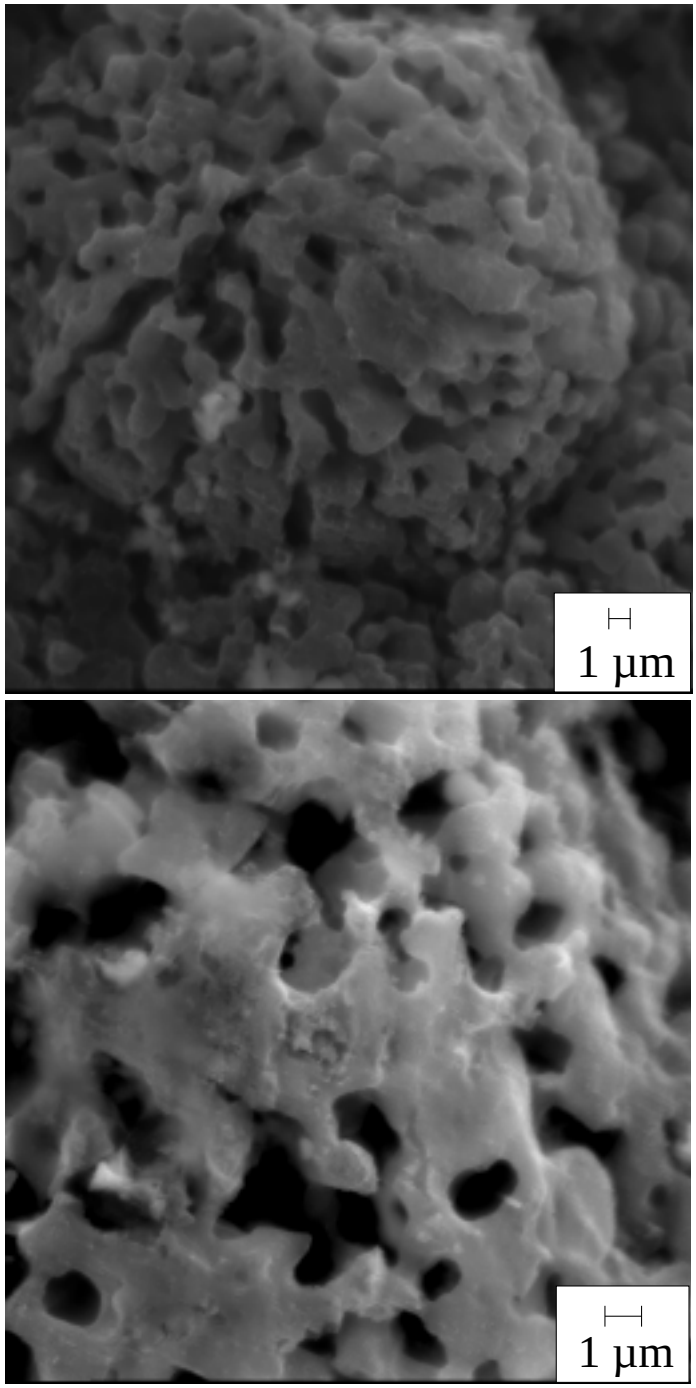

Figure 3.7: Microstructure of Sample 2 after etching for 72 hours

composite. Each powder particle is a completely interconnected network of Be, intertwined with a completely interconnected Al phase, now etched away. This is indicative of a microstructure created by liquid phase separation. The surface of the sample shows evidence of the boundaries of the original powder particles. Although both samples (even Sample 1) were still intact after the experiment, it appears that some of the powder particles were removed from the surface during the experiment. Some evidence of prior powder particle boundaries was also observed in as-HIP'd samples (see Figure 3.4).

3.5 Mechanical properties

The tensile properties of Be and Be-47.5Al-2.5Ag were measured using round tensile specimens, shown in Figure 3.8. This geometry is commonly used for tensile testing of Be and Be-Al composites. Representative tensile stress-strain curves for Be and Be-47.5Al-2.5Ag in the as-HIP'd condition are shown in Figure 3.9. The Be used in this test was fabricated using the same centrifugal gas atomization process as the one used for producing the composite. An optical micrograph, using polarized light, of its microstructure is shown in Figure 3.10. Even though the grain size was relatively small, 10–30 μm, the tensile elongation was only 1%.

The tensile elongation of Be-47.5Al-2.5Ag in the as-HIP'd condition is 8% with a yield strength of 300 MPa and an ultimate strength of 360 MPa. The Vickers Hardness is 140 VHN. Previous studies showed that these properties can be improved through further heat treatments or rolling. Table 3.2 [103, 104]

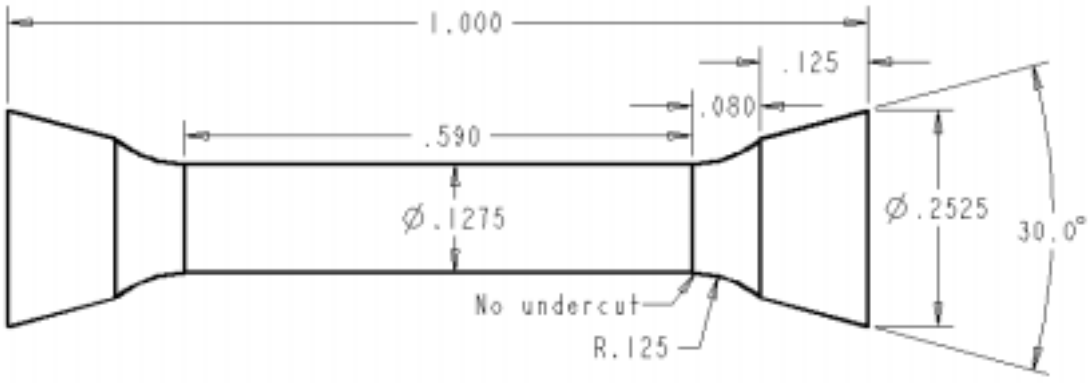

Figure 3.8: Round tensile test specimen geometry (in inches)

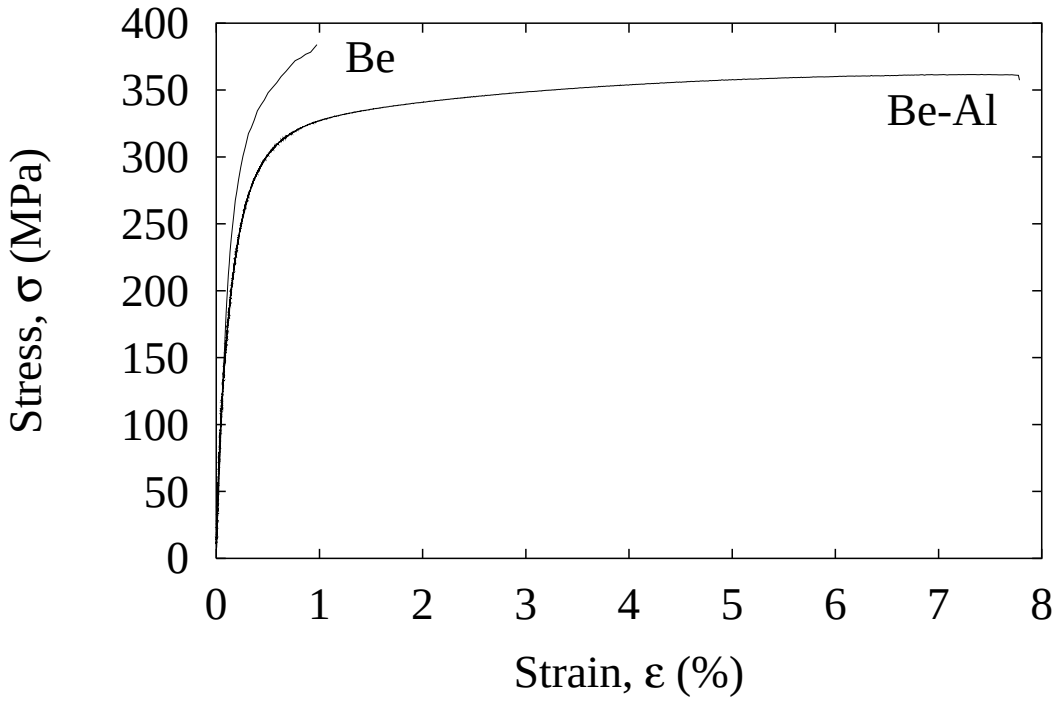

Figure 3.9: Tensile stress-strain curves for Be and Be-47.5Al-2.5Ag

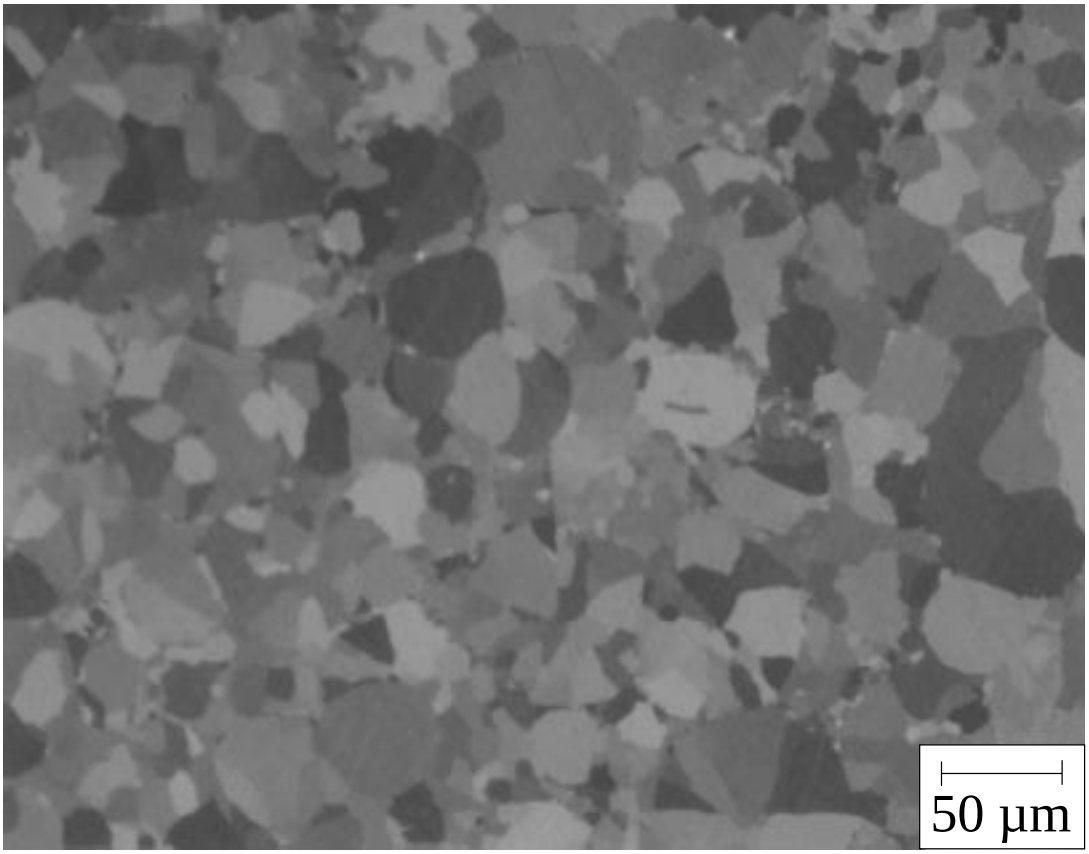

Figure 3.10: Microstructure of rapidly solidified HIP'd Be (optical)

Table 3.2: Tensile properties of rolled Be-47.5Al-2.5Ag sheet (from [103, 104])

Condition	σ_y (MPa)	σ_c (MPa)	Elongation (%)
Solution treated	356	427	6.6
Solution treated	358	430	9.6
Annealed	356	393	4.8
Annealed	354	399	6.3
175 °C age	400	455	10.6
175 °C age	399	458	9.1

shows the yield strength (σ_y), fracture strength (σ_c), and elongation for sheet that was rolled from material with three different heat treatments: *(i)* solution treated at 550 °C for 1 hour and then quenched; *(ii)* annealed at 550 °C for 1 hour and then furnace cooled; and *(iii)* solution treated at 550 °C, quenched, then aged at 175 °C for 16 hours.

To understand the deformation behavior, various fracture surfaces were closely examined. A secondary SEM micrograph of the fracture surface of a tensile specimen in the as-HIP'd condition is shown in Figure 3.11. The sample underwent a strain of 8% before failure.

It is not evident from Figure 3.11 that any substantial difference in the fracture morphology between the Be and the Al exists. In particular, the Al grains did not neck down to a point or debond from the Be during deformation. It appears that the Al was constrained by the Be. A hydrostatic stress is developed in the Al due to this constraint; it will be shown in the following chapter how this could enhance the flow strength and ductility of the composite. Also, there was no evidence of any microcracking in the Be, either at the fracture surface or away from the fracture surface.

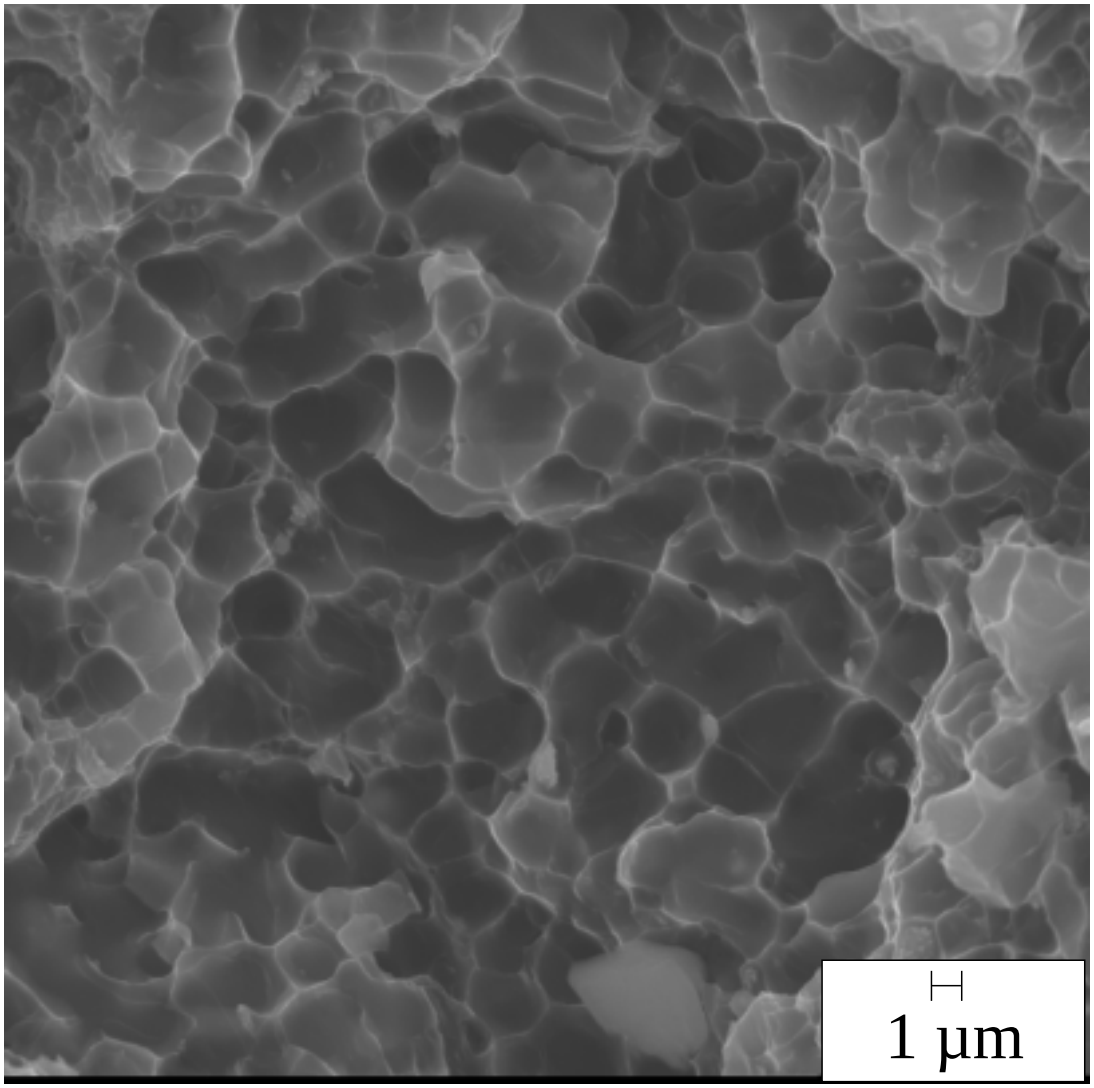

Figure 3.11: Fracture surface of a Be-47.5Al-2.5Ag tensile specimen (secondary SEM)

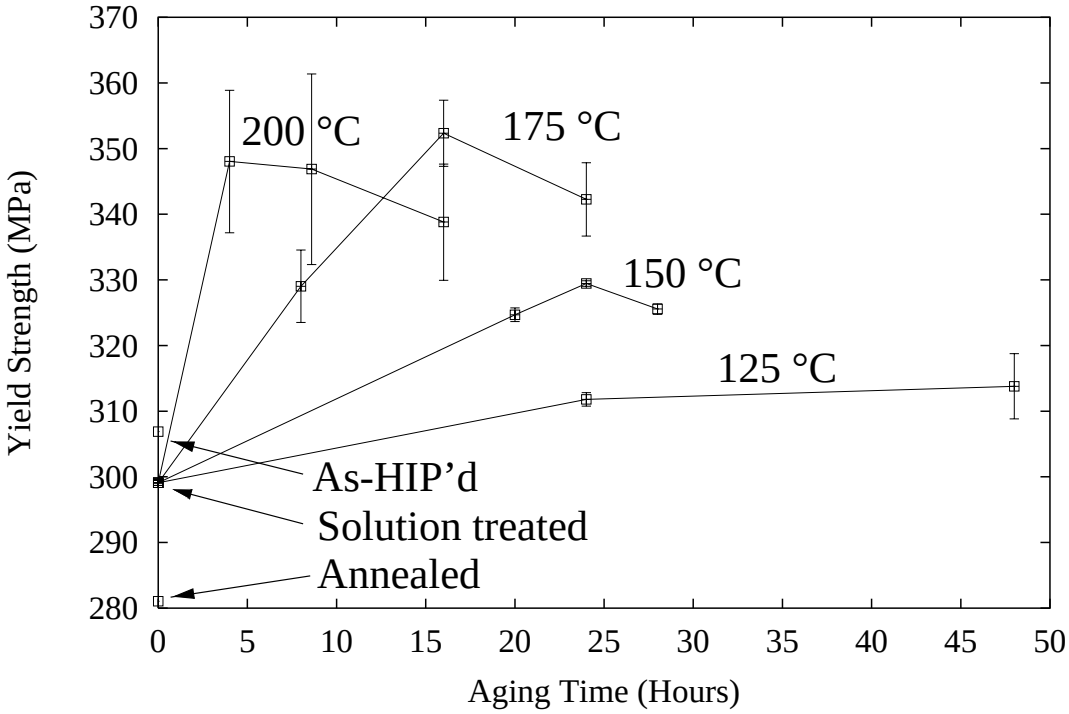

Figure 3.12: Effect of aging time and temperature on compression strength of Be-47.5Al-2.5Ag (from [103, 104])

The yield strength in compression for as-HIP'd material is 307 MPa. The compressive properties have also been measured as a function of aging condition [103,104]. The results are shown in Figure 3.12. This is a plot of compression strength versus aging time and temperature, showing that the higher temperature aging for shorter times produced the best results. Also shown on this plot are yield strengths for samples that were *(i)* as-HIP'd, *(ii)* solution treated at 550 °C for one hour and then quenched, and *(iii)* annealed at 550 °C for one hour and then furnace cooled.

In order to determine the yield behavior of the composite in bending, four-point bend tests were performed on the material in the as-HIP'd condition at two

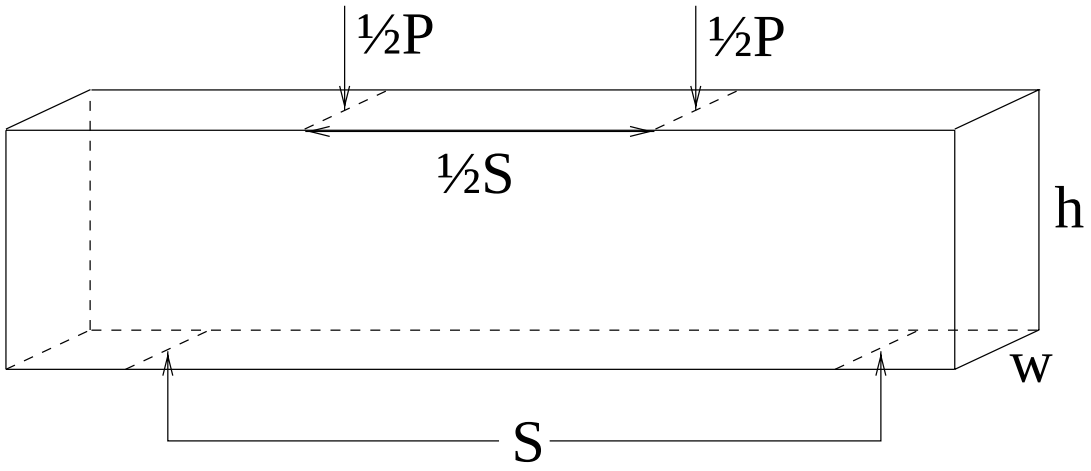

Figure 3.13: Four-point bend test specimen geometry

different strain rates. The maximum stress for a beam in bending is calculated using

$$\sigma = \frac{Mc}{I} \tag{3.1}$$

where M is the moment arm, c is the height of the neutral axis, and I is the moment of inertia.

The sample geometry and loading configuration is shown in Figure 3.13. For this sample geometry,

$$\sigma = \frac{3PS}{4wh^2} \tag{3.2}$$

where P is the applied load, S is the outer span, w is the sample width, and h is the sample height. For this experiment, $w = 2.5$ mm, $h = 6.4$ mm, and $S = 19$ mm.

Samples were tested in displacement control, at crosshead speeds of 0.127 and 1.27 mm/min. The stress versus crosshead displacement curves for samples tested at these two crosshead speeds are shown in Figure 3.14. Both samples

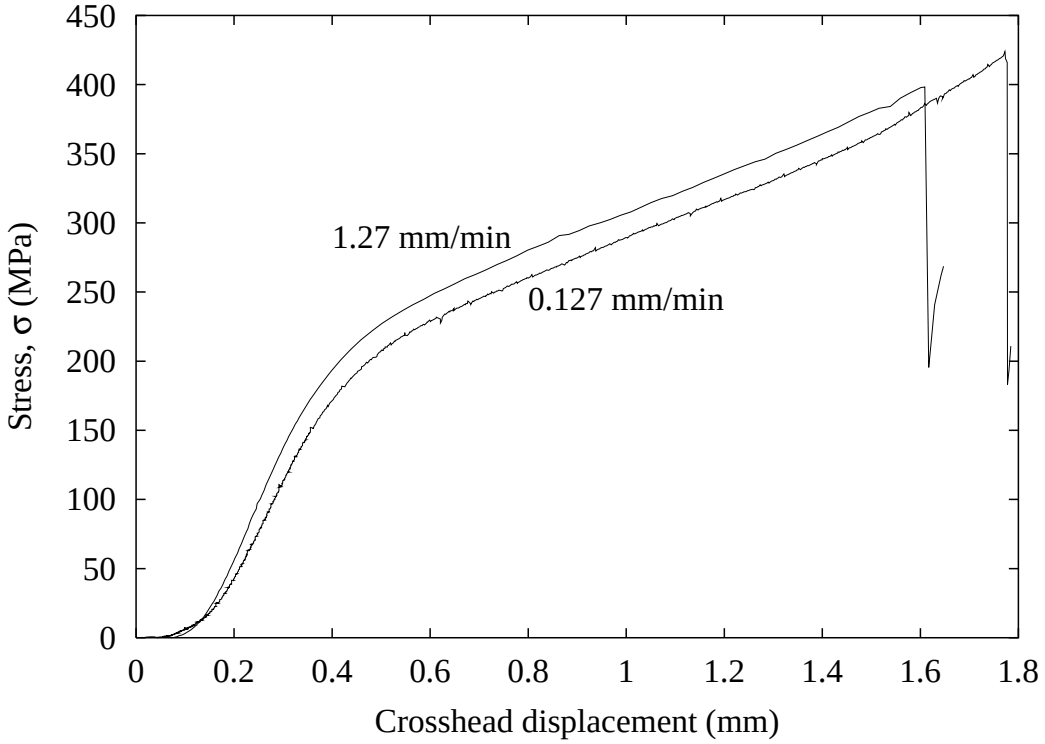

Figure 3.14: Four-point bend test data for Be-47.5Al-2.5Ag, crosshead speeds of 0.127 mm/min and 1.27 mm/min

bottomed out in the fixture prior to failure, demonstrating excellent ductility. Both samples yielded at approximately 200 MPa.

3.6 Cyclic tensile test

The focus of this research was dependent on whether the apparent ductility in Be-Al composites was due to microcracking or compatible plastic deformation; therefore, this question was addressed initially. Preliminary microscopic examinations suggest that the Be phase undergoes plastic deformation, rather than substantial microcracking during tensile elongation.

One of the first experiments performed was a tensile loading/unloading test, wherein the Be-47.5Al-2.5Ag composite was strained beyond yield, unloaded, and then reloaded. The purpose of the experiment was to determine whether the modulus of the composite remained invariant, an indication that minimal microcracking accompanies plastic straining. That is, whether all of the strain was caused by compatible plastic deformation of both the Al and Be phases.

The specimen geometry is shown in Figure 3.8. This test was performed on an MTS hydraulic load frame with a TestStar digital controller and software for control and data acquisition. A cyclic loading program was written such that each cycle would strain the sample to an additional 0.5% engineering strain (except the first five, which were in increments of 0.2%). Loading occurred in strain control, with a strain rate of 1×10^{-4} sec^{-1}. Unloading was performed in load control, and each unload went to a nominal load of 5 MPa. The sample was cycled in this manner until the specimen failed.

Figure 3.15 shows the resulting stress-strain curve. The modulus of the composite remained invariant, an indication that minimal microcracking accompanies plastic straining. That is, all of the strain is caused by compatible plastic deformation of both the Al and Be phases. One other noteworthy feature of this σ–ε curve was the ductile characteristic of the failure.

3.7 Thermal residual strain measurements

Three types of experiments were performed using neutron diffraction. The first experiment was designed to obtain diffraction patterns on powder samples to

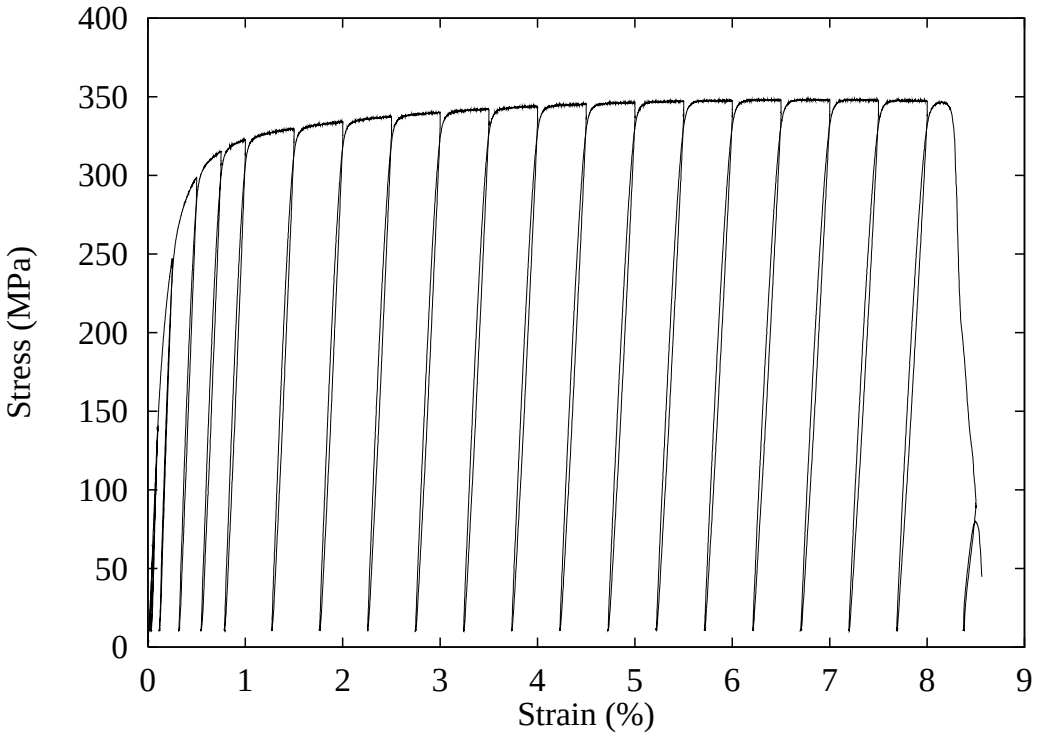

Figure 3.15: Cyclic loading experiment results for Be-47.5Al-2.5Ag

measure thermal residual strain due to processing. The second and third experiments were *in situ* loading experiments in which diffraction patterns were acquired from a sample held under either compressive or tensile load.

During processing, residual stresses result from the difference in thermal expansion coefficients between Be (11.6×10^{-6} K^{-1}) and Al (23.6×10^{-6} K^{-1}). After cooling from the pressing temperature (590 °C), the Be phase will initially be in compression and the Al in tension, though the magnitudes depend on the specific microstructure and creep characteristics of the phases.

The Be-Al composites were expected to begin the load tests with a pre-existing residual strain. To assess this, a neutron diffraction spectrum was acquired from two different powders. The first powder was the starting Be-47.5Al-2.5Ag powder from which the LANL Be-Al samples were fabricated. The second powder was nominally pure Be, also produced by centrifugal gas atomization, with a particle size of 5 μm. Each powder was sealed in a cylindrical vanadium can. Vanadium has a very short coherent scattering length; essentially no visible diffraction peaks were produced by the can.

Diffraction spectra were acquired on both powders and compared to a diffraction spectrum from the HIP'd cylindrical compression sample of Be-47.5Al-2.5Ag to obtain the level of residual strains due to HIPping.

Table 3.3 shows the residual strains in the HIP'd Be-47.5Al-2.5Ag sample with respect to both the starting powder and nominally pure Be powder. Be is in compression and Al is in tension with respect to the starting Be-47.5Al-2.5Ag powder. Also, the Be in the sample is in compression with respect to the Be powder. Surprisingly, the difference between the lattice parameter of Be

Table 3.3: Thermal residual strains, ε_T, in Be-47.5Al-2.5Ag

Phase (in HIP'd sample)	ε_T in $a_\circ$	ε_T in $c_\circ$	Basis for ε_T
Be	-1.62×10^{-4}	-2.76×10^{-4}	Be powder
Be	-1.53×10^{-4}	-3.54×10^{-4}	Be-47.5Al-2.5Ag powder
Al	$+3.26 \times 10^{-4}$		Be-47.5Al-2.5Ag powder

in the Be-47.5Al-2.5Ag powder and in the Be powder is slight, indicating that the residual strain in the starting Be-47.5Al-2.5Ag powder is similar to the Be powder.

3.8 *In situ* neutron diffraction loading experiments

3.8.1 Procedure

Neutron diffraction spectra were acquired on tensile and compression specimens of Be-47.5Al-2.5Ag while the samples were held under load. Cylindrical compression samples were machined with a diameter of 8 mm and a height of 24 mm. The tensile specimen geometry is shown in Figure 3.16. Experiments were performed in the stress rig shown schematically in Figure 3.17 [78]. This apparatus fit into a 0.74 m diameter cylindrical chamber in the neutron beam.

The orientation of the sample in the neutron beam is shown in Figure 3.18. By placing the loading axis at 45° to the incident beam, strains parallel and perpendicular to the loading axis were measured simultaneously by detectors at scattering angles of −90° (**Q** parallel to the load) and +90° (**Q** perpendicular to

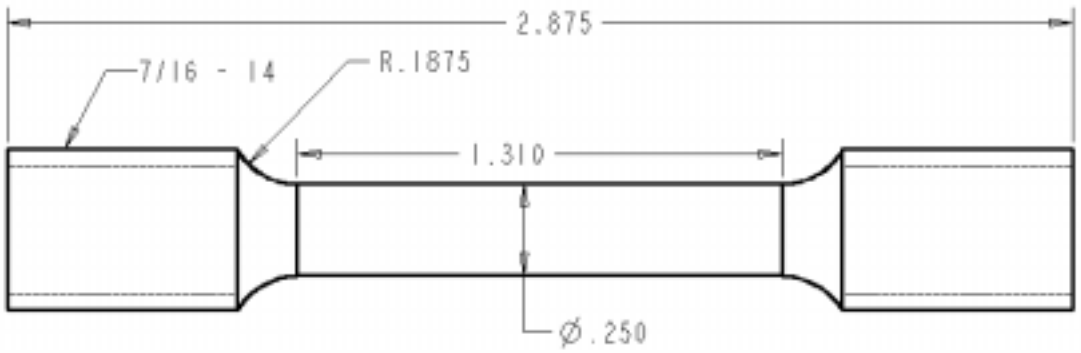

Figure 3.16: Round tensile test specimen geometry (in inches)

the load) where **Q** indicates the diffraction direction. Not shown in Figure 3.18 is an additional detector at +148° with respect to the incident beam.

Nominal loads of −5 MPa for the compression test and 5 MPa for the tensile test were used as the stress-free references. Each sample was loaded at a strain rate of 2×10^{-4} sec^{-1} in increments varying between 10 and 50 MPa. The sample was held in displacement control for 2–4 hours at each applied stress while diffraction data were acquired. Beryllium has a large neutron scattering cross-section and substantially shorter times could have been used for Be alone. By contrast, Al has a relatively small scattering cross-section; therefore, obtaining adequate statistical accuracy for the aluminum was the limiting factor in determining the hold duration at each stress.

The loading history for the compression experiment is shown in Figure 3.19. The maximum applied stress was −323 MPa. The total strain was measured using an extensometer. At higher loads, some stress relaxation was noted, but the change was only 10 MPa even at the highest applied load.

The compression experiment was repeated using a sample of AlBeMet AM162 to determine whether the behavior was repeatable with another Be-Al composite.

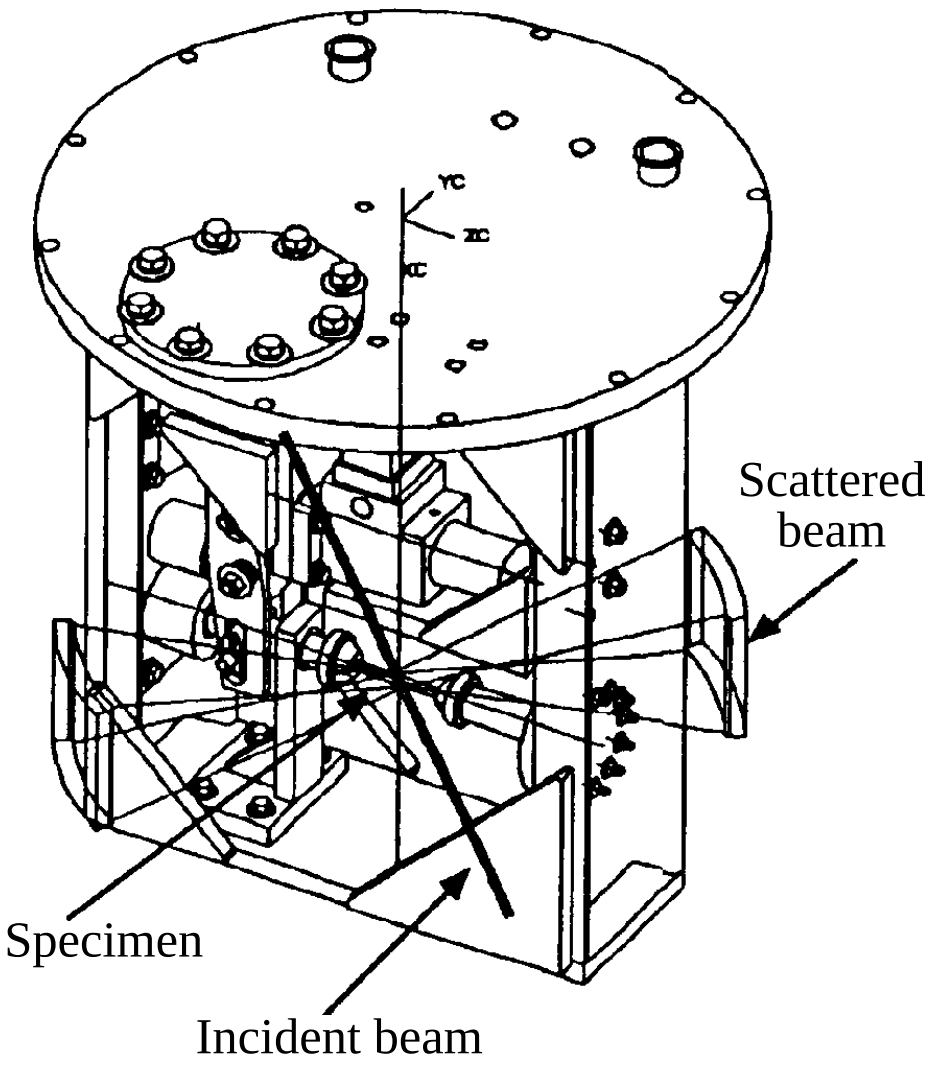

Figure 3.17: Stress rig used for loading experiments in the neutron beam (from [78])

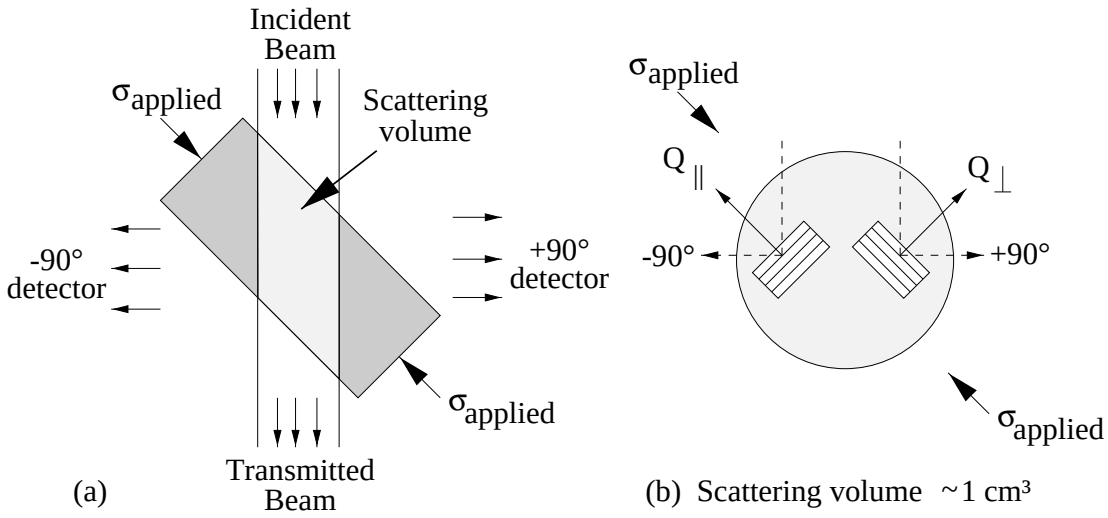

Figure 3.18: Scattering geometry: (a) axial and transverse strains are measured simultaneously in $-90°$ and $+90°$ detector banks, respectively; (b) dashed lines show the paths of the incident and diffracted beams, which record strain parallel ($\mathbf{Q}_{\parallel}$) and perpendicular ($\mathbf{Q}_{\perp}$) to the applied load

The loading history for the AlBeMet sample was similar to that for the LANL Be-Al, except that the maximum applied stress was -302 MPa. The total strain was measured using the average of two strain gauges on diametrical sides of the samples. These strain measurements did not deviate significantly, which indicates good alignment of the loading axis.

Since the AlBeMet sample had been extruded, some texture was expected. This texture is apparent in the difference in diffraction spectra recorded by detectors parallel [Figure 3.20(a)] and perpendicular [Figure 3.20(b)] to the extrusion direction. The extrusion caused the Be basal (0002) planes to align parallel to the extrusion direction. Therefore, the relative intensity of the (0002) diffraction peak recorded parallel to the extrusion direction is much higher than the (0002) diffraction peak recorded perpendicular to the extrusion direction.

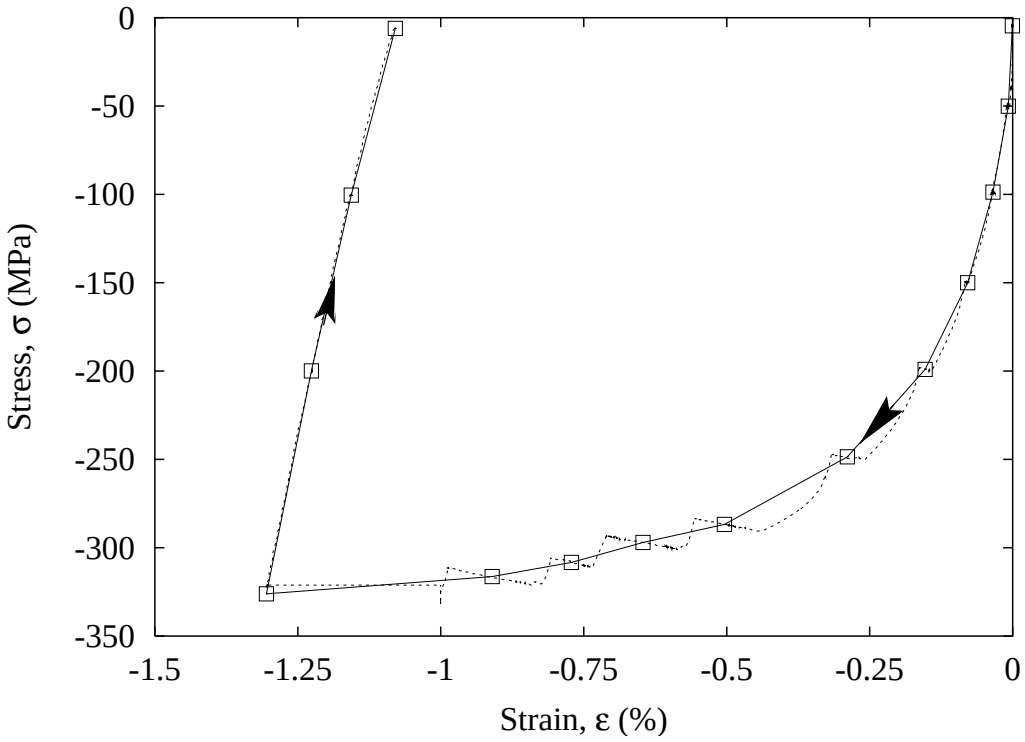

Figure 3.19: Applied stress vs. total strain

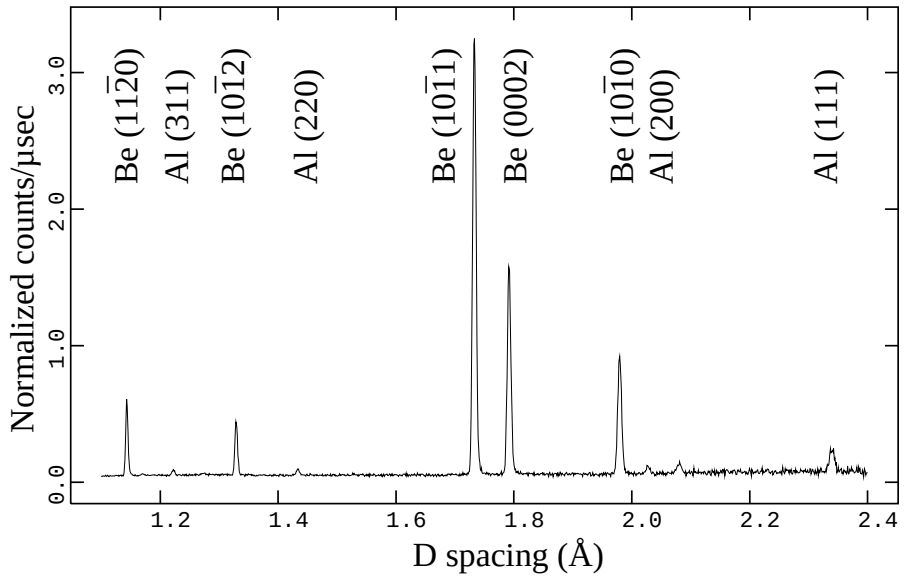

(a)

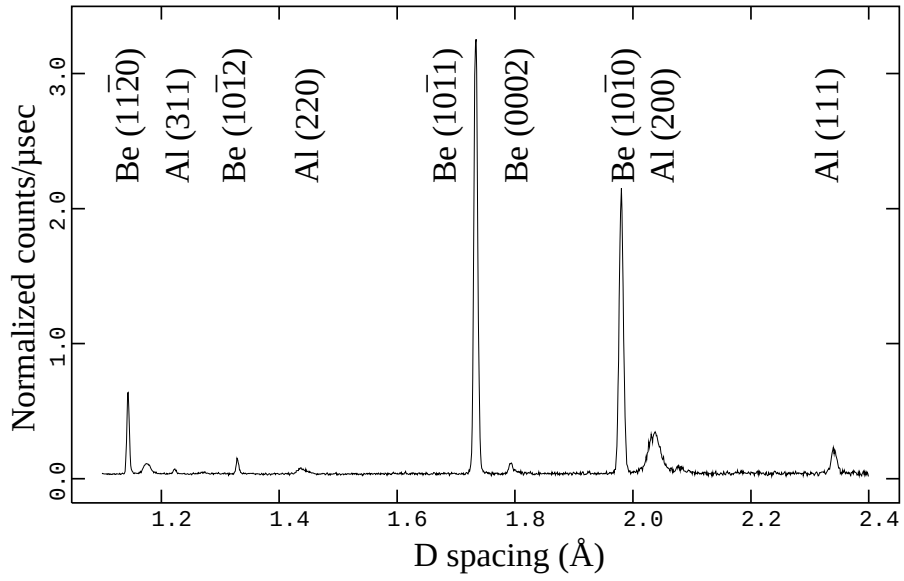

(b)

Figure 3.20: Diffraction spectra from planes a) parallel and b) perpendicular to the extrusion direction for AlBeMet. The fitted background response has been subtracted and the intensity has been normalized with respect to the incident spectrum.

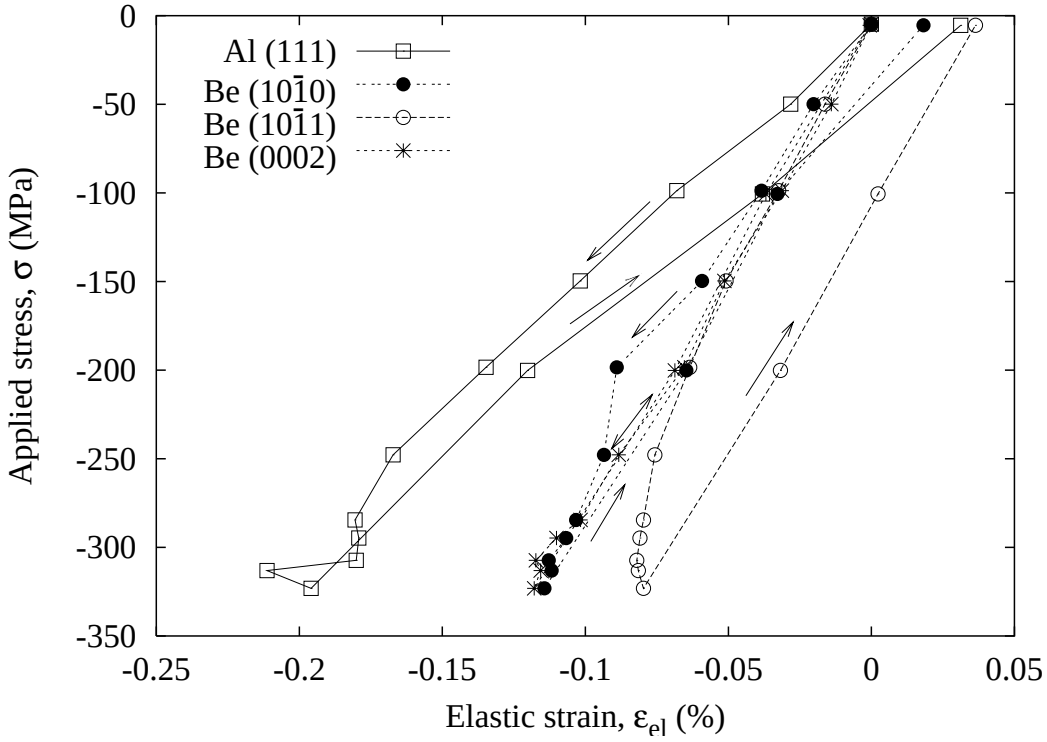

Figure 3.21: Applied stress vs. elastic strains for selected *hkl* planes with normals parallel to the loading direction (LANL Be-Al)

3.8.2 Results

Plotted in Figures 3.21–3.23 are strains for four selected planes in the Be-47.5Al-2.5Ag: Al (111), Be (0002), Be (10$\bar{1}$0), and Be (10$\bar{1}$1). Although data was obtained for all peaks, only strains from these peaks are shown to simplify the presentation. These strains are measured for planes whose normals are parallel (Figure 3.21) and perpendicular (Figure 3.22) to the loading direction and also +148° to the incident beam (Figure 3.23). In these and subsequent plots, the strains assumed zero initial values and do not account for the small thermal residual strains from processing (Table 3.3).

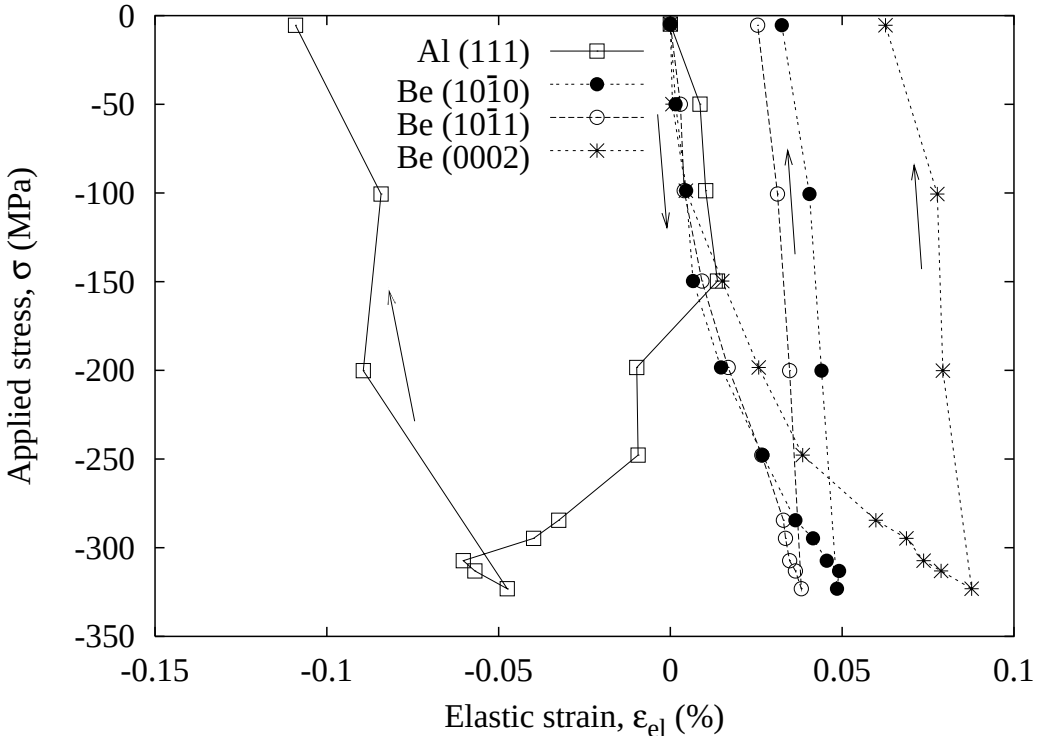

Figure 3.22: Applied stress vs. elastic strains for selected *hkl* planes with normals perpendicular to the loading direction (LANL Be-Al)

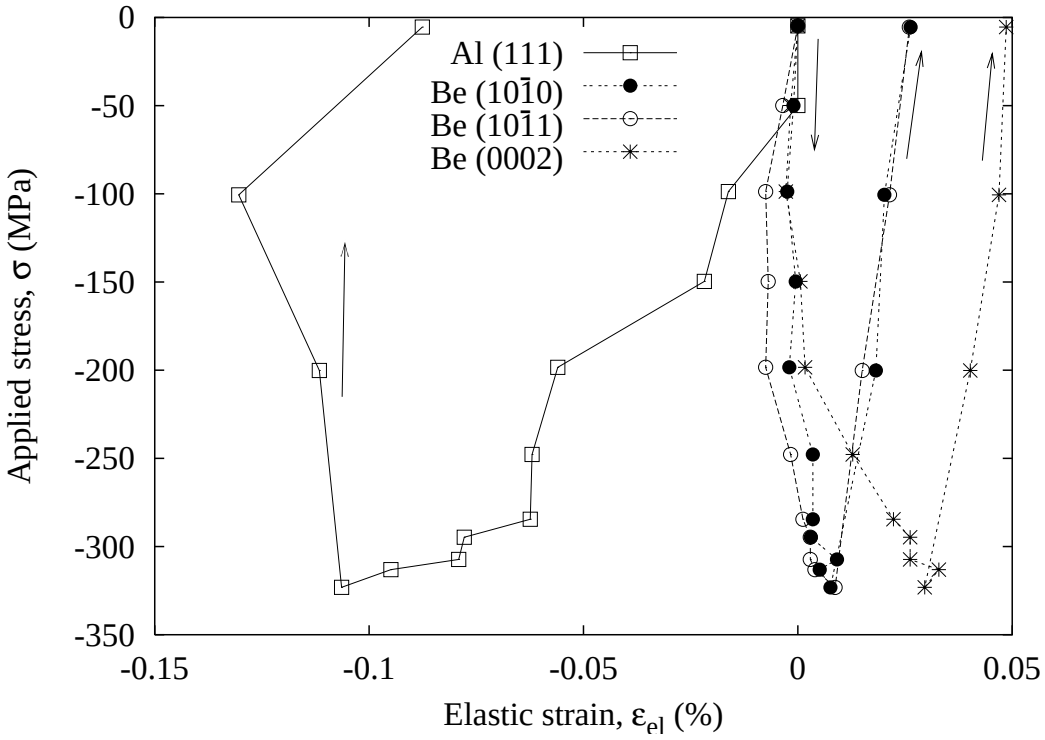

Figure 3.23: Applied stress vs. elastic strains for selected *hkl* planes with normals +148° to the incident beam (LANL Be-Al)

Be grains oriented such that the compression axis is perpendicular to the basal plane (0002) behave differently than those in the pyramidal plane $(10\bar{1}1)$ or the prismatic plane $(10\bar{1}0)$ orientations. This may be explained by the anisotropy in elastic constants for Be because the elastic stiffness for Be is higher along the c-axis than along the a-axis. The effects of anisotropy on the deformation behavior of single-crystal Be are reviewed in [8], and neutron diffraction studies of this behavior were performed in [65].

The microstructural deformation is complicated by both the mean phase (Be and Al) response and the hkl specific anisotropic behavior of the Be. Individual hkl responses will be the subject of further work. However, the significant aspects of the bulk deformation are captured by the response of the lattice parameters and, hereafter, the deformation will be described in terms of the strains calculated from the Rietveld refinements.

The results in Figures 3.24 and 3.25 represent mean phase elastic strains parallel and perpendicular to the loading direction, plotted against the applied stresses. These curves show the same characteristics as the strains in the individual planes.

Each phase (Figure 3.24) has two inflections, highlighted on Figure 3.26, where straight lines have been superimposed, identifying three distinct regions. Both phases remain elastic until -100 MPa, where the Al phase begins to yield. That is, for each additional increment in applied stress, the Al accommodates less elastic strain than below -100 MPa. Correspondingly, the Be bears a higher proportion of the load, which results in more elastic strain. Therefore, the Al curve deflects downwards, and the Be curves deflect in the opposite manner.

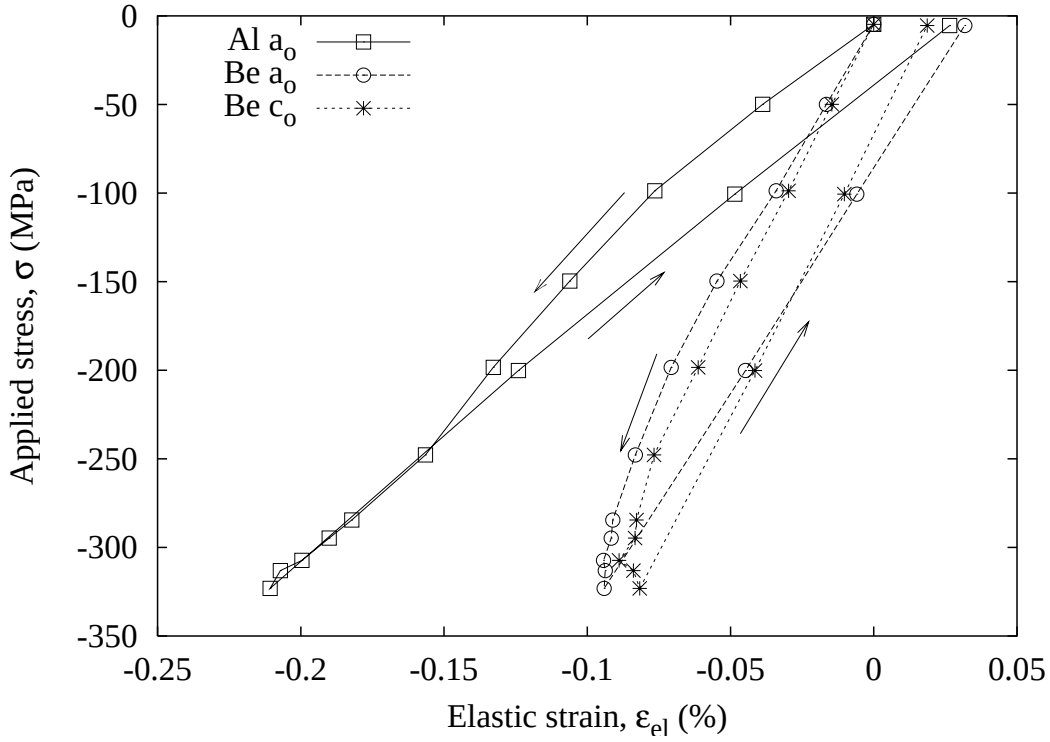

Figure 3.24: Applied stress vs. elastic strains parallel to the loading direction (LANL Be-Al)

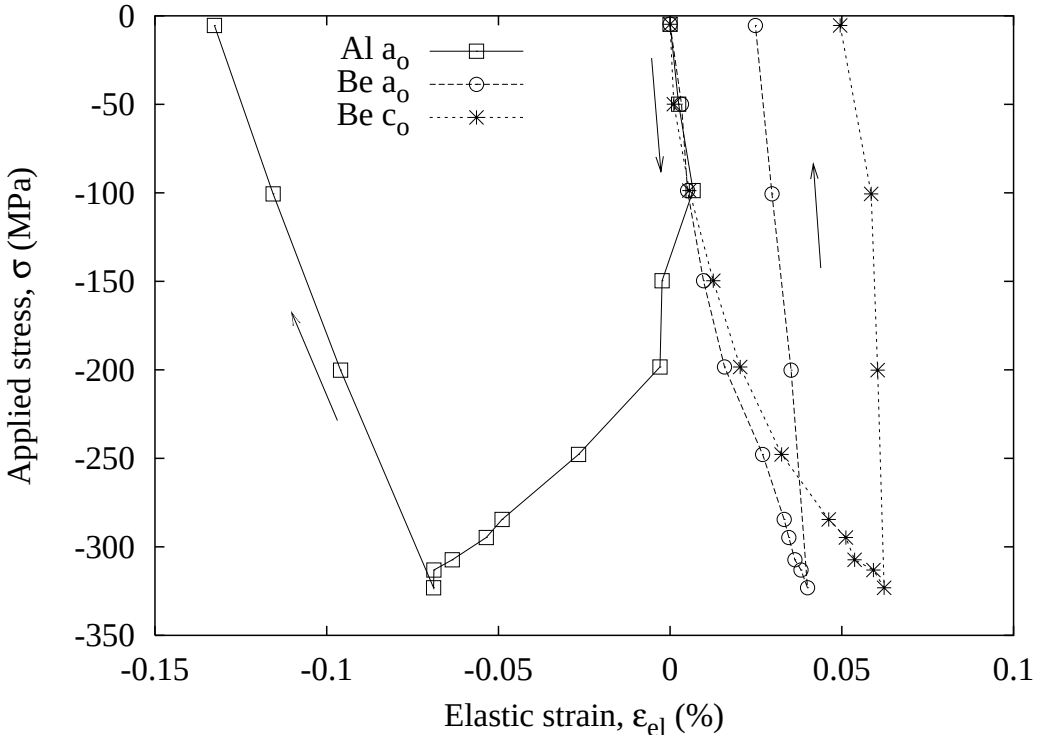

Figure 3.25: Applied stress vs. elastic strains perpendicular to the loading direction (LANL Be-Al)

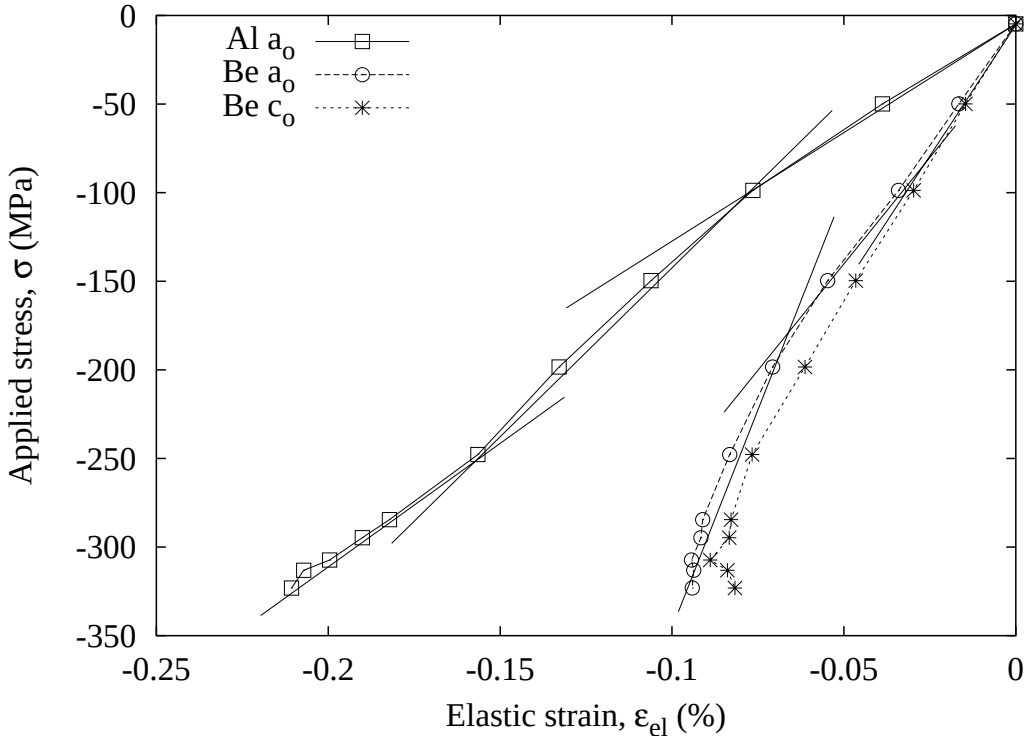

Figure 3.26: Applied stress vs. elastic strains parallel to the loading direction (LANL Be-Al) with straight lines superimposed that identify three distinct regions of these curves

Because Be has a higher elastic modulus than Al (300 GPa for Be and 70 GPa for Al), the inflections for Be are not as obvious as the inflections for Al. At −250 MPa, a second inflection occurs in both curves, where the Be curves deflect downwards and the Al curve deflects in the opposite direction. It can be inferred from this observation that the Be is beginning to yield, causing a redistribution of the strain between the two phases.

The unloading slopes of both phases were approximately the same as their initial slopes on loading. In both phases, the deformation-induced residual elastic strains upon unloading are tensile: 3.2×10^{-4} for Be $a_\circ$, 1.9×10^{-4} for Be $c_\circ$,

and 2.7×10^{-4} for Al $a_\circ$. Through the balance of forces, the volume average of residual stress cannot be tensile in both phases. However, this interpretation assumes that each phase had zero strain at the initial applied stress (Table 3.3). The total residual strain upon unloading, measured by the extensometer, was 1.1×10^{-2} (plastic strain) (Figure 3.19).

Perpendicular to the loading direction (Figure 3.25), upon initial loading, both phases experience tensile strain. At approximately -100 MPa, the stress-strain curve for the Al deflects in the opposite direction, and by -150 MPa, the Al phase exhibits a compressive strain. Aluminum continues to strain in compression up to the maximum applied stress of -323 MPa, reaching an elastic strain of -6.9×10^{-4}.

The Al is in compression when unloading begins, and it goes further into compression to a final elastic strain of -1.3×10^{-3}. The residual elastic strain in Be upon unloading is tensile: 2.5×10^{-4} for $a_\circ$ and 5.0×10^{-4} for $c_\circ$.

This result was surprising because no other composite studied in this manner had shown this type of behavior. The large compressive strains perpendicular to the load imply that the Be constrains the Al to such a degree that the Al experiences compressive hydrostatic stress in addition to the stress normal to the applied load. The data measured at 148° to the incident beam (Figure 3.23) also show large compressive strains in the Al, which supports the hypothesis that the Al undergoes a compressive hydrostatic stress. This constraint is caused by the wide disparity in the flow stresses and elastic constants of Be and Al, the anomalously low Poisson's ratio of 0.03 for Be, and the morphology of the microstructure. This will be discussed in detail, in connection with a model for

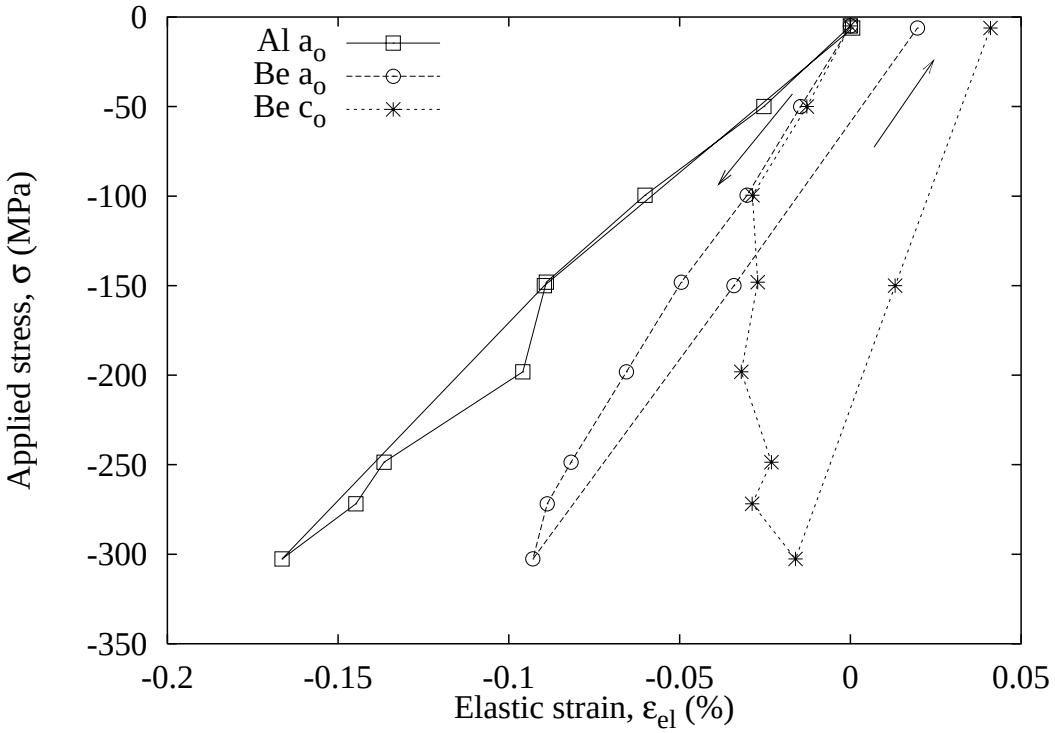

Figure 3.27: Applied stress vs. elastic strains parallel to the loading direction (AlBeMet)

deformation in this composite, in the following chapter.

Shown in Figures 3.27 and 3.28 are elastic strains parallel and perpendicular to the compression direction, respectively, for AlBeMet. The results show the same general characteristics as those found in the LANL Be-Al composite. The most distinctive characteristic is the large amount of compressive strain in the Al in a direction perpendicular to the compression axis (Figure 3.28), indicative of a large amount of hydrostatic stress. Also, a difference existed between the behavior of the Be planes along the *a*-axis and the *c*-axis, both parallel and perpendicular to the compression direction. This may be due to the anisotropy in elastic constants for Be.

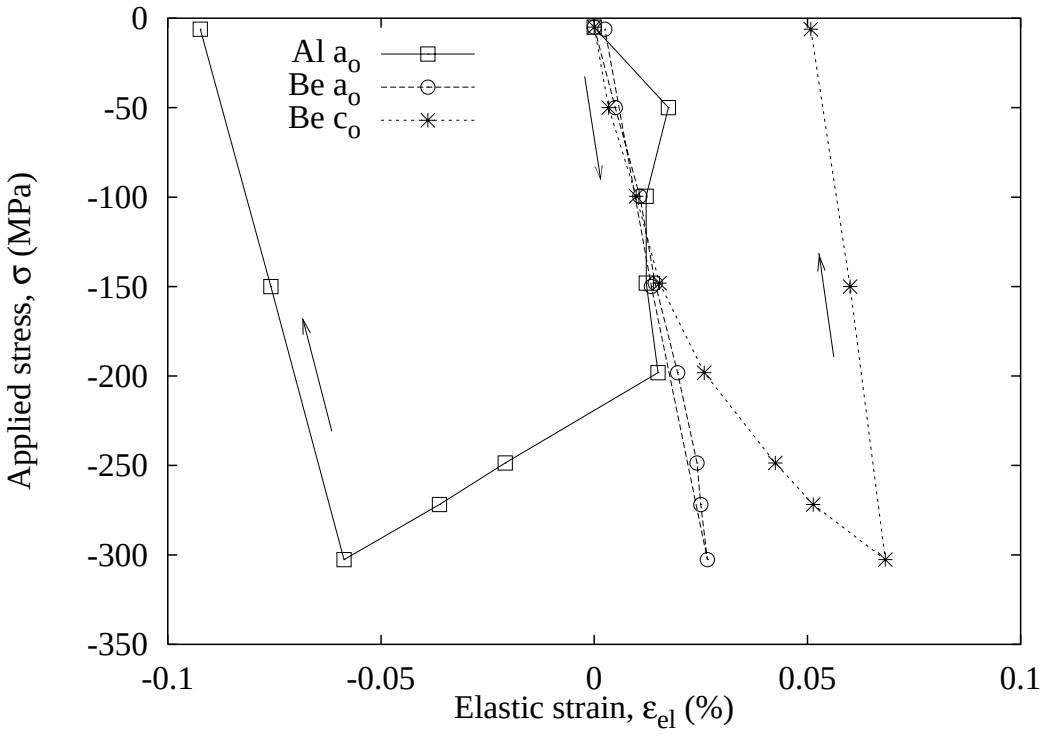

Figure 3.28: Applied stress vs. elastic strains perpendicular to the loading direction (AlBeMet)

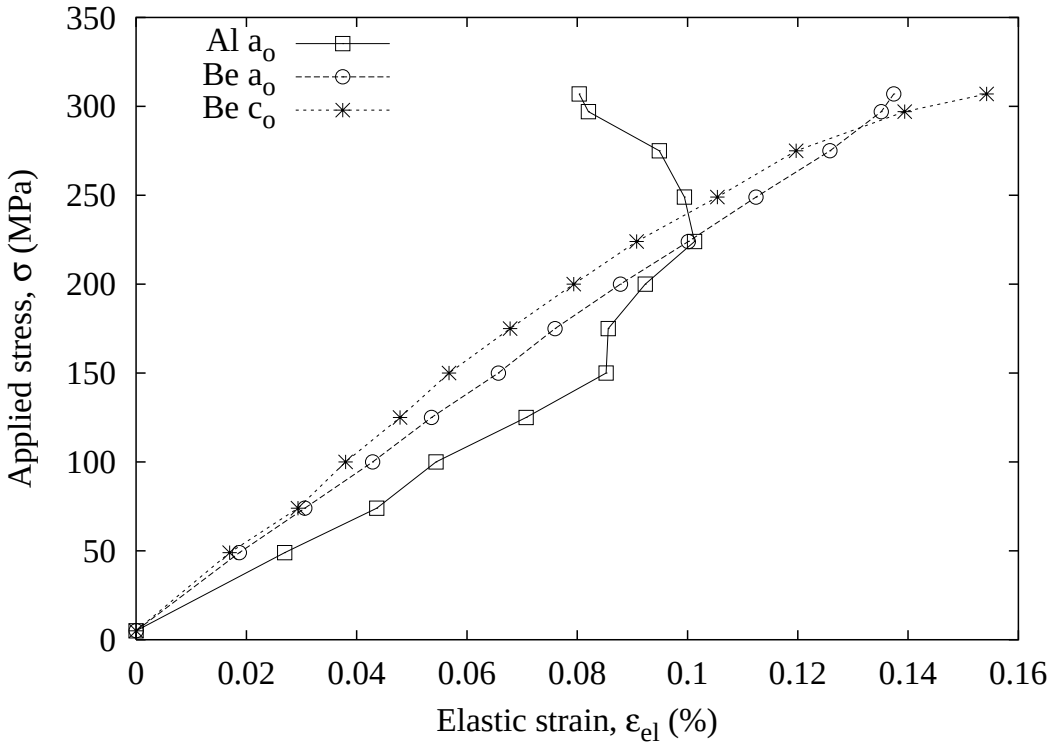

Figure 3.29: Applied stress vs. elastic strains parallel to the loading direction, loading only (LANL Be-Al)

The results from the tensile experiment on the LANL Be-Al are shown in Figures 3.29–3.31. For clarity, elastic strains parallel to the loading direction during the initial part of the loading cycle are shown in Figure 3.29, and Figure 3.30 is the first complete load and unload cycle.

Figure 3.31 shows the elastic strains perpendicular to the tensile axis. The diffraction data perpendicular to the tensile axis show a large amount of scatter, so it is unclear whether these data will provide any useful information.

The residual strain from processing this composite was measured and found to be small (see Table 3.3). This strain was not taken into account when plotting the strains during the neutron diffraction loading experiments, such as Figures 3.24

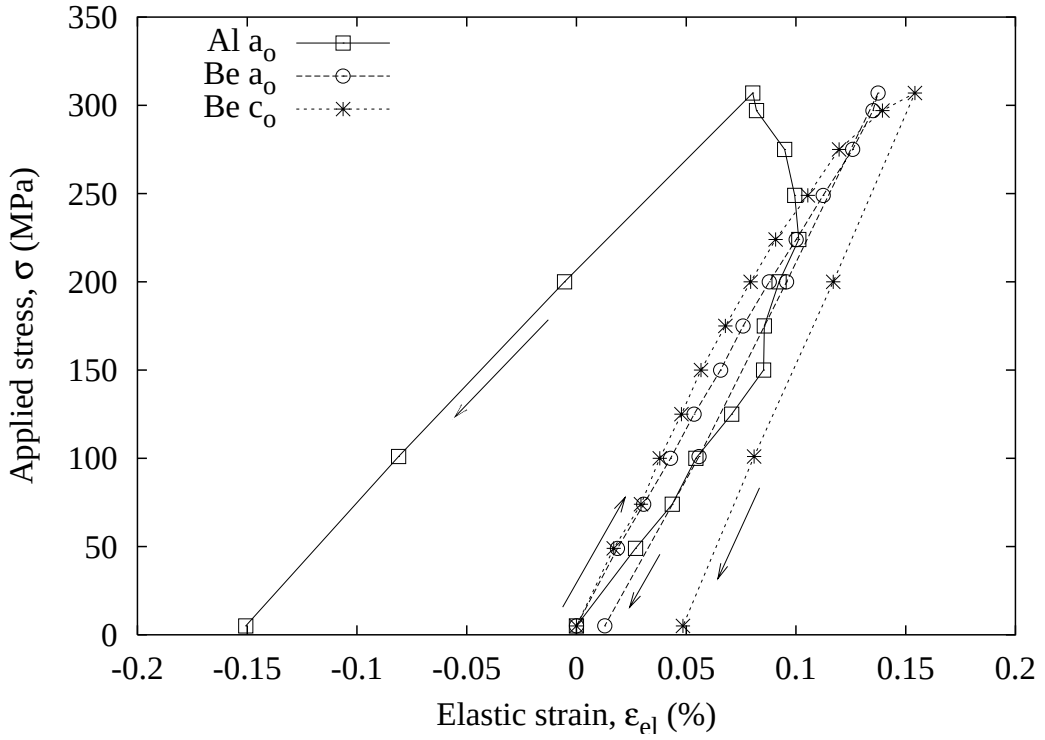

Figure 3.30: Applied stress vs. elastic strains parallel to the loading direction, loading and unloading (LANL Be-Al)

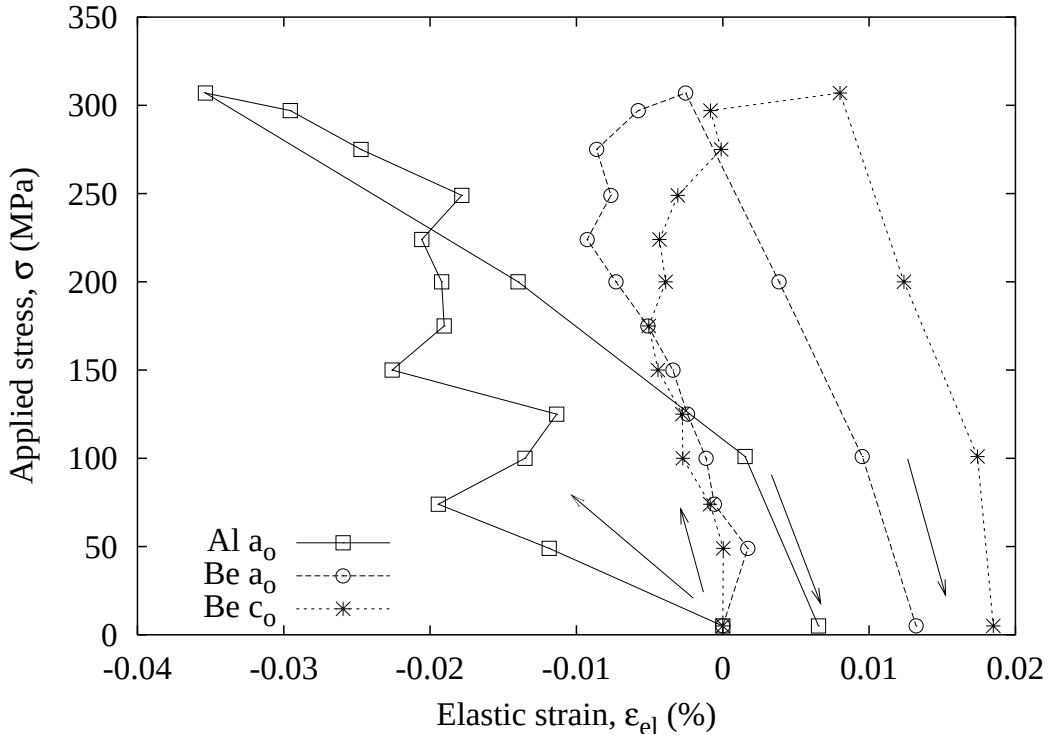

Figure 3.31: Applied stress vs. elastic strains perpendicular to the loading direction (LANL Be-Al)

or 3.25. These plots assumed a starting strain of 0 at the initial nominal load of -5 MPa. It is worthwhile to discuss the effect, if any, that the initial residual strain may have on the behavior of the composite.

The initial residual strains are on the order of 10^{-4}. This is a relatively small amount of strain when considering magnitude of strains shown in Figures 3.24 and 3.25. If one were to simply calculate the residual stress based on Young's modulus, the result would be between -50 and -100 MPa for Be and 25 MPa for Al. A couple of observations can be made. The most important result is that the sign of the residual stress is correct for each phase. Based on the difference in thermal expansion coefficients [Be (11.6×10^{-6} K^{-1}) and Al (23.6×10^{-6} K^{-1})], Be should be in compression and Al in tension, after cooling from the pressing temperature of 590 °C.

These residual strains should not affect the stress-strain characteristics obtained from the neutron diffraction experiments, given that the residual strains were low, except that since the Al is initially in tension, it would begin to yield at a slightly lower applied stress in the tensile test than in the compression test.

Chapter 4

Modeling and Interpretation

4.1 Summary of important results

The Be-Al composite has a unique microstructure because of rapid solidification and resultant liquid phase separation. The grain size is very fine, on the order of 1–3 μm. The morphology can be described as a three-dimensional interpenetrating microstructure, in which each phase consists of continuous "tendrils." Each tendril typically consists of only one grain and, therefore, can be considered single-crystal Be or Al. Single-crystal Be undergoes plasticity if oriented correctly. The Al accommodates shape changes in the Be by compatible deformation.

The properties of Be are anisotropic; therefore, the local stress and strain state may vary from grain to grain. In the composite, the material properties are isotropic because the tendrils are randomly oriented. Therefore, an averaging technique may be employed to describe the effective properties.

The emphasis is on the deformation and the way in which the two phases interact, as measured using neutron diffraction. Strains parallel to the compression axis (Figure 3.24) follow the qualitative trends in the hypothetical example, Figure 2.17. Strains perpendicular to the compression axis (Figure 3.25) were surprising. Strains in the Al were largely compressive transverse to the loading direction. No other composite studied in this manner in the literature has shown this type of behavior.

A sequence of geometrical, physical, and numerical models will be presented in the following sections to help explain these results.

4.2 Geometric models

It is beneficial to develop the simplest geometric model that captures the salient features of the morphology. One well-characterized representation comprises a fiber-reinforced metal matrix composite, which can be modeled as a regular array of cylinders. Generally, the composite is loaded either longitudinally or transversely to the fiber direction. The former describes an iso-strain condition, while the latter is closer to an iso-stress condition (as discussed in Chapter 2).

The Be-Al composite can be considered a mixture of these morphologies. It will be seen that the iso-stress model simulates the data more closely than the iso-strain model because the volume fraction of tendrils aligned with the loading direction is smaller than that transverse to the loading direction. This can be explained using a simple illustration, shown in Figure 4.1, for randomly oriented discontinuous fibers; the same concept can be applied to the Be-Al composite,

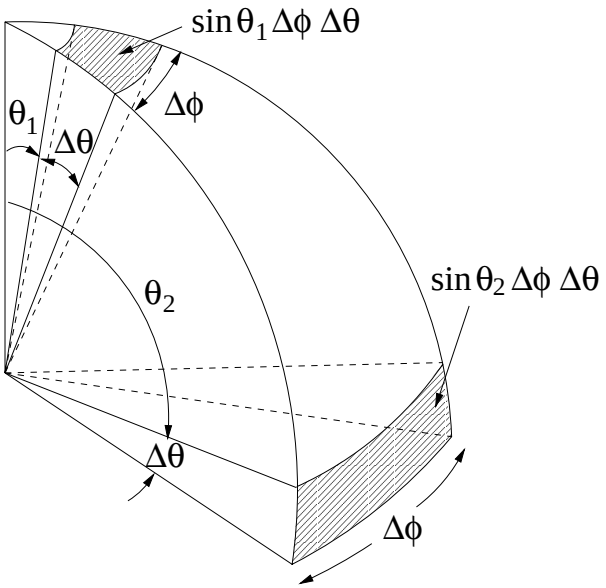

Figure 4.1: Illustration of volume fraction of fibers, V_f, oriented longitudinal vs. transverse to loading direction. V_f oriented at some angle θ from the vertical axis is $\int_0^{2\pi} \sin\theta \Delta\theta d\phi = 2\pi \sin\theta \Delta\theta$. Therefore, V_f oriented transversely is greater than those oriented longitudinally ($\sin\theta_2 > \sin\theta_1$).

where the morphology comprises randomly oriented "tendrils." The density of fibers intersecting a sphere is constant around the entire surface. The volume fraction of fibers within each "wedge" of the sphere is thus $\int_0^{2\pi} \sin\theta \Delta\theta d\phi = 2\pi \sin\theta \Delta\theta$. (See [107].) Since $\sin\theta_2 > \sin\theta_1$, the fraction oriented transverse to the loading is greater than the fraction oriented longitudinally.

4.3 Physical models

A simple illustration may help explain the concept of plastic constraint. In Figure 4.2, the stress-strain curves for a composite $(\sigma, \varepsilon)_c$ and *in situ* curves for each phase in the composite (α, β), are plotted for a hypothetical tensile experiment. Although this is not a quantitative model (it is neither isostress nor

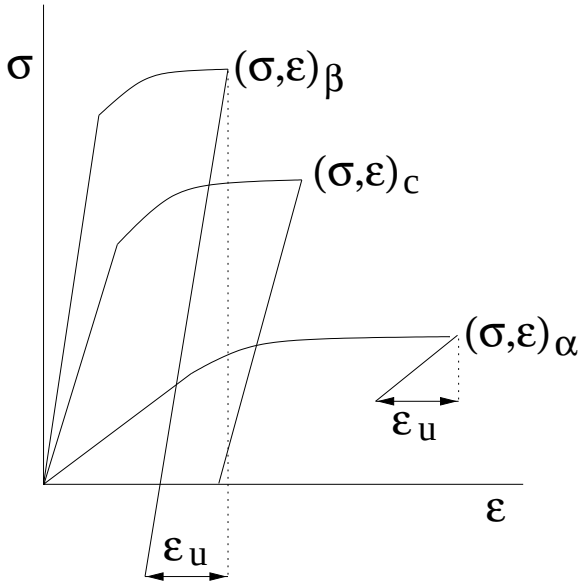

Figure 4.2: Strain compatibility during unloading of a composite $(\sigma, \varepsilon)_c$ consisting of a stronger, stiffer phase $(\sigma, \varepsilon)_\beta$ and a weaker, softer phase $(\sigma, \varepsilon)_\alpha$

isostrain), it is a useful illustration. The sample is loaded to some strain, ε_C, where the average stress is σ_C and then unloaded.

The β phase is stronger and stiffer then the α phase. Because of this, the stress and strain in each phase are different than the average values, $\sigma_\beta > \sigma_C > \sigma_\alpha$ and $\varepsilon_\beta < \varepsilon_C < \varepsilon_\alpha$.

Each phase unloads along a line with a slope corresponding to its elastic modulus. If we now assume an isostrain condition, each phase must undergo the same unloading strain, ε_U. Because the β phase has a higher modulus than the α phase, it must undergo a larger change in stress. Since the final average stress in the composite must be $\sigma_C = 0$, the residual stress will be tensile in the α phase and compressive in the β phase.

Neutron diffraction provides a unique way of studying composites because

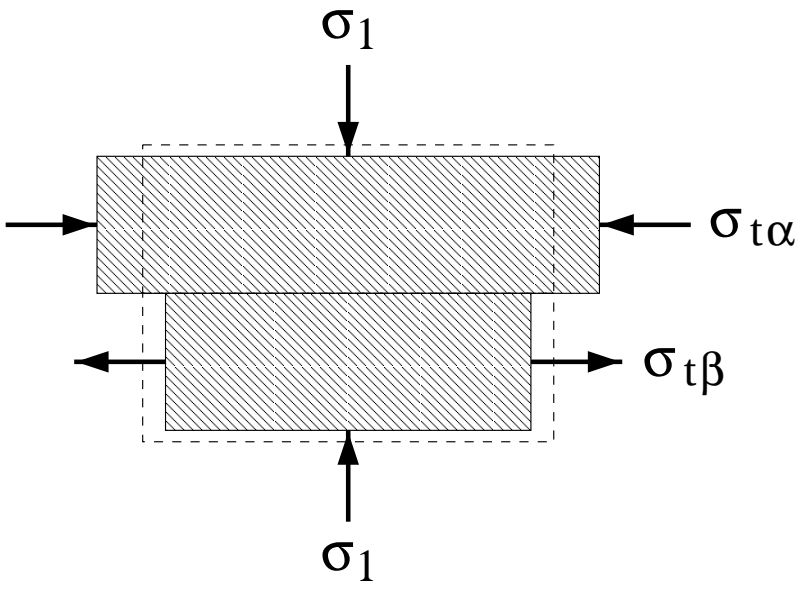

Figure 4.3: Illustration of strain compatibility effects

measurements can be made of strains in each phase individually. The results imply that as the composite is loaded, constraint causes a hydrostatic stress to develop in the Al, evident from the large transverse compressive strain. The reasons for the development of hydrostatic stresses include the disparity in the flow stresses for Al and Be, the difference in their elastic properties, and the morphology of the composite.

Following Poech [108], the material is idealized as an isostress composite with layers of alternating phases (Figure 4.3). In the direction of loading (designated by a subscript of 1)

$$\sigma_{1c} = \sigma_{1\alpha} = \sigma_{1\beta}. \tag{4.1}$$

The strains in the transverse directions, ε_t, are equal to the strain in the composite such that

$$\varepsilon_{tc} = \varepsilon_{t\alpha} = \varepsilon_{t\beta}. \tag{4.2}$$

As the composite is loaded in compression, it expands transversely. The transverse stresses in each phase must balance, giving

$$\sigma_{tc} = f_\alpha \sigma_{t\alpha} + f_\beta \sigma_{t\beta} = 0 \tag{4.3}$$

where f_α and f_β are the volume fractions of the phases. If the Poisson contraction is higher in the α phase than in the β phase, then the α experiences compression in the transverse direction. The strains in each phase are

$$\varepsilon_{t\alpha} = \frac{\sigma_{t\alpha} - \nu_\alpha(\sigma_{1\alpha} + \sigma_{t\alpha})}{E_\alpha} \tag{4.4}$$

and

$$\varepsilon_{t\beta} = \frac{\sigma_{t\beta} - \nu_\beta(\sigma_{1\beta} + \sigma_{t\beta})}{E_\beta}. \tag{4.5}$$

Using these relations together with Equations 4.1–4.3, the transverse stresses in each phase are

$$\sigma_{t\alpha} = -\frac{f_\beta}{f_\alpha}\sigma_{t\beta} = -\sigma_{1c}\left[\frac{E_\alpha\nu_\beta - E_\beta\nu_\alpha}{E_\beta(1-\nu_\alpha) + \frac{f_\alpha}{f_\beta}E_\alpha(1-\nu_\beta)}\right]. \tag{4.6}$$

In the Be-Al composites ($\nu_\alpha \approx 1/3$, $\nu_\beta \approx 0$, $f_\alpha = f_\beta = 1/2$, and $E_\beta \approx 4E_\alpha$)

$$\sigma_{t\alpha} = -\sigma_{t\beta} = \frac{4}{11}\sigma_{1c}. \tag{4.7}$$

When the applied stress σ_{1c} is compressive, the transverse stress in the Al is also compressive.

The hydrostatic component of stress σ_H is

$$\sigma_{H\alpha} = \frac{19}{33}\sigma_{1c} \tag{4.8}$$

and

$$\sigma_{H\beta} = \frac{1}{11}\sigma_{1c} \tag{4.9}$$

showing that the hydrostatic stress in the Al is greater than in the Be by more than a factor of 6.

The constraint has an even greater effect when the α begins to yield because its Poisson's ratio increases to 0.5.

4.4 Numerical models

A unit cell model was developed to examine the mechanical properties. This model was previously used to study alumina fiber-reinforced Al composites [97–99] and SiC fiber-reinforced titanium composites [109].

Fibers are assumed to be long, parallel cylinders arranged in a hexagonal array, shown in Figure 4.4(a). The properties of this array are closest to a composite with randomly distributed fibers [98]. It is transversely isotropic when both phases are elastic, but is anisotropic when either phase exhibits non-linear behavior.

Numerical studies were performed using the ABAQUS [1] finite element program. The load and symmetry conditions were taken from [96]. The model

[1] Hibbitt, Karlsson & Sorensen, Inc., Pawtucket, RI 02860

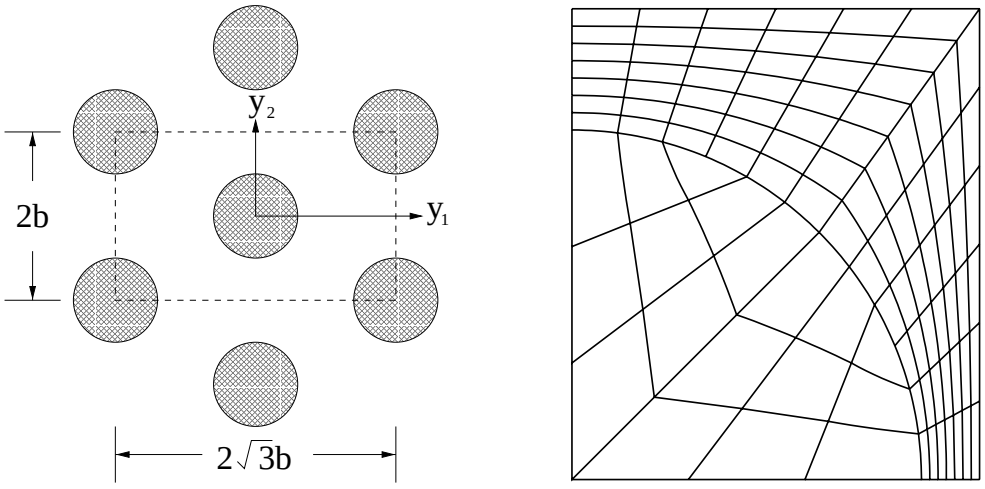

(a) Hexagonal array with unit cell identified

(b) FEM mesh for unit cell

Figure 4.4: FEM model (from [96])

comprised a two-dimensional unit cell from a hexagonal array of fibers loaded either axially (in the y_3 direction) or transversely (in the y_1 direction). An inversion symmetry in the displacement field exists at $(\frac{1}{2}\sqrt{3}b, \frac{1}{2}b)$ [see Figure 4.4(a)] when the displacements are taken to be zero at this point. Therefore, only one eighth of this unit cell needs to be modeled, shown in Figure 4.4(b). This mesh was determined to be sufficiently fine for the solutions to converge. Ten-node biquadratic quadrilateral, reduced integration generalized plane strain elements were used for both axial and transverse loading cases.

The boundary conditions ensured generalized plane strain. The following conditions were imposed on the displacements u_i:

$$u_2(y_2 = 0) = 0 \tag{4.10}$$

Table 4.1: Material properties used in finite element analysis

	ν	E (GPa)	$\sigma_\circ$ (MPa)	n
Al	0.3	70	75	10
Be	0.03	250	275	6

$$u_1\left(y_1 = \frac{\sqrt{3}}{2}b, y_2 = \frac{b}{2}\right) = 0 \tag{4.11}$$

$$u_1(y_1 = 0) = \text{constant} \tag{4.12}$$

$$u_2(y_2 = b) = \text{constant} \tag{4.13}$$

$$u_1\left(y_1 = \frac{\sqrt{3}}{2}b, y_2 = \frac{b}{2} + c\right) = -u_1\left(y_1 = \frac{\sqrt{3}}{2}b, y_2 = \frac{b}{2} - c\right) \tag{4.14}$$

where

$$0 \leq c \leq \frac{b}{2} \tag{4.15}$$

Both constituents are modeled as power law materials with isotropic hardening, where the stress strain relation reduces to

$$\varepsilon = \begin{cases} \frac{\sigma}{E} & \sigma < \sigma_\circ \\ \frac{\sigma_\circ}{E}\left(\frac{\sigma}{\sigma_\circ}\right)^n & \sigma \geq \sigma_\circ \end{cases} \tag{4.16}$$

where $\sigma_\circ$ is the initial yield stress. The input properties are listed in Table 4.1, where ν is Poisson's ratio and E is Young's modulus.

Properties for Be were fit from experimental data (Figure 3.9) obtained on material produced by rapid solidification, identical to the process used for the Be-Al composite. The *in situ* properties for the Al were estimated using data from the literature. Using these as a starting point, a parametric study was

performed using the finite element model to refine the properties. Tensile stress-strain curves were calculated using the model and compared to measured data (Figure 3.9). The properties that gave the best fit (Table 4.1) were used for subsequent analyses.

The unloading modulus during cyclic tensile tests (Figure 3.15) indicates that no debonding occurs at the Be-Al interfaces. Therefore, the model assumed perfect bonding.

Results are presented for Al as the fiber and Be as the matrix, with equal volume fractions. The composite was loaded in compression either axially or transversely to a final load of -323 MPa and then unloaded. The results are plotted as volume averages of the elastic strains in each phase, both parallel and perpendicular to the loading direction (as plotted for the experimental data, such as in Figures 3.24 and 3.25).

Figure 4.5 shows the elastic strains parallel to the loading direction for a simulation in which the stress was applied axially. Both Al and Be follow the same curve until -162 MPa, when the Al yields. At this point, the curves diverge, indicating that a higher proportion of the load is being carried by the Be. At -260 MPa, the Be begins to yield and continues to harden, up to the maximum load. Upon unloading, the slopes of both curves are equal to their initial loading slope. This slope is an "effective stiffness," $\bar{E}$, not an elastic modulus, because the applied stress is the ordinate, not the stress in each phase. These simulations do not correspond with the measurements.

The transverse applied stress simulations, shown in Figures 4.6 and 4.7, compare well with the measurements. In this case, the applied stress is in the y_1

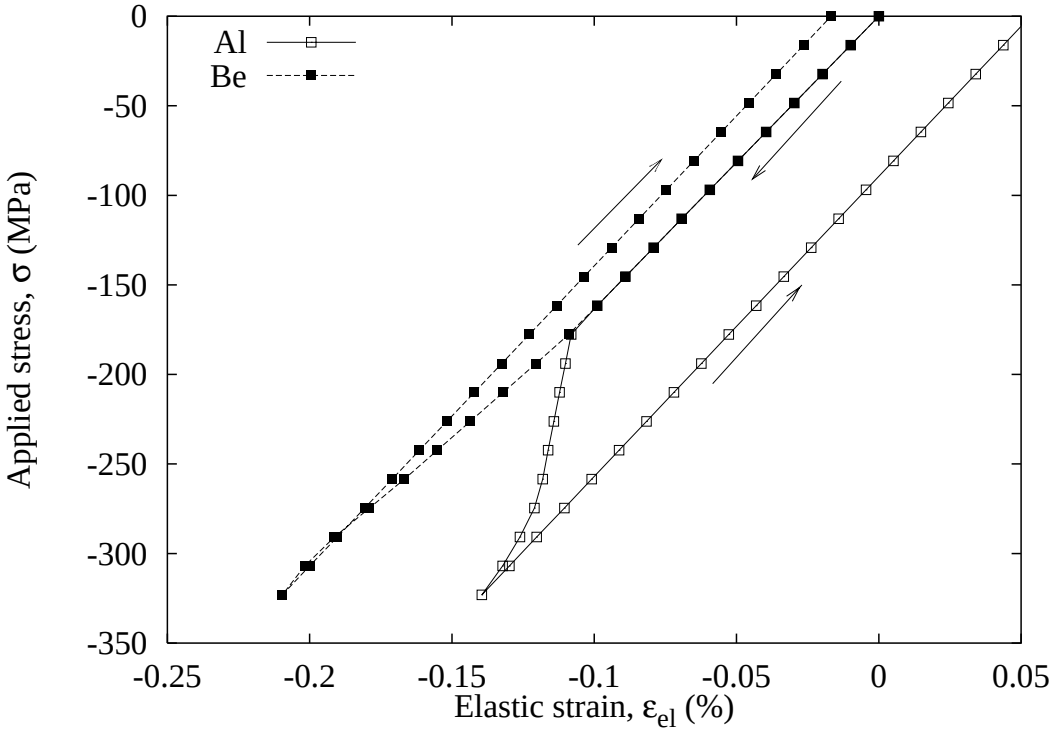

Figure 4.5: Simulation of applied axial stress vs. elastic strains parallel to the loading direction

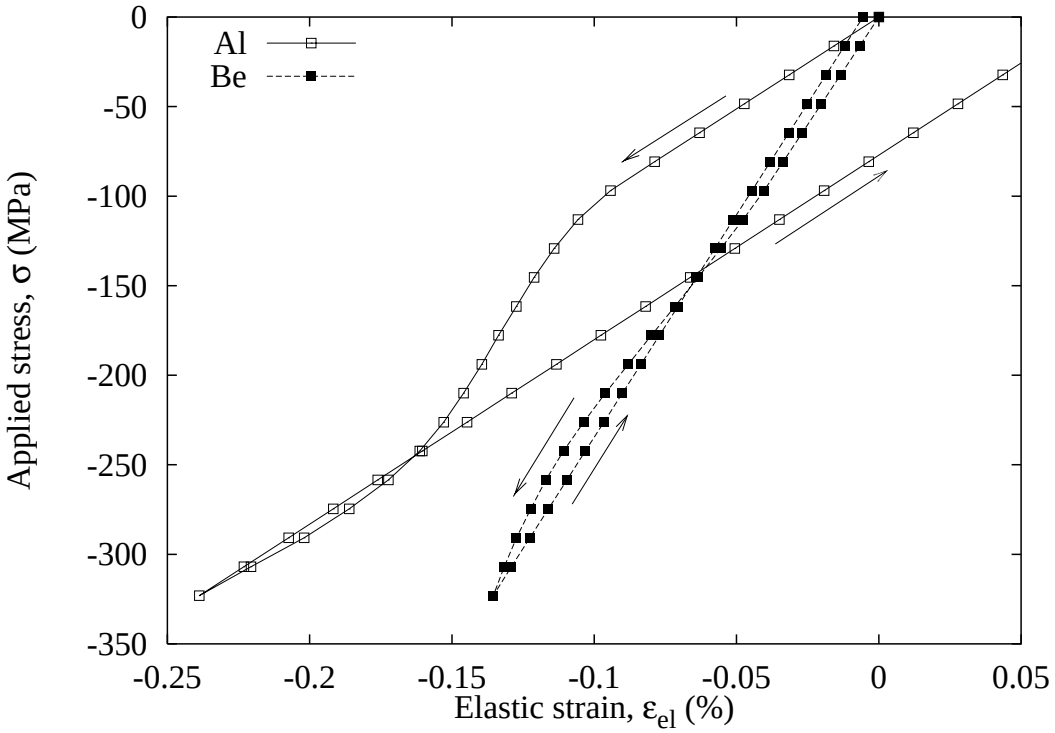

Figure 4.6: Simulation of applied transverse stress vs. elastic strains parallel to the loading direction

direction. The results are plotted as applied stress against elastic strains parallel and perpendicular to the loading direction.

Features of the experimental data can be interpreted by these simulations, especially the strain in the Al perpendicular to the loading direction (Figure 3.25). That is, the Al experiences transverse compressive strain during loading, as found experimentally. Also, because this is nearly an isostress condition, the simulation calculates a different $\bar{E}$ for each phase. The calculated $\bar{E}$ for Be and Al during the initial loading (parallel to the loading direction) are 249 and 103 GPa, respectively, compared with experimental measurements (Figure 3.24) of 283 and 120 GPa.

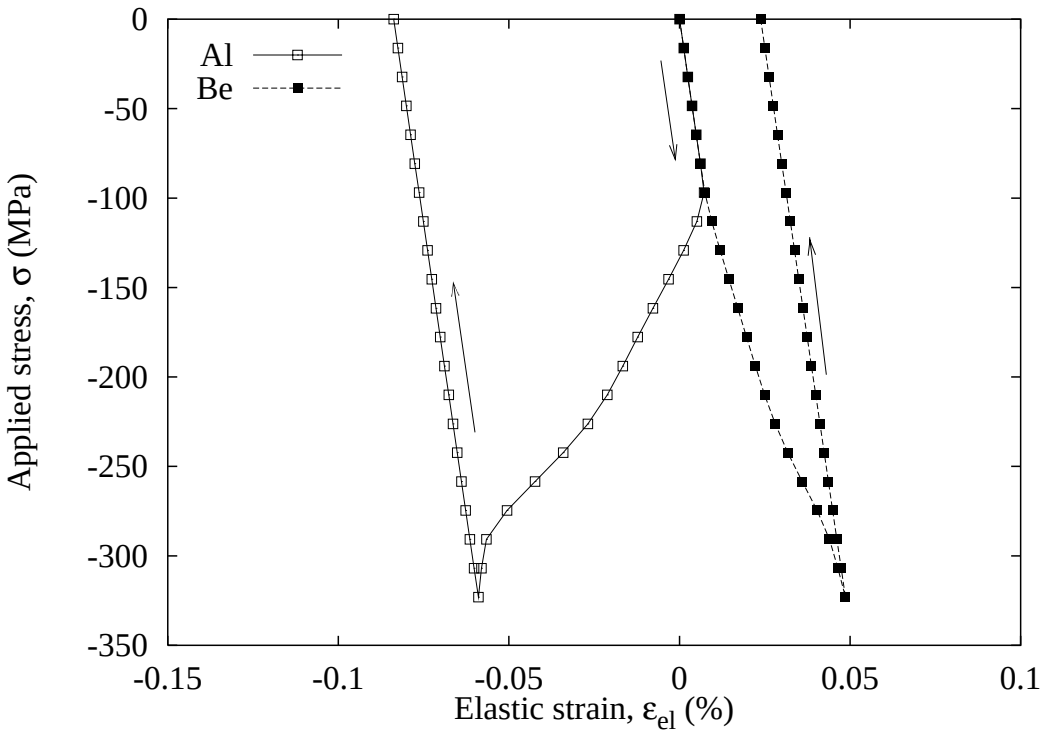

Figure 4.7: Simulation of applied transverse stress vs. elastic strains perpendicular to the loading direction

4.5 Discussion

The main focus of this research is on the interaction of the two phases during the initial stages of elastic and plastic deformation. This behavior was studied using neutron diffraction, a technique that was ideal for studying the deformation of two phases because it quantified the deformation of each phase individually. Compression tests were performed during neutron diffraction to provide the mode of interaction of the two phases. The repartitioning of load because of plastic flow in each phase was quantified. Tensile tests were also performed to examine the role of microcracking. No evidence of substantial microcracking was found.

The main observation regarding the deformation behavior is that the constraints in this composite are important and complex. A number of origins of constraint exist. *(i)* Beryllium has a Poisson's ratio of almost zero; therefore, it undergoes essentially no strain in the direction perpendicular to the loading axis. This imposes hydrostatic components of stress. Although each tendril of Be is essentially a single crystal, the Poisson effect is observed in a global sense, in which the Be phase is polycrystalline. *(ii)* The composite had an unusual microstructure and morphology, consisting of a very fine interpenetrating network of continuous phases. *(iii)* Plastic compatibility exists between the two phases. The Al is able to flow around the grains of Be, but the constraint imposed by the Be effectively raises its flow stress. The Al phase also can accommodate deformation in the Be phase.

In addition, constraints can also arise because of thermally induced residual strain. It was observed that residual strains from processing existed in both phases: compressive in the Be phase and tensile in the Al phase. The tensile

residual stress in the Al phase may in fact be on the order of the flow stress for normal polycrystalline Al. However, the flow stress for the Al phase in this composite is not the normal flow stress for Al in tension, but the constrained flow stress, which is much higher.

The development of these constraints can be explained and even reproduced using simple physical and numerical models. Moreover, even though the morphology of the Be-Al composite is difficult to represent, a simple two-dimensional model reproduces the salient features of the deformation behavior—namely, the development of a large hydrostatic stress component. A nearly iso-stress condition reproduced the observed deformation behavior much better than an iso-strain condition. This is consistent with the earlier finding that the volume fraction of tendrils aligned with the loading direction is smaller than the transverse volume fraction.

It is the purpose of this section to discuss how these constraints may influence mechanical properties. The primary effect may be to enhance the ductility of the composite. Failure of polycrystalline Be is normally due to cleavage, a stress-controlled fracture mode. The development of a high hydrostatic stress in the Al during deformation effectively raises the flow stress of the Al. Because of this, the Al is able to bear a larger proportion of the applied stress. This allows much more strain to be imparted into the composite before the stress in the Be reaches the critical stress for fracture. Moreover, the Be undergoes plastic flow before reaching its critical cleavage stress.

This can be illustrated with a simple model using Mohr's circles, shown in Figure 4.8. In this diagram, the principal stresses are plotted along the x-axis,

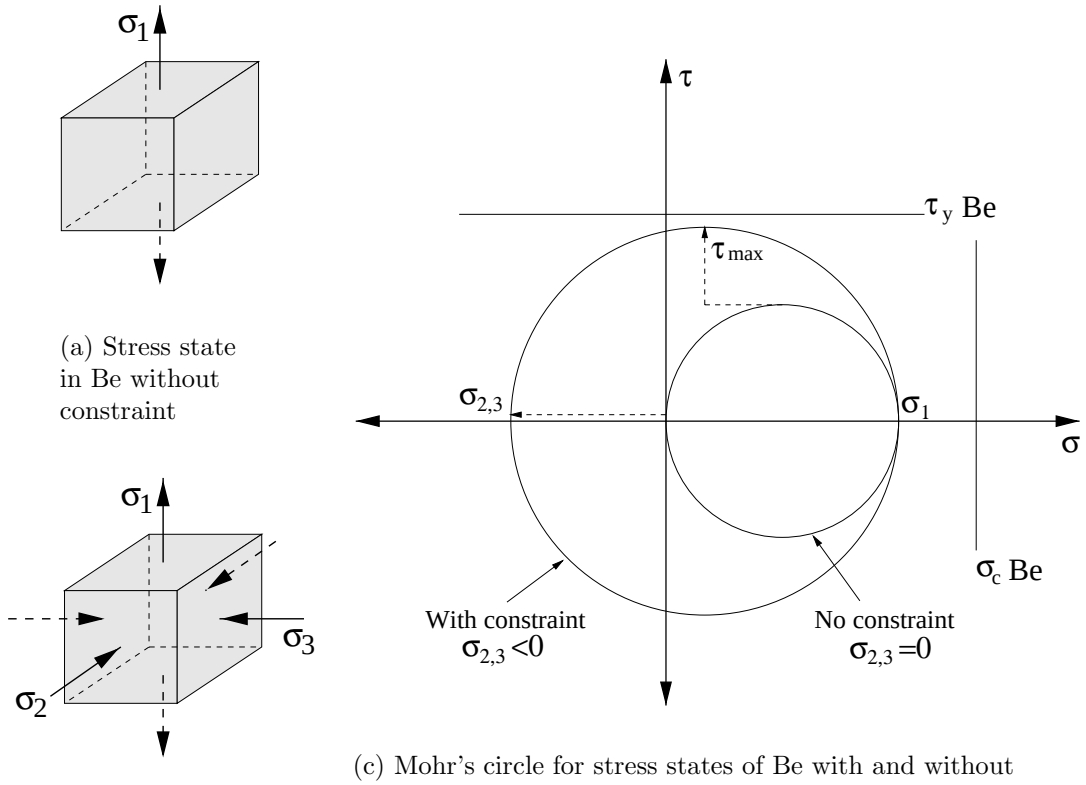

(a) Stress state in Be without constraint

(b) Stress state in Be with constraint

(c) Mohr's circle for stress states of Be with and without constraint

Figure 4.8: Mohr's circle representation of constraint effects in Be

and the shear stresses are plotted along the y-axis. The stress state for a tensile test on Be ($\sigma_1 > 0, \sigma_2 = \sigma_3 = 0$) is shown in Figure 4.8(a). This case is plotted in Figure 4.8(c), where σ_c represents the critical (normal) stress for fracture in Be, and τ_y represents the critical (shear) stress for plastic flow in Be. Normally, polycrystalline Be will reach its critical stress for fracture (σ_c) prior to substantial plastic flow (τ_y). However, it is evident from this illustration that it is possible to reach τ_y before σ_c by changing the stress state in the Be.

The stress in the Be transverse to the loading direction has the opposite sign

from the stress in the Al [Figure 4.8(b)]: the Be is in compression transverse to the loading direction, when tensile loading is applied. Along with the axial tension, this stress increases the maximum shear stress, facilitating plastic flow.

This same simple model can be used to illustrate the effect of constraint on the Al, shown in Figure 4.9. The stress state for a tensile test on Al ($\sigma_1 > 0, \sigma_2 = \sigma_3 = 0$) is shown in Figure 4.9(a). In this case, hydrostatic stress components due to constraint require $\sigma_2, \sigma_3 > 0$, shown in Figure 4.9(b). The resulting Mohr's circle is shown in Figure 4.9(c). For the same applied stress (σ_1), the maximum shear stress is decreased, effectively raising the flow stress of the Al.

The data from this work and others support this hypothesis. For example, it was found that as the strength of the Al was increased due to age-hardening, the ductility of the composite also increased. This is counter-intuitive because strength and ductility are sometimes inversely proportional. However, it fits with the current hypothesis because, as the flow stress of the Al is increased, the Al bears a higher proportion of the load and, thus, increases the required applied stress to reach the cleavage stress in the Be.

Evidence from microscopy studies (see Figure 3.11) also supports this hypothesis. Observations of fracture in this composite suggested that the Al was fully constrained by the Be until fracture. The Al grains do not undergo substantial necking, as they might in other metal matrix composites. In fact, the phases look almost identical in appearance on the fracture surface. Each "tendril" consists of a single grain of either Be or Al. The size of the "ductile dimples" was essentially the grain size of the Al. The fine grain size of the Al means that each facet on the fracture surface was caused by only one void. Also, no evidence of

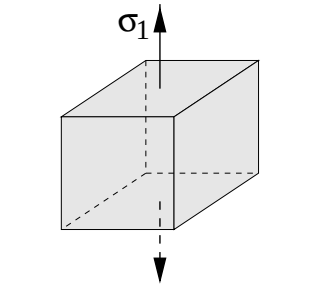

(a) Stress state in Al without constraint

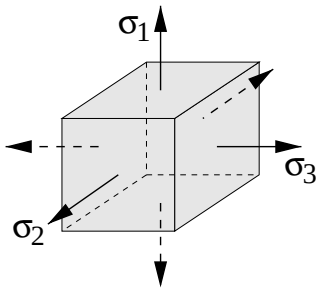

(b) Stress state in Al with constraint

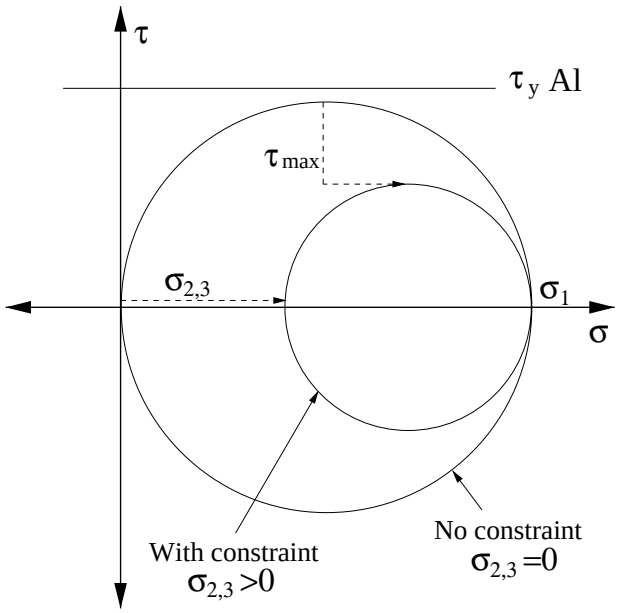

(c) Mohr's circle for stress states of Al with and without constraint

Figure 4.9: Mohr's circle representation of constraint effects in Al

microcracking or debonding near the fracture surface was observed.

To summarize, the initial sequence of elastic and plastic deformation in this Be-Al composite can be described as follows. As the composite is loaded, both phases load elastically. Because of the morphology and the elastic properties of the phases, a hydrostatic stress develops in the Al. Therefore, the Al is able to bear a larger proportion of the applied load, and the stress in the Be is lower than the cleavage stress. Once the Al begins to yield, the constraint increases even further.

Eventually the Be begins to plastically deform. The Be can flow plastically before it begins to fracture because each Be tendril is a single crystal surrounded by Al, which can accommodate shape changes through compatible deformation.

In addition, the critical stress for fracture of Be increases with decreasing grain size ($\sigma_c \propto D^{-1/2}$) and the amount of hardening also increases ($\sigma_c - \sigma_y \propto D^{-1/2}$) (see Figure 2.6). The fine grain size of the composite enhances its ductility by elevating its fracture stress.

Chapter 5

Conclusions

The physical and mechanical properties of Be, especially the combination of low density and high elastic modulus, make it an attractive structural material. However, intrinsic brittleness problems exist with monolithic Be related to its hexagonal close-packed crystal structure. The Be-Al material studied in this research had a unique composite microstructure that obviates this problem. It consisted of interpenetrating phases formed from liquid immiscibility.

The approach taken to understand its behavior was to use neutron diffraction to monitor the elastic strains in each phase, in combination with studies of the overall mechanical behavior. The results were interpreted in terms of models that describe the interaction between the phases and the local stress states established by compatibility requirements.

Parallel to the loading direction, the Al began to yield at about -100 MPa; whereas, the Be phase appeared to deform plastically at -200 to -250 MPa. The Al developed a large hydrostatic stress enabling it to bear a substantial

proportion of the applied load (and even maintain this load when the Be yielded). This raised the applied load required to reach the critical stress for cleavage fracture in Be.

Perpendicular to the loading direction, the Al was in compression at applied stresses above −150 MPa. This was a result of the hydrostatic stress that arises because the Al was highly constrained by the Be, which does not expand perpendicular to the loading direction. Upon unloading, the Al retained a compressive residual strain, while the Be had a smaller tensile residual strain.

Finite element analyses using a relatively simple model simulated this behavior quite well. A hexagonal array of Al cylinders in a Be matrix, when loaded in the transverse direction, reproduced a similar constraint. The resulting σ_{app} vs. ε_{el} curves both parallel and perpendicular to the loading direction were consistent with the experimental observations.

The mechanical behavior of this composite was largely influenced by the constraints developed during deformation. These constraints were very complex and had a number of origins. *(i)* Beryllium has unusual elastic properties—a high elastic modulus and low Poisson's ratio. *(ii)* The microstructure and morphology of the composite is unique—an interpenetrating network of two continuous phases with a very fine grain size. *(iii)* Compatible plastic deformation occurs—Al is constrained, but can plastically flow and accomodate deformation in the Be. Because of these constraints, the Be-Al composite had a yield strength of 300–400 MPa, yielded plastically, and exhibited a substantial amount of ductility, on the order of 10% elongation, prior to fracture.

A number of areas exist for further research. The fine microstructure and

unusual morphology of this composite were among the factors governing its deformation behavior and excellent mechanical properties. Similar experiments should be performed using Be-Al with different microstructures to examine the importance of specific microstructural parameters on the deformation behavior. For example, the deformation behavior of cast Be-Al, which has a much larger grain size, should be studied. The larger scale of the microstructure may lead to microcracking in the Be because of incompatible deformation between Be grains. A larger grain size may also cause a smaller fracture stress such that the Be undergoes cleavage at a smaller applied load.

Plasticity in the Be should be carefully studied to identify the specific deformation mechanisms and the relative importance of twinning, basal plane slip, and other slip systems.

Experiments should be performed as a function of temperature to examine the role of diffusional processes in the deformation behavior of this composite. In addition, the role of thermal residual strain from processing on the deformation behavior of the composite needs to be studied further.

The fracture properties of Be-Al composites should be studied further. For example, if the Be fails by cleavage, the orientation of Be grains on the fracture surface can be examined to determine whether they fractured along their preferred cleavage plane: the basal plane. Other fracture properties (fracture toughness and fatigue resistance, for example) need to be understood before considering Be-Al as a viable composite for structural applications.

Bibliography

[1] Donald Webster and Gilbert J. London, editors. *Beryllium Science and Technology*, volume 1. Plenum Press, New York, 1979.

[2] Dennis R. Floyd and John N. Lowe, editors. *Beryllium Science and Technology*, volume 2. Plenum Press, New York, 1979.

[3] S. F. Pugh. Plasticity of hexagonal metals and its variation with temperature. Technical Report MIR 1290, Atomic Energy Research Establishment, 1953.

[4] H. Conrad and I. Perlmutter. Beryllium as a technological material. In *Proc. Int. Conf. Beryllium Met.*, pages 319–372, Grenoble, 1965. French University Press, Paris.

[5] D. J. Silversmith and B. L. Averbach. Pressure dependence of the elastic constants of beryllium and beryllium-copper alloys. *Phys. Rev.*, 1B:567–571, January 1970.

[6] E. Schmid and W. Boas. *Plasticity of Crystals with Special Reference to Metals*. F. A. Hughes & Co. Limited, London, 1950.

[7] R. M. Treco. Thermal expansion characteristics of beryllium. *Journal of Metals*, 188:1274–1276, 1950.

[8] Fritz Aldinger. Flow and fracture of single crystals. In Donald Webster and Gilbert J. London, editors, *Beryllium Science and Technology*, volume 1, chapter 2. Plenum Press, New York, 1979.

[9] H. J. Saxton and G. J. London. Flow and fracture of polycrystalline beryllium. In Donald Webster and Gilbert J. London, editors, *Beryllium Science and Technology*, volume 1, chapter 3. Plenum Press, New York, 1979.

[10] S. F. Pugh. Relations between the elastic moduli and the plastic properties of polycrystalline pure metals. *Phil. Mag.*, 45:823–843, August 1954.

[11] H. T. Lee and R. M. Brick. Slip & twinning in single crystals of beryllium. *Journal of Metals*, 4:147–148, 1952.

[12] G. L. Tuer and A. R. Kaufmann. Ductility of beryllium as related to single crystal deformation and fracture. In D. W. White, Jr. and J. E. Burke, editors, *The Metal Beryllium*, pages 372–424. The American Society for Metals, Cleveland, Ohio, 1955.

[13] H. T. Lee and R. M. Brick. Deformation of beryllium single crystals at 25 to 500 °C. *Transactions of the ASM*, 48:1003–1037, 1956.

[14] D. McLean. The plastic behavior of beryllium and some other metals. In *Proc. Int. Conf. Beryllium Met.*, pages 3–14, Grenoble, 1965. French University Press, Paris.

[15] A. Moore and G. C. Ellis. The toughness of beryllium. In *Proc. Int. Conf. Beryllium Met.*, pages 378–384, Grenoble, 1965. French University Press, Paris.

[16] V. Damiano, G. London, G. Stone, and H. Conrad. Mechanical properties of commercial purity and of distilled and zone refined beryllium. Technical Report AFML-TR-67-126, Air Force Materials Laboratory, 1967.

[17] Daniel Caillard, Alain Couret, and Guy Molenat. Mechanisms of yield stress anomalies in beryllium and Ni_3Al. *Materials Science and Engineering A*, A164(1–2):69–81, May 1993.

[18] V. V. Damiano, B. Lalevic, and G. L. London. Investigations relating to the brittleness of beryllium. Technical Report AFML-TR-69-70, Air Force Materials Laboratory, March 1969.

[19] A. N. Stroh. The cleavage of metal single crystals. *Phil. Mag.*, 3:597–606, 1958.

[20] R. K. Govila and M. H. Kamdar. Cleavage in beryllium monocrystals. *Metallurgical Transactions*, 1:1011–1018, April 1970.

[21] V. V. Damiano, G. J. London, D. F. Kaufman, and L. R. Aronin. Deformation and fracture of beryllium bicrystals. *Transactions of The Metallurgical Society of AIME*, 242:2423–2431, December 1968.

[22] Norman P. Pinto. Properties. In Dennis R. Floyd and John N. Lowe, editors, *Beryllium Science and Technology*, volume 2, chapter 16. Plenum Press, New York, 1979.

[23] S. H. Gelles. Impurity effects in beryllium. Technical Report MCIC-72-06, Metals and Ceramics Information Center, March 1972.

[24] A. James Stonehouse. Impurity effects in beryllium. In Donald Webster and Gilbert J. London, editors, *Beryllium Science and Technology*, volume 1, chapter 5. Plenum Press, New York, 1979.

[25] Graham I. Turner. Grain size effects. In Donald Webster and Gilbert J. London, editors, *Beryllium Science and Technology*, volume 1, chapter 4. Plenum Press, New York, 1979.

[26] M. F. Ashby. *Materials Selection in Mechanical Design*. Pergamon Press, New York, first edition, 1992.

[27] M. F. Ashby. Overview No. 106: Criteria for selecting the components of composites. *Acta Metallurgia et Materialia*, 41(5):1313–1335, 1993.

[28] D. J. Lahaie, J. D. Embury, and M. F. Ashby. Scale dependent composite design charts. *Scripta Metallurgica et Materialia*, 32(1):133–138, 1995.

[29] G. I. Turner and R. A. Lane. The effect of powder particle size on the mechanical properties of hot pressed high purity beryllium, paper 15. In *Beryllium 1977, Proc. 4th International Conference on Beryllium*. The Royal Society, London, 1977.

[30] D. Hull and D. J. Bacon. *Introduction to Dislocations*. Pergamon Press, New York, 1984.

[31] Hugh S. Cooper. Al-Be alloys. U. S. Patent No. 1,254,987, January 1918.

[32] Beryllium-aluminum alloy extrusions save weight in Minutemann III Missile. *Industrial Heating*, 38:666–672, April 1971.

[33] R. J. Duba, A. C. Haramis, R. F. Marks, L. Payne, and R. D. Sessing. YF-12 Ventral Fin Program, final report, vol. 1. Technical Report CR-144971, NASA, 1976.

[34] D. Hashiguchi, A. N. Ashurst, F. C. Grensing, and J. M. Marder. Aluminum-beryllium alloys for aerospace applications. In *International Symposium on Advanced Materials for Lightweight Structures, ESTEC, Noordwijk, The Netherlands, March 25–27, 1992*, pages 165–169, 1992.

[35] F. C. Grensing and D. Hashiguchi. Properties of wrought aluminum–beryllium alloys. In *Advances in Powder Metallurgy and Particulate Materials—1993. Vol. 4. Processing, Properties and Applications, Nashville, Tenessee, May 16–19, 1993*, pages 179–189, Princeton, NJ, 1993. Metal Powder Industries Federation.

[36] L. M. Beltz and D. J. Chellman. The effects of beryllium content on the properties of powder metallurgy aluminum-beryllium alloys. In *Advances in Powder Metallurgy and Particulate Materials—1993. Vol. 4. Processing, Properties and Applications, Nashville, Tenessee, May 16–19, 1993*, pages 191–200, Princeton, NJ, 1993. Metal Powder Industries Federation.

[37] James M. Marder. Aluminum-beryllium alloys. *Advanced Materials & Processes*, 152(4):37–40, October 1997.

[38] V. C. Nardone and T. J. Garosshen. Evaluation of the tensile and fatigue behavior of a powder metallurgy beryllium/aluminum alloy. *Journal of Materials Science*, 32(10):2549–2557, 1997.

[39] William T. Nachtrab, Kevin R. Raftery, and Thomas D. Sanborn. Beryllium aluminum—a new alloy for investment casting. In P. W. Lee and B. L. Ferguson, editors, *Proceedings of the 3rd Near Net Shape Manufacturing Conference*, pages 27–32. ASM International, Pittsburgh, PA, 1993.

[40] Nancy F. Levoy. Ductile-ductile beryllium aluminum metal matrix composite manufactured by extrusion, final report. Technical Report AD-A296 792, Nuclear Metals, Inc., Concord, MA, June 1995.

[41] William T. Nachtrab, Nancy F. Levoy, and Raymond L. White III. Ductile, light weight, high strength beryllium-aluminum cast composite alloy. U. S. Patent No. 5,417,778, May 1995.

[42] William T. Nachtrab, Nancy F. Levoy, and Kevin R. Raftery. Light weight, high strength beryllium-aluminum alloy. U. S. Patent No. 5,421,916, June 1995.

[43] William T. Nachtrab, Nancy F. Levoy, and Kevin R. Raftery. Light weight, high strength beryllium-aluminum alloy. U. S. Patent No. 5,603,780, February 1997.

[44] William T. Nachtrab and Nancy Levoy. Beryllium-aluminum alloys for investment castings. *Advanced Materials & Processes*, 151(5):23–25, May 1997.

[45] V. C. Nardone and T. J. Garosshen. Evaluation of the tensile and fatigue behavior of ingot metallurgy beryllium/aluminum alloys. *Journal of Materials Science*, 32(15):3975–3985, 1997.

[46] J. H. Perepezko and W. J. Boettinger. Use of metastable phase diagrams in rapid solidification. In L. H. Bennett, T. B. Massalski, and B. C. Giessen, editors, *MRS Symposium on Alloy Phase Diagrams*, volume 19, pages 223–240. Elsevier, North Holland, 1983.

[47] Y. Nakagawa. Liquid immiscibility in copper-iron and copper-cobalt systems in the supercooled state. *Acta Metallurgia et Materialia*, 6:704–711, 1958.

[48] J. L. Murray and D. J. Kahan. The Al-Be system. *Bulletin of Alloy Phase Diagrams*, 4(1):50–55, 1983.

[49] W. J. Boettinger and J. H. Perepezko. Fundamentals of rapid solidification. In S. K. Das, B. H. Kear, and C. M. Adam, editors, *Rapidly Solidified Crystalline Alloys*, pages 21–58, Warrendale, PA, 1985. The Metallurgical Society of AIME.

[50] David C. Van Aken and Hamish L. Fraser. The microstructures of rapidly solidified hyper-eutectic Al-Be alloys. *Acta Metallurgia et Materialia*, 33(6):963–974, June 1985.

[51] David C. Van Aken. *Al-Be Composites Produced by Rapid Solidification*. PhD thesis, University of Illinois, 1986.

[52] D. C. Van Aken and H. L. Fraser. Nucleation in the presence of a metastable liquid miscibility gap in the Al-Be system. In E. W. Collings and C. C. Koch, editors, *Undercooled Alloy Phases*, pages 413–431. Metallurgical Society of AIME, Warrendale, PA, 1986.

[53] J. W. Zindel, D. C. Van Aken, R. D. Field, P. Kurath, and H. L. Fraser. Mechanical properties of rapidly solidified Al-Fe-X and Al-Be alloys. In *Mechanical Behavior of Rapidly Solidified Materials, New York, NY, February 24–28, 1985*, pages 189–203. Metallurgical Society of AIME, Warrendale, PA, 1985.

[54] B. A. Mueller, L. E. Tanner, and J. H. Perepezko. Microstructure development in undercooled Al-Be powders. *Materials Science and Engineering A*, A150(1):123–132, February 1992.

[55] J. W. Elmer, M. J. Aziz, L. E. Tanner, P. M. Smith, and M. A. Wall. Formation of bands of ultrafine beryllium particles during rapid solidification of Al-Be alloys: Modelling and direct observations. *Acta Metallurgia et Materialia*, 42(4):1065–1080, April 1994.

[56] Loren A. Jacobson, Paul W. Stanek, W. Scott Gibbs, and Robert M. Aikin, Sr. XSR processed beryllium 28 wt% aluminum alloy. Technical report, NASP Technical Memorandum 1130, May 1991.

[57] Loren A. Jacobson. Rapidly solidified beryllium-aluminum-X alloys. Unpublished research, May 1992.

[58] Michael T. Hutchings and Aaron D. Krawitz, editors. *Measurement of Residual and Applied Stress Using Neutron Diffraction*, volume 216. Kluwer Academic Publishers, Boston, 1992.

[59] Ismail C. Noyan and Jerome B. Cohen. *Residual Stress: Measurement by Diffraction and Interpretation*. Springer-Verlag, New York, 1987.

[60] A. J. Allen, M. T. Hutchings, C. G. Windsor, and C. Andreanni. Neutron diffraction methods for the study of residual stress fields. *Advances in Physics*, 34(4):445–473, 1985.

[61] S. R. MacEwen, J. Faber, Jr., and A. P. L. Turner. The use of time-of-flight neutron diffraction to study grain interaction stresses. *Acta Metallurgia et Materialia*, 31(5):657–676, 1983.

[62] R. B. Von Dreele, J. D. Jorgensen, and C. G. Windsor. Rietveld refinement with spallation neutron powder diffraction data. *Journal of Applied Crystallography*, 15:581–589, 1982.

[63] Allen C. Larson and Robert B. Von Dreele. General structure analysis system (GSAS). Technical Report LA-UR 86-748, Los Alamos National Laboratory, 1986.

[64] M. R. Daymond, M. A. M. Bourke, R. B. Von Dreele, B. Clausen, and T. Lorentzen. Use of Rietveld refinement for elastic macrostrain determination and for evaluation of plastic strain history from diffraction spectra. *Journal of Applied Physics*, 82(4):1554–1562, August 1997.

[65] M. R. Daymond, M. A. M. Bourke, and R. B. Von Dreele. Use of Rietveld refinement to fit a hexagonal crystal structure in the presence of elastic and plastic anisotropy. *Journal of Applied Physics*, 85(2):739–747, January 1999.

[66] G. E. Bacon. *Neutron Diffraction*. Oxford University Press, third edition, 1975.

[67] Aaron D. Krawitz and Thomas M. Holden. The measurement of residual stresses using neutron diffraction. *MRS Bulletin*, 15(11):57–64, November 1990.

[68] S. Majumdar, J. P. Sing, D. Kupperman, and A. D. Krawitz. Application of neutron diffraction to measure residual strains in various engineering composite materials. *Journal of Engineering Materials and Technology*, 113(1):51–59, 1991.

[69] Aaron D. Krawitz. Neutron stress measurements in composites. In E. V. Barrera and I. Dutta, editors, *Residual Stresses in Composites: Measurement, Modeling & Effects on Thermo-Mechanical Behavior, 21–25 February 1993*, pages 161–176, Denver, Colorado, 1993. The Minerals, Metals & Materials Society, Warrendale, Pennsylvania.

[70] D. C. Dunand, D. Mari, M. A. M. Bourke, and J. A. Roberts. NiTi and NiTi-TiC composites. IV. Neutron diffraction study of twinning and shape-memory recovery. *Metallurgical Transactions A*, 27A(9):2820–2836, September 1996.

[71] Saurin Majumdar, David Kupperman, and Jitendra Singh. Determinations of residual thermal stresses in a SiC-Al_2O_3 composite using neutron diffraction. *Journal of the American Ceramic Society*, 71(10):858–863, October 1988.

[72] Saurin Majumdar and David Kupperman. Effects of temperature and whisker volume fraction on average residual strains in a SiC/Al_2O_3 composite. *Journal of the American Ceramic Society*, 72(2):312–313, February 1989.

[73] D. S. Kupperman, S. Majumdar, and J. P. Singh. Neutron diffraction NDE for advanced composites. *Journal of Engineering Materials and Technology*, 112(2):198–201, April 1990.

[74] G. L. Povirk, M. G. Stout, M. Bourke, J. A. Goldstone, A. C. Lawson, M. Lovato, S. R. MacEwen, S. R. Nutt, and A. Needleman. Mechanically induced residual stresses in Al/SiC composites. *Scripta Metallurgica et Materialia*, 25(8):1883–1888, 1991.

[75] G. L. Povirk, M. G. Stout, M. Bourke, J. A. Goldstone, A. C. Lawson, M. Lovato, S. R. MacEwen, S. R. Nutt, and A. Needleman. Thermally and mechanically induced residual strains in Al-SiC composites. *Acta Metallurgia et Materialia*, 40(9):2391–2412, September 1992.

[76] A. J. Allen, M. A. M. Bourke, S. Dawes, M. T. Hutchings, and P. J. Withers. The analysis of internal strains measured by neutron diffraction in Al/SiC metal matrix composites. *Acta Metallurgia et Materialia*, 40(9):2361–2373, 1992.

[77] M. A. M. Bourke, J. A. Goldstone, N. Shi, J. E. Allison, M. G. Stout, and A. C. Lawson. Measurement and prediction of strain in individual phases of a 2219Al/TiC/15p-T6 composite during loading. *Scripta Metallurgica et Materialia*, 29(6):771–776, September 1993.

[78] M. A. M. Bourke, J. A. Goldstone, M. G. Stout, A. C. Lawson, and J. E. Allison. Strain measurement in individual phases of an Al/TiC composite during mechanical loading. In E. V. Barrera and I. Dutta, editors, *Residual Stresses in Composites: Measurement, Modeling & Effects on Thermo-Mechanical Behavior, 21–25 February 1993*, pages 67–77, Denver, Colorado, 1993. The Minerals, Metals & Materials Society, Warrendale, Pennsylvania.

[79] N. Shi, M. A. M. Bourke, J. A. Roberts, and J. E. Allison. Phase-stress partition during uniaxial tensile loading in a TiC-particulate reinforced Al composite. *Metallurgical Transactions A*, 28:2741–2753, December 1997.

[80] J. C. Halpin and S. W. Tsai. Environmental factors in composite design. Technical Report AFML-TR-67-423, Air Force Materials Laboratory, 1967.

[81] T. W. Clyne and P. J. Withers. *An Introduction to Metal Matrix Composites*. Cambridge University Press, Cambridge, UK, 1993.

[82] H. L. Cox. The elasticity and strength of paper and other fibrous materials. *Brit. J. Appl. Phys.*, 3:72–79, 1952.

[83] T. W. Clyne. A simple development of the shear lag theory appropriate for composites with a relatively small modulus mismatch. *Materials Science and Engineering A*, A122:183–192, 1989.

[84] J. D. Eshelby. The determination of the elastic field of an ellipsoidal inclusion, and related problems. *Proc. Royal. Soc. Lond.*, A241:376–396, 1957.

[85] R. Hill. A self-consistent mechanics of composite materials. *Journal of the Mechanics and Physics of Solids*, 13:213, 1965.

[86] B. Budiansky. On the elastic moduli of some heterogeneous materials. *Journal of the Mechanics and Physics of Solids*, 13:223, 1965.

[87] A. Molinari, S. Ahzi, and R. Kouddane. On the self-consistent modeling of elastic-plastic behavior of polycrystals. *Mechanics of Materials*, 26:43–62, 1997.

[88] Z. Hashin and S. Shtrikman. A variational approach to the theory of the elastic behavior of multiphase materials. *Journal of the Mechanics and Physics of Solids*, 11:127–140, 1963.

[89] T. Christman, A. Needleman, and S. Suresh. An experimental and numerical study of deformation in metal-ceramic composites. *Acta Metallurgia et Materialia*, 37(11):3029–3050, 1989.

[90] R. Hill. *The Mathematical Theory of Plasticity*. Oxford University Press, 1950.

[91] D. C. Drucker. Engineering and continuum aspects of high-strength materials. In Victor F. Zackay, editor, *High Strength Materials*, chapter 21, pages 795–833. John Wiley & Sons, Inc., New York, 1965.

[92] D. C. Drucker. The continuum theory of plasticity on the macroscale and the microscale. *Journal of Materials*, 1(4):873–910, December 1966.

[93] T. W. Butler and D. C. Drucker. Yield strength and microstructural scale: A continuum study of pearlitic versus spheroidized steel. *Journal of Applied Mechanics*, 40:780–784, September 1973.

[94] G. Bao, J. W. Hutchinson, and R. M. McMeeking. Particle reinforcement of ductile matrices against plastic flow and creep. *Acta Metallurgia et Materialia*, 39(8):1871–1882, August 1991.

[95] T. Christman, A. Needleman, S. Nutt, and S. Suresh. On microstructural evolution and micromechanical modelling of deformation of a whisker-reinforced metal-matrix composite. *Materials Science and Engineering A*, A107:49–61, 1989.

[96] Stefan Jansson. Homogenized nonlinear constitutive properties and local stress concentrations for composites with periodic internal structure. *Int. J. Solids Structures*, 29(17):2181–2200, 1992.

[97] S. Jansson. Mechanical characterization and modeling of non-linear deformation and fracture of a fiber reinforced metal matrix composite. *Mechanics of Materials*, 12:47–62, 1991.

[98] S. Jansson and F. A. Leckie. Mechanical behavior of a continuous fiber-reinforced aluminum matrix composite subjected to transverse and thermal loading. *Journal of the Mechanics and Physics of Solids*, 40(3):593–612, April 1992.

[99] Stefan Jansson. Non-linear constitutive equations for strongly bonded fibre-reinforced metal matrix composites. *Composites*, 26:415–424, 1995.

[100] J. R. Brockenbrough, S. Suresh, and H. A. Wienecke. Deformation of metal-matrix composites with continuous fibers: Geometrical effects of fiber distribution and shape. *Acta Metallurgia et Materialia*, 39(5):735–752, 1991.

[101] David H. Carter, Andrew C. McGeorge, Loren A. Jacobson, and Paul W. Stanek. Age hardening in beryllium-aluminum-silver alloys. *Acta Materialia*, 44(11):4311–4315, 1996.

[102] L. A. Jacobson, P. W. Stanek, and J. Cotton. Microstructure and properties of rapidly solidified beryllium-aluminum alloys. Unpublished research, May 1993.

[103] David H. Carter, Paul W. Stanek, and Loren A. Jacobson. Beryllium/aluminum composites. In David Hui, editor, *Proceedings of the First International Conference on Composites Engineering, ICCE/1, 28–31 August 1994*, pages 83–84. International Community for Composites Engineering (ICCE), 1994.

[104] David H. Carter, Loren A. Jacobson, and Paul W. Stanek. Mechanical behavior of beryllium-aluminum composites. In Anoush Poursartip and Ken Street, editors, *Proceedings of the Tenth International Conference on Composite Materials, 14–18 August 1995*, volume II: Metal Matrix Composites, pages 401–408, Whistler, British Columbia, Canada, 1995. Woodhead Publishing Limited, Cambridge, England.

[105] David H. Carter and Mark A. M. Bourke. Neutron diffraction study of the co-deformation behavior of a beryllium-aluminum composite. In Murray L. Scott, editor, *Proceedings of the Eleventh International Conference on Composite Materials, Gold Coast, Queensland, Australia, 14–18 July*

1997, volume III: Metal Matrix Composites and Physical Properties, pages 736–745, Melbourne, Victoria, Australia, 1997. Australia Composite Structures Society.

[106] Erik C. M. Pennings and Wolfgang Greliner. Precise nondestructive determination of the density of porous ceramics. *Journal of the American Ceramic Society*, 72(7):1268–1270, July 1989.

[107] U. F. Kocks, C. N. Tomé, and H.-R. Wenk. *Texture and Anisotropy: Preferred Orientations in Polycrystals and their Effect on Materials Properties*. Cambridge University Press, Cambridge, UK, 1998.

[108] M. H. Poech and H. F. Fischmeister. Deformation of two-phase materials: a model based on strain compatibility. *Acta Metallurgia et Materialia*, 40(3):487–494, 1992.

[109] S. R. Gunawardena, S. Jansson, and F. A. Leckie. Modeling of anisotropic behavior of weakly bonded fiber reinforced MMC's. *Acta Metallurgia et Materialia*, 41(11):3147–3156, 1993.

Los Alamos
NATIONAL LABORATORY
Los Alamos, New Mexico 87545